The Benzodiazepine Diazepam Impairs Synaptic Plasticity via Translocator Protein (18 kDa): Implications for Alzheimer's Disease

Yuan Shi

München 2019

Dissertation
zum Erwerb des Doctor of Philosophy (Ph.D.)
an der Medizinischen Fakultät der
Ludwig-Maximilians-Universität zu München

vorgelegt von

Yuan Shi
.....

aus

Shandong, China
.....

am

13. 09. 2019
.....

Supervisor(s):	Prof. Dr. Jochen Herms
Second expert:	Prof. Dr. Armin Giese
Dean:	Prof. Dr. med. dent. Reinhard Hickel
Date of oral defense:	19. 12. 2019

I dedicate this work to my family.

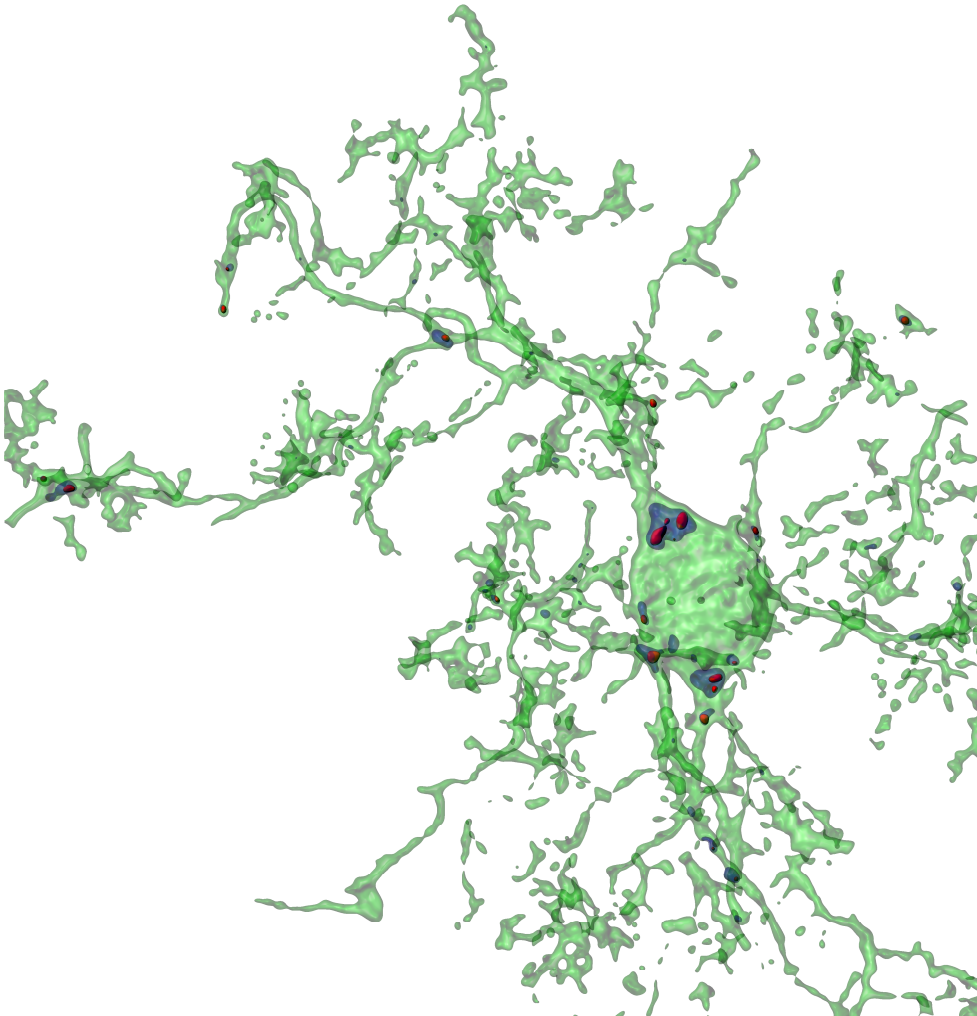

Table of Contents

Summary

Benzodiazepines are among the frequently recommended medications prominently for treating anxiety, insomnia, and epileptic seizures. In the central nervous system, benzodiazepines allosterically intensify the effect of the γ-aminobutyric acid (GABA) – one of the most important neurotransmitter mediating inhibitory effect by engaging to the benzodiazepine binding site on GABA type A receptors ($GABA_ARs$), exerting sedative, anxiolytic, anticonvulsant and other psychotropic and non-psychotropic properties. Besides, some classical benzodiazepines, most prominently amongst them diazepam, have significant additionally binding affinity for the outer mitochondrial membrane protein – 18 kDa translocator protein (TSPO), formerly named as the peripheral-type benzodiazepine receptor, which is involved in numerous functions such as steroidogenesis, mitochondrial bioenergetics, and calcium homeostasis although its ultimate function remains elusive.

Despite having been prescribed for decades, numerous studies in animals and humans have revealed that benzodiazepines can cause cognitive impairment, which limits their clinical use. Furthermore, cumulating clinical reports have suggested that chronic benzodiazepine administration may play a role in elevating the dementia risk, e.g., Alzheimer's disease (AD), which, however, is not supported unequivocally. The debate persists as long as the cellular and molecular mechanisms underlying the long-term use of benzodiazepine relevant decline of cognitive functions remain unclear.

Previously, my colleagues and I have demonstrated that alterations of dendritic spines, the highly dynamic small membranous protrusions from neuronal dendrites, functionally contribute to cognitive performance, facilitate the cognitive decline in the pathophysiology of AD, raising the intriguing hypothesis that long-term use of

benzodiazepines might affect dendritic spines and thus increase the risk of developing AD.

In this dissertation, by applying serial *in vivo* imaging longitudinally on several genetically modified mouse models, how diazepam, a most widely prescribed benzodiazepine, affects the remodelling of dendritic spines was examined, and the synaptic mechanism by which long-term diazepam use could increase the risk for the cognitive decline was proposed. To directly test the effect of diazepam on dendritic spine plasticity *in vivo*, serial imaging using two-photon microscopy was performed on GFP-M mice with the pyramidal neurons visualized in green fluorescence. Results indicate that diazepam impairs the structural plasticity of dendritic spines, leading to cognitive impairment in mice. Instead of classical $GABA_AR$s, diazepam induces such deficits via TSPO, the elevation of which was observed not only upon diazepam treatment but also in AD pathophysiology. Under both circumstances, increased TSPO drives microglia to deposit C1q, the initiating protein of the classical complement cascade and triggers excessive microglial synaptic engulfment, which can be suppressed by TSPO ablation.

Collectively, this dissertation demonstrates the disruptive role of TSPO on synaptic plasticity, provides tantalizing avenues for targeting microglial synapse loss not only for new-drug design which may avoid side effects but also for therapy and prevention for cognitive decline in AD.

1. Introduction

1.1 Benzodiazepines

Benzodiazepines are a group of psychotropic compounds with similar core chemical structure. They allosterically potentiate the inhibitory effects of GABA, exerting sedative, hypnotic, anxiolytic, anticonvulsant, and muscle-relaxant properties. In 1955, the earliest benzodiazepine drug chlordiazepoxide was formulated by Leo Sternbach and soon marketed a few years later [1]. Since then, benzodiazepines have gradually become the most widely prescribed class of drugs in clinical practice [1,2].

1.1.1 Chemistry of benzodiazepines

The fusion of a diazepine ring and a benzene nucleus composed the core chemical structure of benzodiazepines, which is bicyclic and heterocyclic [3]. In the diazepine ring, the positions 1 and 4 are usually constituted by two nitrogen atoms (Fig. 1a) [4,5].

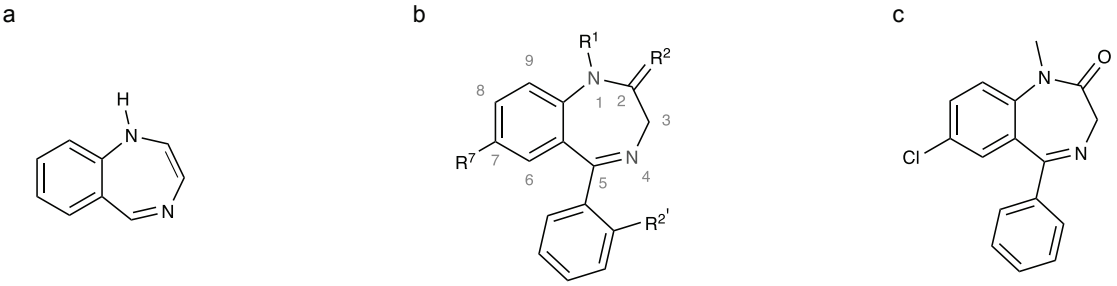

Figure 1. The core chemical structure of benzodiazepines. a, The 1,4-benzodiazepine ring. **b** & **c**, The chemical skeleton of classical benzodiazepines (**b**); the common positions of side groups are indicated by "R" labels (**b**), which regulate the unique pharmacological properties of different benzodiazepines, such as 7-chloro-1-methyl substituted diazepam (**c**).

Position 1, 2, 5, or 7 of the core structure is usually substituted by various side groups to form different benzodiazepine compounds [4,6]. The activity of benzodiazepine compounds may not maintain if position 6, 8, or 9 is substituted [6]

(Fig. 1b). The binding affinities of the benzodiazepine compounds are mainly modulated by their different substituted side groups, so do the pharmacokinetic and pharmacological properties, the effectiveness, and the biodistribution [4,6] (Fig. 1c).

1.1.2 Pharmacology of benzodiazepines

Benzodiazepines affect the central nervous system (CNS) mainly through allosterically increasing the potency of the major inhibitory neurotransmitter γ-aminobutyric acid (GABA) by binding to the benzodiazepine binding site on γ-aminobutyric acid type A receptors ($GABA_ARs$). As one of the major neurotransmitters exerting the inhibitory effect in the CNS of mammals, GABA regulates the excitability of neurons via binding to the transmembrane $GABA_ARs$ [7]. This binding modulates the gating of ion channels to allow either negatively charged chloride ions to flow into neurons or positively charged potassium ions to flow out of neurons, resulting in its hyperpolarization [7]. By elevating the difference between resting potential and threshold potential, firing would not take place.

The $GABA_A$ receptor contains a GABA-sensitive ion channel where Cl^- can go across the neuronal membrane; it also has two GABA binding sites at which GABA analogues can bind. There is a subgroup of $GABA_A$ receptor complexes with only one site to which benzodiazepines can bind [8]. Classical benzodiazepines exert their positive allosteric effect by upregulating the Cl^- conduction across the neuronal membrane, without altering the binding of GABA. Enhanced GABAergic currents thereby inhibit the excitability of neurons, so does the interneuronal communication, exerting the calming effect on many brain functions such as sedative, anxiolytic, and anticonvulsant properties [5].

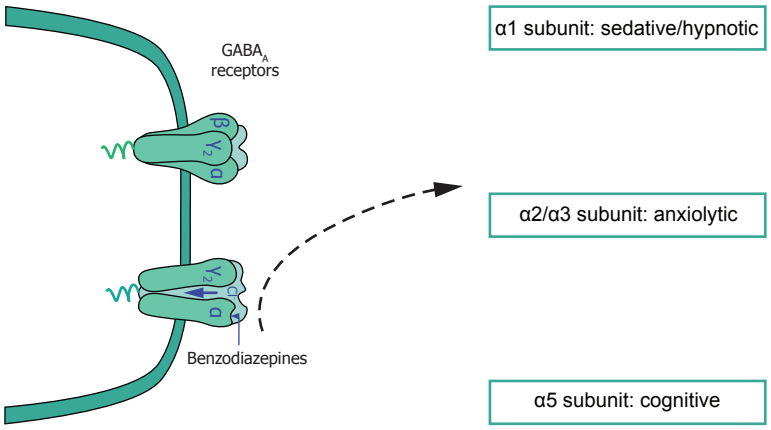

Figure 2. Schematic diagram of GABA$_A$Rs. Distinct contributions of GABA$_A$Rs subtypes towards various clinical effects.

In the CNS, classic benzodiazepines such as diazepam primarily bind to subtypes of α1-, α2-, α3-, or α5- containing GABA$_A$Rs [9]. In the past years, progress has been made concerning the neuropharmacological effects of specific GABA$_A$Rs subtypes revealed distinct contributions toward each clinical effect from each subtype (Fig. 2). More recent discoveries have unveiled the critical role of α1 subtype in sedation [10], whereas α2 subtype achieves strong antihyperalgesia than α3 or α5 subtypes [11].

1.1.3 Clinical uses of benzodiazepines

Benzodiazepines are widely prescribed in clinical practice due to their broad spectrum of pharmacological activity. According to their widely varying pharmacological and pharmacokinetic characteristics, benzodiazepines are dictated for different indications (Tab. 1).

As hypnotics, they mainly could be used to treat transient or short-term insomnia [12]. Ideally, benzodiazepines used as hypnotic drugs should have a fast onset duration and minimal side effects. However, early benzodiazepine hypnotics such as flurazepam and nitrazepam have relatively long half-lives [12], which leads to undesirable effects including sedation, and amnesia in patients. Therefore, benzodiazepines with shorter half-lives such as triazolam [13,14], loprazolam [14], and

temazepam [15] have been developed to avoid the side effects mentioned above. Diazepam is also indicated for short-term or intermittent use [16].

As anxiolytics, benzodiazepines generally are used for treating acute anxiety, episodic anxiety, and as initial treatment for agoraphobia [16]. In contrast to the treatment of sleep disorders, benzodiazepines with longer half-lives are desired to maintain a constant level of receptor occupation for anxiolysis. The benzodiazepine anxiolytics include diazepam, alprazolam, lorazepam, oxazepam, clonazepam, and chlordiazepoxide [16,17].

Benzodiazepines also have uses in epilepsy (diazepam, clonazepam, and lorazepam), alcohol withdrawal (diazepam, and clorazepate), anaesthesia (midazolam), muscle relaxant (diazepam) and occasionally in acute psychoses [16,18].

Table 1. Widely used representatives of benzodiazepines.

Pharmacokinetics	Name	Indications
Long-acting	Diazepam	Anxiety, insomnia, sedation, alcohol withdrawal, and seizure [19,20]
Long-acting	Chlordiazepoxide	Anxiety and alcohol withdrawal [20]
Long-acting	Flurazepam	Insomnia [20]
Intermediate-acting	Alprazolam	Anxiety and alcohol withdrawal [21]
Intermediate-acting	Lorazepam	Anxiety and sedation [21]
Intermediate-acting	Temazepam	Sedation, muscle spasm, and anxiety [20]
Short-acting	Midazolam	Anxiety, muscle spasm, seizure, and sedation [22]
Short-acting	Triazolam	Insomnia [20]

1.1.4 Effects of benzodiazepines on cognition

Numerous studies in human patients and animal models have revealed that benzodiazepine administration can result in mild to severe impairments in memory and cognition [23-26]. Notably, clinical evidence indicates that memory stored prior to the use of benzodiazepine is not affected [27]. In recent years, the interaction between benzodiazepine use and cognitive disorders such as dementia and AD has been broadly investigated. Clinical reports suggest that chronic administration of benzodiazepines is correlated with an elevated possibility of dementia and AD [28-30], although recently the association has been questioned [31]. Nevertheless, benzodiazepines are still suspected of contributing to cognitive decline in the elderly [32,33]. However, although benzodiazepines have been prescribed for decades, the molecular mechanisms leading to memory and cognitive impairment remains unclear.

1.2 Translocator protein (18 kDa)

As one of the two major targets of benzodiazepines, translocator protein (TSPO), an 18 kDa protein mainly expressed on the outer membrane of mitochondria [34], was formerly named as the peripheral-type benzodiazepine receptor (PBR) [35]. Based on the topological analysis, TSPO has a membrane-spanning structure carrying five α-helical structural elements with highly charged carboxyl terminus on the external cytoplasm side and amino terminus on the mitochondrial periplasm [36]. In mitochondria, TSPO participates in forming a multimeric complex composed of a 30 kDa adenine nucleotide transporter on its inner membrane and a 32 kDa voltage-dependent anion channel (VDAC) on its outer membrane [37-40].

In the CNS, microglia and astrocytes are the sources of TSPO [41,42]. Besides, some neuronal cell types such as olfactory receptor cells also express TSPO [43]. TSPO expression is relatively low in the brain during the healthy period but can be dramatically increased in the pathological brains with glial activation conditions,

including inflammation, metabolic stresses, ischemic, and neurodegenerative states [44]. TSPO is encoded by the nuclear DNA and well conserved throughout evolution. The cDNA of TSPO has been cloned from mouse, rat, cow, and human [38,45-47], which shows an 80% sequence homology [44].

1.2.1 Physiological functions of TSPO

As a major mitochondrial membrane component, TSPO has many proposed functions, including steroidogenesis, mitochondrial bioenergetics, and calcium homeostasis, although its ultimate function remains elusive. Amongst the best-defined functions of TSPO, one of them is the regulation of steroidogenesis [48]. The transportation of cholesterol between the outer and the inner membrane of mitochondria is the rate-determining step in steroid biosynthesis. Biochemical and pharmacological evidence indicated that TSPO as a key regulator of cholesterol transport [49]. However, the long posited role in steroid synthesis has been questioned due to the recent finding that TSPO knockout mice show nearly no deficits in the biosynthesis of steroid [40]. In addition to its role in steroidogenesis, recent studies show that TSPO is involved in regulating mitochondrial energy metabolism [50,51]. Overexpression of TSPO in Jurkat cells increases the ATP production in mitochondria, enhancing the cell proliferation and motility [50]. On the other hand, CRISPR/Cas9 mediated TSPO knockout in C20 human microglial cells shows a decreased mitochondrial membrane potential and an impaired respiratory function [51]. In addition, the cytosolic Ca^{2+} levels are also decreased in TSPO knockout microglial cells [51], which is consistent with a previous discovery that TSPO regulates the mitochondrial Ca^{2+} dynamics via VDAC and the cAMP-dependent protein kinase (PKA) [52]. Together, these works implicate that TSPO is a key player in mitochondrial Ca^{2+} homeostasis.

1.2.2 Pharmacology of TSPO

TSPO shows a high affinity to compounds of benzodiazepine class and isoquinoline class (Fig. 3). Benzodiazepine diazepam has a comparable affinity to both TSPO and $GABA_A$Rs, while Ro5-4864, the 4'-chloro derivative of diazepam, binds to TSPO with high affinity but only with relatively low affinity to $GABA_A$Rs. Certain benzodiazepines, such as clonazepam and alprazolam, bind only weakly to TSPO [53,54]. In addition to the benzodiazepine class, TSPO also has a high affinity for several isoquinoline carboxamide derivatives [55,56], such as PK11195 – a specific and selective high-affinity ligand. Over the past years, synthetic TSPO ligands of other classes have been developed, such as imidazopyridine alpidem (Fig. 3), phenylpurine XBD173, and benzoxazine etifoxine.

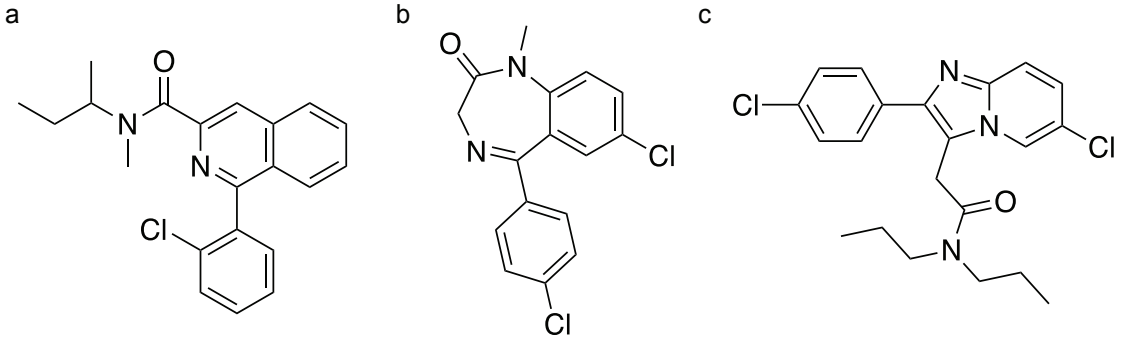

Figure 3. Chemical structures of representative TSPO ligands. a, The isoquinoline carboxamide, PK11195. **b** The benzodiazepine, Ro5-4864. **c**, The imidazopyridine acetamide, alpidem.

As a target of interest, TSPO has been vastly studied for developing drugs in the treatment of psychiatric and neurological disorders [34]. Various animal studies show the anxiolytic activity of TSPO ligands such as XBD173. XBD173 is a selective TSPO ligand with high affinity. It has fast-acting anti-panic effects and anti-anxiety effects in animal models. Moreover, the clinical trials show that XBD173 exerts rapid anxiolytic effects in human volunteers without causing sedation or withdrawal symptoms [57].

Besides the synthetic ones, TSPO is also modulated by endogenous ligands such as the diazepam binding inhibitor (DBI), a 10 kD polypeptide first isolated in 1983 from rat brain, displaces benzodiazepine diazepam from the benzodiazepine binding site [58]. Other endogenous ligands of TSPO includes the cleavage products of DBI (endozepines), protoporphyrin IX, and cholesterol [34]. However, the physiological roles of such endogenous ligands upon binding TSPO are not well defined.

Table 2. Effects of representative TSPO ligands.

TSPO Ligands	Class	Models	Effects
PK-11195	Isoquinoline carboxamide	Cultured neural cells	Outgrowth of neurites [59]
		Rodent brains	Increased neurosteroid level in brain [60]
		CNS injury models	Neuroprotection, decreased reactive microglia and astrocytes [61]
Ro5-4864	Benzodiazepine	Cultured neural cells	Outgrowth of neurites [59]
		Rodent brains	No data
		CNS injury models	Neuroprotection, decreased reactive microglia and astrocytes [62]
XBD173	Phenylpurine acetamide	Cultured neural cells	No data
		Rodent brains	Increased neurosteroid level in brain [57]
		CNS injury models	No data
Etifoxine	Benzoxazine	Cultured neural cells	Outgrowth of neurites [63]
		Rodent brains	Increased neurosteroid level in brain [64]
		CNS injury models	No data

1.2.3 TSPO and glial activation

TSPO positron emission tomography (PET) scanning is a diagnostic approach being used in clinical practice for neuroinflammation that occurs in most CNS pathological conditions. The TSPO level and binding sites for its ligands are elevated in the reactive glial cells during the pathophysiology of neuroinflammation. TSPO PET signal was first considered mainly originating from reactive microglia – the central effectors of neuroinflammation and neurodegeneration, while recent evidence also indicates a potential contribution of reactive astrocytes [65]. The TSPO-specific ligand PK11195 labelled with ^{11}C is the first TSPO PET radioligand used in clinical practice since the 1980s [66].

In 2001, the first TSPO PET brain imaging study with [^{11}C](R)-PK11195 in AD patients showed significantly TSPO binding [67]. This finding, together with other subsequent PET studies using the newer generation of TSPO radioligands (see Tab. 3) further confirmed that elevation of TSPO associated microglia activation is positively correlated with the AD pathogenesis; however the role of TSPO in the pathogenesis stays inconclusive.

Table 3. Representative radioligands of TSPO for PET imaging.

Generation	Radioligand	Class
First	[^{11}C](R)-PK11195	Isoquinoline carboxamide [68]
Second	[^{11}C]PBR28	Phenoxy acetamide [69]
	[^{18}F]PBR06	Phenoxy acetamide [70]
	[^{11}C]DAC	Aryl-oxodihydropurines [71]
	[^{18}F]DPA-714	Pyrazolopyrimidine [72]
Third	[^{11}C]ER176	Isoquinoline carboxamide [73]
	[^{18}F]GE180	Tetrahydrocarbazole [74]

Note: Due to the low signal-to-noise ratio, the application of [^{11}C](R)-PK11195 is restrained, hence the development of TSPO radioligands of the 2nd generation. However, their sensitivity to the single amino-acid substitution in the TSPO encoded by rs6971 polymorphism causes reducing of binding affinity in mutant compared to WT [75]. The advantage of the third generation of TSPO radioligands is their insensitivity to rs6971 with a high signal-to-noise ratio [74]. However, the low cerebral density of TSPO, expression by other cells, and non-specific binding of the TSPO ligands narrow the potential interest of TSPO PET.

1.3 Alzheimer's disease

Alzheimer's disease (AD) is the most frequently diagnosed neurodegenerative disease of the brain that has three major pathological hallmarks: the existence of senile amyloid plaques, consisting of the amyloid β (Aβ)-peptide that accumulates and deposits extracellularly; the formation of intraneuronal neurofibrillary tangles (NFTs) mainly made of aberrantly misfolded and hyperphosphorylated tau; and the

substantial loss of neurons [76,77]. An overwhelming majority of AD cases are sporadic- the cause of which is not a single genetic polymorphism but a combination of genetic (e.g. apolipoprotein E ε4 (APOE4) genetic variants) [78] and environmental factors (e.g. education level), while a small fraction of AD cases are characterized as familial Alzheimer's disease (FAD) – consequence of the mutant genes encoding amyloid precursor protein (APP), presenilin 1 (PSEN1), or presenilin 2 (PSEN2).

1.3.1 The discovery of the disease

The decline of the cognitive functions and ageing were connected by doctors and philosophers in ancient Greek and Rome [79]. In 1907, Alois Alzheimer, a physiatrist from Germany, noticed and firstly reported a case of a newly discovered disease [80], which was soon called after him. A woman at 51 years of age (referred to as Auguste Deter) presented a deviant clinical picture, which includes: paranoia, a rapidly worsening memory weakness, complete perplexity, intermittent delirium, and impaired memory. The static balance and motor functions were not disturbed initially but gradually compromised with a general reducing of cognitive functions while the disease was developing. Auguste Deter died after 4.5 years of illness duration. Her autopsy revealed an evenly atrophic brain without macroscopic foci, but with very particular fibrils, which can be stained by silver method of Bielschowsky. The fibrils were initially formed in “appeared” normal cells and lasted as a tangled bundle after the disintegration of the cell itself. About 1/4 – 1/3 of all neurons of the brain cortex changed in such a way [80,81]. Such changes are still observable in the brains of patients with AD today (Fig. 4).

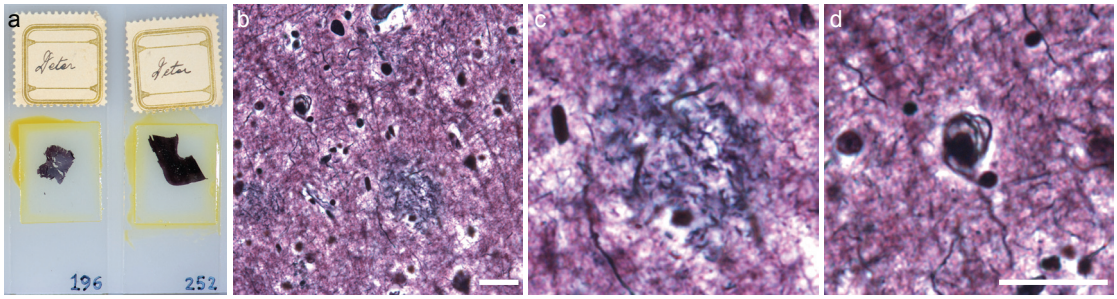

Figure 4. The neuropathological hallmarks of AD brain. a, Brain samples from Auguste Deter, which are preserved at the Center for Neuropathology and Prion Research, LMU Munich. **b**, Pathological hallmarks shown by Bielschowsky's silver staining. **c** & **d**, Enlarged images of amyloid plaques (**c**) and neurofibrillary tangles (**d**). Scale bar = 10 μm. Courtesy of Prof. Dr. h.c. Hans A. Kretzschmar.

1.3.2 Prevalence and age-based distribution

Based on cohort longitudinal studies, approximately 24.3 million dementia cases have been reported worldwide. The morbidity of dementia is around 1 case/second. The estimate of dementia patients would be twice as much within two decades; by 2040, it would be 81.1 million [82]. Similar estimates were made earlier [83]. Around 70% of them are AD patients [84], making AD the absolute majority of all dementia forms. As one of the major risk factors of AD, ageing severely influences the distribution of morbidity of AD. Statistic studies show that patients with AD are around 1.6% of the population at the age of 65–74, the number increases to 19% in the group of 75–84 years old, and in the group over 84 years old – 42% [85].

1.3.3 Symptoms, stages, and diagnosis

Traditionally, AD represents both the neuropathological criteria and clinical symptoms such as continuous cognitive and behavioural impairment (commonly at the stage of AD dementia). Benefiting from the effort by the National Institute on Aging–Alzheimer's Association workgroups and other relevant studies, a consensus was gradually formed that such processes are better to be conceptualized as a trajectory (Tab. 4).

Table 4. Staging categories for preclinical AD.

Pathology		Stage 1	Stage 2	Stage 3
Asymptomatic amyloidosis	High level of PET signal of amyloid tracer	+	+	+
	Low concentration of $A\beta_{1-42}$ in cerebrospinal fluid (CSF)	+	+	+
Neurodegeneration	Fluorodeoxyglucose positron emission tomography (FDG-PET) / functional magnetic resonance imaging (fMRI) indications of disruptions of neuronal function	-	+	+
	High concentration of tau / hyperphosphorylated tau (P-tau) in CSF	-	+	+
	Thinning of the cortex / sMRI indications of atrophy of the hippocampus	-	+	+
Subtle cognitive decline	Evidence of slight decline of cognition from the baseline	-	-	+
	Inadequate performance on more complicated cognitive test	-	-	+
	Not enough to be diagnosed as mild cognitive impairment (MCI)	-	-	+

Adapted from Reisa A. Sperling *et al*., 2011 [86].

Several preclinical stages – some asymptomatic phases with only instrumental or lab evidence of neuropathological changes have been partially consensually defined: at stage 1, high level of PET signal of amyloid tracer and low concentration of $A\beta_{1-42}$ in CSF could be demonstrated; at stage 2, amyloidosis plus observable FDG-PET / fMRI indications of disruptions of neuronal function, high concentration of tau / P-tau in CSF, and thinning of the cortex / sMRI indications of atrophy of hippocampus would be observed; at stage 3, besides all above, evidence of slight decline of cognition from the baseline and inadequate performance on more complicated cognitive test are detectable, but the criteria for MCI is not yet met [86]. In other words,

the neuropathological cascade can begin years prior to the emergence of AD clinical symptoms.

1.3.4 Pathogenesis and biomarkers

There is no consensus on the pathogenesis of AD. Though prevailing evidence shows the correlation between Aβ peptides (and their accumulation) and the pathophysiology of AD, many investigations have suggested that age-related factors such as synaptic, metabolic, neuronal, and inflammatory. may play a role in the pathogenesis of AD [87,88]. Nevertheless, alterations in APP (the encoding gene maps to chromosome 21) production or cleavage are considered as a partial cause of early-onset AD. Correspondingly, AD pathology consistently appears in patients with Down's syndrome (trisomy 21), in which exist three intact APP gene copies. For late-onset AD, APOE is regarded as the crucial genetic risk, which involves in Aβ trafficking, degradation, and plaque formation [89-91].

Table 5. Biomarkers (AT(N) criteria) used for AD diagnosis.

Group	Biomarkers
A – Aβ aggregation or pathologic state related to it	Aβ42 in CSF Ratio of Aβ42/Aβ40 PET signal of Amyloid
T – Tau aggregation (NFT) or pathologic state related to it	P-tau in CSF PET signal of tau
(N) – Neurodegeneration or neuronal injury	Anatomic MRI FDG-PET Total tau in CSF

Adapted from Clifford R. Jack Jr. *et al*., 2018 [92].

Three groups of biomarkers are recommended for AD diagnosis based on the pathophysiology of the disease (Tab. 5). Biomarkers of Aβ plaques are the high-level signal of cortical Aβ or relatively low-level Aβ42 in CSF [93]. Biomarkers of tauopathy are the high-level signal of cortical tau and high concentration of CSF P-tau [94]. Hypometabolism on FDG-PET, atrophy on MRI and high level of CSF tau are used as biomarkers for neurodegeneration and neuronal injury [95].

1.3.5 Caspase cleavage of APP

APP is an integral plasma membrane protein ubiquitously on neurons, glia, and other non-neural cells [96], and predominantly located in the synapses of neurons. Although the normal biological function is unclear, some evidence suggests that it functions as a regulator of synaptic function [97-99], neural activity and plasticity [100-102], mitochondrial function and ATP synthase activity [103,104]. In mammals, the APP family of proteins includes APP, homologous amyloid precursor-like protein 1 (APLP1), and homologous amyloid precursor-like protein 2 (APLP2) [105-107]. These proteins have a tri-domain-structure: one intracellular tail, one transmembrane domain, and one ectodomain [108,109]. Notably, the intact Aβ domain found only in APP can form Aβ oligomers and then Aβ plaques [110,111], which therefore plays a critical role in AD pathogenesis. APP is sequential proteolytically cleaved via two distinct cleavage cascades – the amyloidogenic or non-amyloidogenic cascade (Fig. 5). In the amyloidogenic cascade, the β-secretase first cleaves APP within the extracellular domain, releasing two protein products: C99 – the C-terminal fragment (CTF) and sAPPβ – the soluble ectodomain [112]. γ-secretase then cleaves the APP-CTF C99 into the neurotoxic Aβ and the APP intracellular domain (AICD) into the cytosol [113]. In the non-amyloidogenic APP cleavage cascade, α-secretase first cleaves APP within the extracellular domain into two protein products: C83 – the C-terminal membrane-spanning stub and sAPPα – soluble ectodomain [114,115]. γ-secretase then cleaves the APP-CTF C83, liberating the non-toxic peptide AICD and the p3. As γ-secretase can cleavage the APP-CTFs at various sites, AICD and Aβ peptides differ in size.

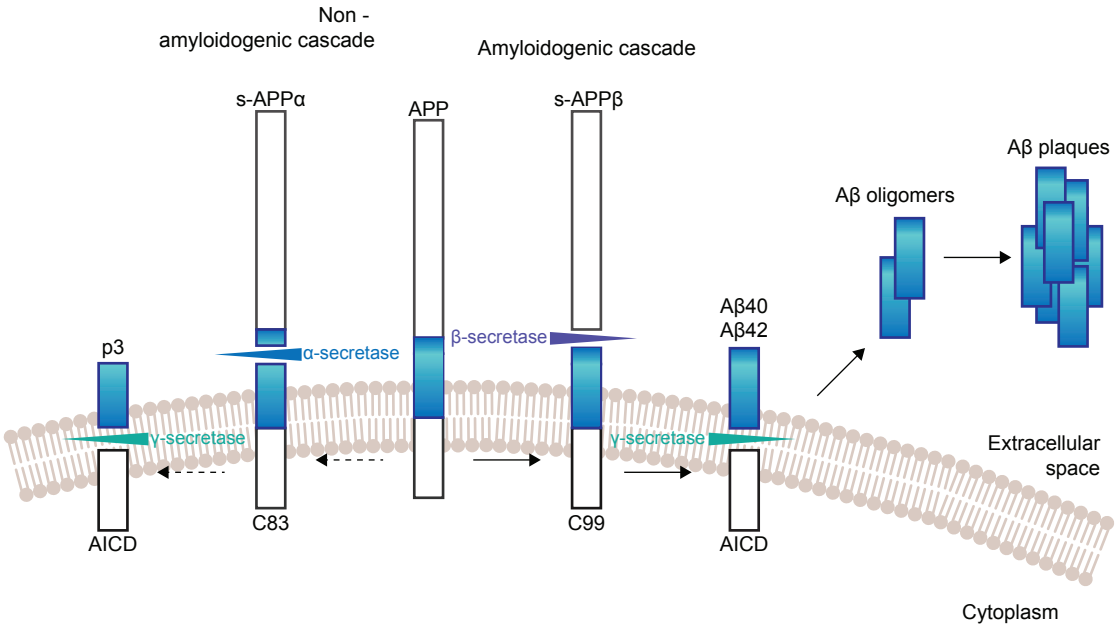

Figure 5. The cleavage cascades of APP. APP is cleaved by α-secretase (non-amyloidogenic cascade) or β-secretase (amyloidogenic cascade), respectively. Followed by γ-secretase cleavage, producing p3 or toxic Aβ accordingly.

1.3.6 The amyloid hypothesis

The amyloid hypothesis has been the leading opinion in the field of AD research for decades since its inception [116-118]. Although the hypothesis itself keeps evolving, the fundamental principle remains essentially unaltered [116,119] (Fig. 6). It posits that Aβ, derived from APP, is the initial and causative factor of AD [116,120,121]. Aβ-peptide consists of 36–43 amino acids, was first sequenced from the amyloid fibril protein from the brain vascular of patients with Down's syndrome or AD [122,123]. Aβ accumulation, causing by its elevated production or declined degradation, occurs in the brain with ageing as a consequence of genetic and environmental factors [124]. With Aβ polymerized into amyloid fibrils in the AD brain, various kinases including PKA, Ca^{2+} / calmodulin-dependent protein kinase-II (CaMKII), glycogen synthase kinase 3β (GSK-3β), and cyclin-dependent protein kinase 5 (CDK-5) are activated, causing hyperphosphorylation of a microtubule-associated binding protein-tau [125]. In axonal projections, non-pathological-form tau binds to microtubules as a stabilizer,

which facilitates the synaptic vesicle's transportation. Hyperphosphorylation of tau hinders its binding to microtubules as a stabilizer, leading to destabilization of microtubules and subsequently synaptic dysfunction [125]. Hyperphosphorylated tau shapes paired helical filaments (PHFs), which subsequently aggregate and form the NFTs [125]. As AD progresses, marked pathophysiological changes such as synaptic loss that ultimately lead to cognitive decline. Data from biochemical and genetic research of FAD strengthen this hypothesis, yet not all findings are consistent with it [116]. For instance, the toxicity of Aβ in experimental models and the mutant APP and presenilins in FAD are consistent with this view, while the healthy individuals with Aβ plaques and the repeated unsuccessful clinical trials targeting Aβ suggest there is more to it [116,124].

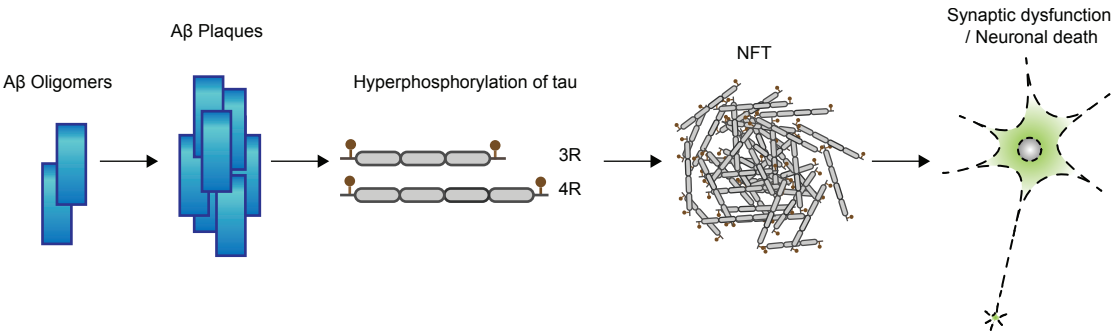

Figure 6. The amyloid cascade hypothesis.

1.3.7 Synaptic failure in Alzheimer's disease

The progressive region-specific synaptic loss that precedes neuronal dysfunction and ultimately death lays the neurobiological foundation of cognitive impairment in AD [126], compared to cerebral plaques and neurofibrillary tangles [127], yet we have only limited information about the mechanisms of synaptic vulnerability [128]. Soluble Aβ oligomers, but not the amyloid plaques, has been proved to be one of the neurotoxicity factors of synaptic and network dysfunction [129]. In multiple AD mouse models, degeneration of synapses can be observed at a rather early stage, long prior to the presence of Aβ

plaques [130,131]. Along with the progression of AD, dystrophic neurites of presynaptic origin can be observed around plaques (Fig. 7), while dendrites that are in close proximity to plaque particularly show spine loss. The degeneration of synapses subsequently causes neuronal dysfunction and death, ultimately leads to cognitive decline.

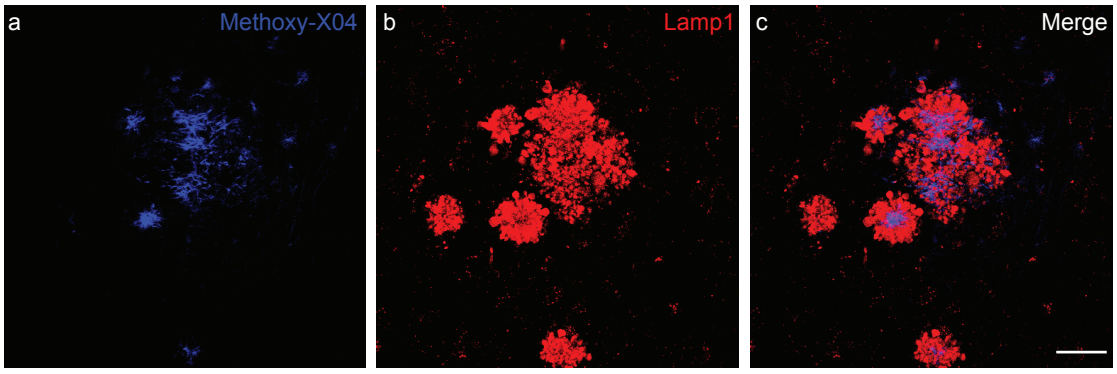

Figure 7. Representative confocal micrographs showing synaptic dystrophies in a mouse model of AD. The methoxy-X04 labelled amyloid plaques are in *blue* and Lamp1-labelled axonal dystrophies are in *red* from 5-month-old APPswe/PS1deltaE9 mice. Scale bar = 50 µm.

1.4 The dynamic synapse

1.4.1 Synapse

As mentioned above, the synapse is one of the primary targets of AD-relevant pathology. In the CNS, synapses are specialized adhesions for neuronal communication, including two types, electrical and chemical. Communication at electrical synapses occurs directly at gap junction channels via the intercellular exchange of ions, small metabolites, and second messenger molecules [132,133], whereas chemical synapses utilize neurotransmitters. Although electrical signals can be directly transmitted across gap junctions of neurons, most of the intercellular communications occur through chemical synapses [134]. A chemical synapse is an asymmetric cellular structure formed between neurons and their targets, comprising a bouton (presynaptic), a cleft, and a dendritic spine (postsynaptic) [134,135] (Fig. 8). In the

presynaptic bouton, synaptic vesicles (~50 nm diameter) containing the neurotransmitters and a few dense-core vesicles containing neuropeptides are formed [136]. Upon depolarization of the presynaptic bouton, the presynaptic voltage-gated calcium channels are opened to influx extracellular calcium, triggering the release of neurotransmitters from synaptic vesicles by exocytosis. The neurotransmitters then travel across the synaptic cleft by diffusion and interact with the postsynaptic receptors upon binding, modulating ion channels [137] and altering the electrical activity of the postsynaptic cells [134]. The altered electrical activity diminishes as the neurotransmitters dissociate from the receptors via reuptake, enzymatic degradation or diffusion. New synaptic vesicles are refilled in the presynaptic bouton by axonal transport or a local cycle of endocytosis, facilitating the new round of signal transmission [134,138].

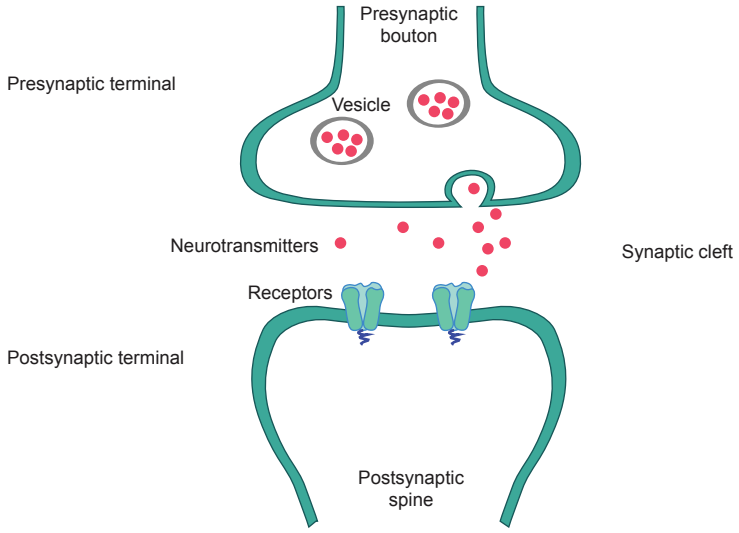

Figure 8. Schematic diagram of an asymmetric chemical synapse. The presynaptic bouton is filled with synaptic vesicles, containing neurotransmitters. Upon depolarization of the presynaptic terminal, neurotransmitters can be released into the synaptic cleft at the presynaptic active zone by exocytosis. Opposite the presynaptic plasma membrane is an electron-dense region which is called postsynaptic density [135], clustering postsynaptic receptors. The released neurotransmitters travel across the synaptic cleft by diffusion and interact with postsynaptic receptors upon binding, altering the electrical activity of the targeted cell [134].

1.4.2 Dendritic spines

In 1888, Santiago Ramón y Cajal first discovered dendritic spines using the Golgi staining [139-141]. Dendritic spines are the highly dynamic small protrusions of neuronal dendrite membrane, each of which receives informational input from presynaptic terminals [142,143]. They consist of an often rather bulbous head (~0.001–1 μm^3), being connected to the dendrite by a narrower neck which is ~0.5 μm in length and ~0.1 μm in diameter [139,144] (Fig. 9). The dendritic spine head, which is electrically and biochemically isolated from the dendrite by the neck [145-148], contains critical compartments for synaptic function and plasticity such as organelles, receptors, and signalling systems [143]. Besides, the postsynaptic membrane on the dendritic spine head also contains an electron-dense thickening known as the postsynaptic density (PSD) [149]. The PSD, which consists of various neurotransmitter receptors, ion channels, signalling complexes, and scaffolding proteins, serves as a postsynaptic structural matrix of the signal transduction machinery [150-152]. Additionally, the dendritic spine head includes smooth endoplasmic reticulum as a source and buffer of Ca^{2+} [153,154]. The smooth endoplasmic reticulum is closely coupled to multiple dendritic events such as excitability and plasticity [155,156] by modulating localized Ca^{2+} dynamics. Local alterations in the level of Ca^{2+} within dendritic spines alter the arrangement of the filamentous actin cytoskeleton, leading to actin-based dendritic spine morphology and stability changes [157,158]. Polyribosomes, which suggest local protein synthesis machinery, most commonly present in the bases of spines, but sometimes in dendritic spine heads or necks [159,160]. Emerging evidence shows that specific mRNA and protein-synthesizing machinery may occur at the dendrites and even the dendritic spines [161].

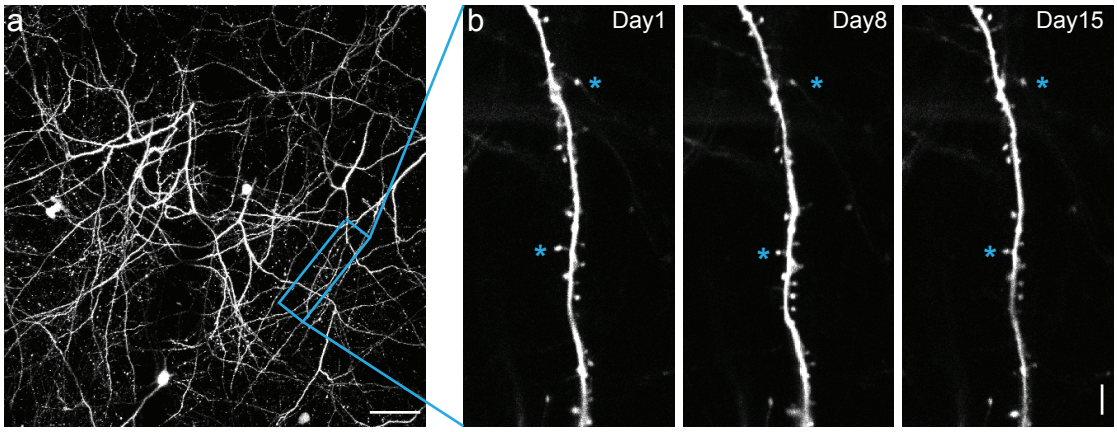

Figure 9. Representative *in vivo* two-photon micrographs showing GFP positive dendrites and spines. a, Overview of GFP-labelled dendrites in the mouse somatosensory cortex. **b**, Dendrites and its spines. Scale bars = 50 μm (overview); 5 μm (zoom in). Asterisks denote the stable spines during the consecutive imaging sessions.

1.4.3 Structural plasticity of dendritic spines

Dendritic spines, the critical structure of synapse correlates for cognitive performance, are highly dynamic [139,142]. Changes of spine density and shape have repeatedly been reported during the activity-dependent experience such as enriched environment [162,163]. Morphologically, dendritic spines are classified as three major types: mushrooms, thins, and stubbies [164,165]. Spines categorized as mushrooms have a narrow neck compare to the larger head; thins have a neck of similar size, but a smaller head; and stubbies have no obvious neck between its head and its base part. Additionally, elongated filopodia, the direct precursors to dendritic spines, can also be observed on the developing dendrites and participate in synaptogenesis actively [166]. Alterations in the morphology of dendritic spines are prominent during physiological processes such as learning [167] and pathological processes such as neurological [168] and neuropsychiatric [169] diseases, reflecting the function of synapses that supports learning and memory [144]. Besides varying in shape and size, the contents of organelles and specific molecules in dendritic spines also differ [150]. The molecular mechanisms underpinning the regulation of dendritic spine size and shape are poorly understood.

1.4.4 Dendritic spine alterations in pathological conditions

Alterations of the dendritic spine are widely observed in the pathophysiology of neurodegenerative and psychiatric disorders not only in human patients but also in the related transgenic mouse models (Fig. 10). In an AD mouse model, neuroinflammation caused by amyloid deposition impairs adaptive dendritic spine plasticity [170]. The impaired dendritic spine plasticity can also be observed in synucleinopathies like Parkinson's disease (PD) [171], which was affected by the misfolded proteins – α-synuclein. Moreover, studies on postmortem material from schizophrenic patients showed defects in the dendritic structure of pyramidal neurons, involving spine loss [172,173]. Increasing evidence suggests that several genes, which are involved in encoding C1q, triggering receptor expressed on myeloid cells 2 (TREM2), transactive response DNA-binding protein (TDP-43), and APOE4, contribute to the elimination or pruning of dendritic spines in neuropsychiatric and neurological diseases [169,174-176]. However, the ultimate mechanisms governing dynamic dendritic spine structural plasticity in the brain are still largely unknown.

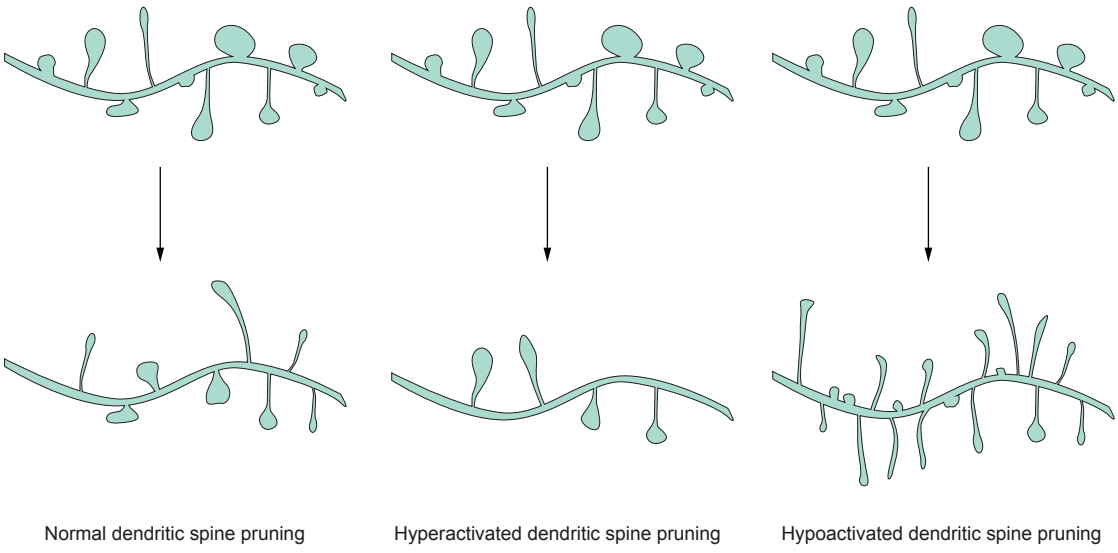

Figure 10. Structural plasticity of dendritic spines in health and disease. In the healthy state, the dynamics of the dendritic spine are in balance. In the diseased state, the pruning of the dendritic spine is either hyperactivated or hypoactivated.

1.5 Microglia in health and disease

Microglia are a type of macrophage-like neuroglia ubiquitously distributed in the CNS and constitute 10–15% of total cells in the mammalian brain. They are originally derived from myeloid precursor cells during the early stages of embryogenesis [177]. As the resident macrophage cells, they monitor the well-being of the local microenvironment and can be activated rapidly in response to pathological changes in the brain [178,179]. Activated microglia release cytokines and chemokines such as immunomodulatory and neuromodulatory messengers, which regulate the innate defence [180]. The primary aim of microglia immune reactions is CNS protection; however, the overt microglial activation could result in direct neurotoxicity, which contributes to acute and chronic neuropathologies [180].

1.5.1 Dynamic microglia–synapse interactions

Microglia are the key players in regulating neuronal and synaptic functions in the healthy brain. During development, microglia refine the neuronal circuits via synaptic pruning – a process of engulfment or elimination of synaptic elements [181]. Emerging studies implicate that microglia regulate synaptic pruning in development via potential "eat-me" pathways. For instance, C1q, C3, and several other components and receptors of the innate immune classical complement cascade, which can be rapidly involved in the recognition and elimination of the pathogens, contribute to the microglial synaptic engulfment. In the healthy postnatal brain, C1q and C3 are expressed and co-localized with the immature synapses, serving as the activity-dependent 'eat-me' signals at the synapses in less stable or less active states for removal by microglia depending on the microglia expressed CR3 [182,183]. Another immune pathway involved in microglial synaptic pruning is CX_3CL1–CX_3CR1 signalling. Although the underlying mechanism has yet to be figured out, it is

proposed that CX_3CL1 chemokine secreted by neurons regulates microglial synaptic pruning via binding to microglial CX_3CR1, namely the “find-me” pathway [184-186].

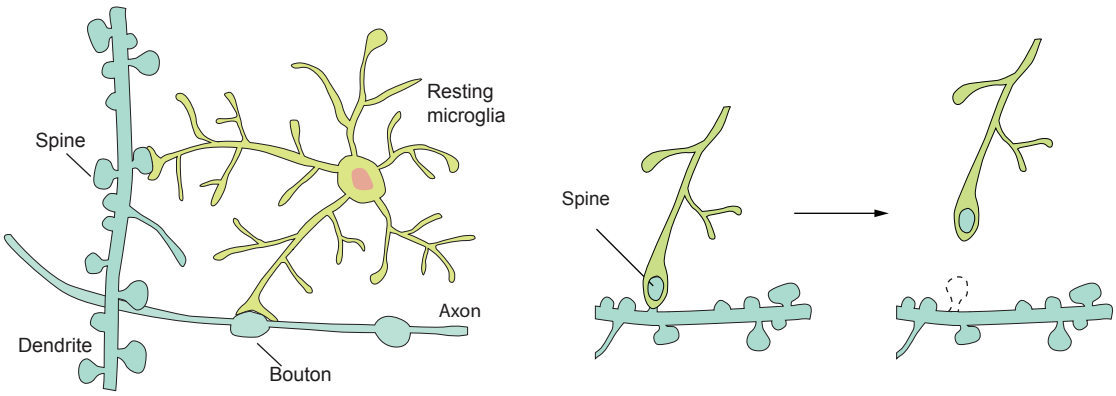

Figure 11. Microglial surveillance and monitoring. Microglia are essential in synaptic pruning: under baseline conditions, microglia constantly survey the surrounding presynaptic boutons and postsynaptic spines; altered neuronal activity triggers the changes in the surveillance by microglial processes, leading to subsequently synaptic pruning.

In the adult brain, microglia modify the activity-dependent synaptic strength remodelling that underlies learning and memory, resulting in synaptic plasticity. *In vivo* imaging has established that microglia constantly survey the surrounding synaptic elements via microglial processes [187]. Alterations in neuronal activity trigger the changes in microglia surveillance by microglial processes, resulting in the activity-dependent synaptic modulation [188,189] (Fig. 11). However, the mechanism underpinning microglia-surveillance-regulated synaptic plasticity needs to be elucidated [181].

1.5.2 Microglia in Alzheimer's disease

In AD, PD, amyotrophic lateral sclerosis (ALS), and nearly all chronic neurodegenerative diseases, activated microglia are observable (Fig. 12). Not only reacting to the pathology, microglia rather act as contributors to the pathophysiology

[190]. When being activated, microglia transfer themselves into an amoeboid morphology with shortened and extensively branched processes, the swelling of soma, and the concomitant increase of cytokines [190] (Tab. 6). For instance, activated microglia in AD show upregulated IL-1β, TGF-β, IL-6, IL-8, TNF-α, CD11c, CD14, CD36, iNOS, and MHC-II [191-194]. In addition, surface receptors such as complement receptors on the cytoplasmic membrane of microglia are also elevated when microglia being activated. The complement cascade, including classical complement proteins C1q, is involved in microglial Aβ clearance [195]. C3, the key component of the complement cascade, and its complement receptor – CR3 also participate in microglial uptake and clearance of Aβ [196]. Besides complement receptors, there are also various pattern recognition receptors expressed by microglia that are involved in recognition of Aβ peptides and modulation of microglial Aβ clearance, including scavenger receptor A, toll-like receptors, and receptor for advanced glycation end products [197-200].

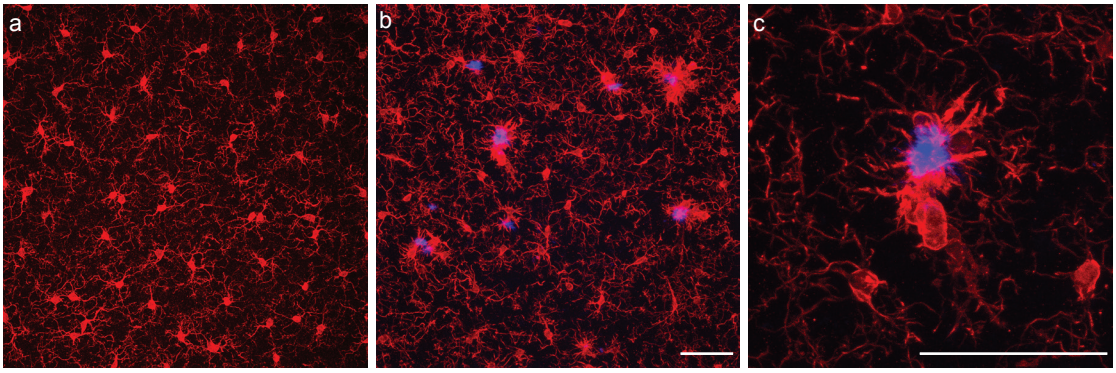

Figure 12. Activated microglia in a mouse model of AD. **a**, Resting Iba1$^+$ microglia (red) in wild-type (WT) mouse brain. **b** & **c**, Overview (**b**) and enlarged (**c**) images showing activated, Iba1$^+$ microglia (red) at an Aβ plaque site (blue) in APPswe/PS1deltaE9 transgenic mouse brain. Scale bar = 50 μm.

Table 6. Microglial pro-inflammatory cytokines.

Cytokine	Full name	Family
IL-1α and IL-1β	Interleukin-1α and interleukin-1β	Interleukin-1 [201,202]
IL-6	Interleukin-6	Interleukin-6 [203]
CXCL8 / IL-8	C-X-C motif chemokine ligand 8 / Interleukin-8	CXC [204]
IL-12	Interleukin-12	Interleukin-12 [205]
IL-15	Interleukin-15	γ-Chain [206]
IL-18 / IGIF	Interleukin-18/interferon-γ inducing factor	Interleukin-18 [207]
CXCL10 / IP-10 / SCYB10	C-X-C motif chemokine ligand 10 / interferon-γ induced protein-10 / small-inducible cytokine B10	CXC [208]
CCL2 / MCP-1	C-C motif chemokine ligand 2 / monocyte chemoattractant protein-1	CC [209]
CSF1 / M-CSF	Colony stimulating factor 1 / macrophage colony-stimulating factor	CSF [210]
CCL22 / MDC	C-C motif chemokine ligand 22 / macrophage-derived chemokine	CC [211]
CCL3 / MIP-1α and CCL4 / MIP-1β	C-C motif chemokine ligand 3 / macrophage inflammatory proteins-1α and C-C motif chemokine ligand 4/macrophage inflammatory proteins-1β	CC [212]
CXCL2 / MIP-2	C-X-C motif chemokine ligand 2 / macrophage inflammatory protein-2	CXC [213]
CCL19 / MIP-3β	C-C motif chemokine ligand 19 / macrophage inflammatory proteins-3β	CC [214]
TNF-α and TNF-β	Tumor necrosis factor-α and tumor necrosis factor-β	TNF [215]
CCL5 / RANTES	C-C motif chemokine ligand 5/regulated upon activation, normal T cell expressed and secreted	CC [216]
CD11c / ITGAX	Cluster of differentiation 11c / integrin subunit α X	Integrin α chain [217]
CD14	Cluster of differentiation 14	LRR [218]
CD36	Cluster of differentiation 36	SR-B [193]
iNOS	Inducible nitric oxide synthase	NOS [219]
MHC II	Major histocompatibility complex class II	MHC [220,221]

In AD, activated microglia function amphibiously. On the one hand, activated microglia clear Aβ deposits from the CNS by microglial phagocytosis [222,223], preventing amyloid fibrils from extending by tightly wrapping around amyloid plaques [224] at the early stages of AD, although recently reported results from intravital experiments indicate that microglia have little effectiveness in clearing fibrillary Aβ [225,226]. On the other hand, microglia of long-term activated state trigger multiple proinflammatory cascades via synthesizing and secreting cytokines, chemokines, and reactive oxygen species, contributing to neurotoxicity and synaptic loss [227]. Understanding the impact of microglial activation at different disease stages will provide the opportunity to monitor and lessen the destructive and maximize the beneficial effects in the treatment of AD [197].

1.5.3 Microglia–synapse dysfunction in Alzheimer's disease

Besides the critical role in refining the developing neuronal circuits and regulating the synaptic plasticity in learning and memory, emerging evidence implicates that microglia are also involved in synaptic dysfunction in many neurodegenerative diseases. One of the potential pathways involved in regulating synaptic plasticity in AD is the complement cascade. For instance, C1q is profoundly upregulated both in patients with AD and transgenic mouse models [228-230], which initiates the subsequent classical complement pathway, leading to excessive microglial synaptic engulfment. Another pathway involved in regulating synaptic plasticity is associated with TREM2, variants of which are well known to increase the risk of late-onset AD. It has recently been proved to be essential for microglial synaptic elimination in neurodevelopmental diseases [169]. In addition, a mouse model of AD lacking microglial TDP-43, a DNA/RNA binding protein regulating microglial phagocytosis, also shows significant synapse loss [174].

1.6 Intravital microscopy

Intravital microscopy represents a group of various optical microscopes, aiming at observing biological processes in live animals (*in vivo*). One of the most widely known applications of *in vivo* imaging is on the green fluorescent protein (GFP)-transgenic animals. The GFP transgenic animals constantly produce green fluorescent protein and light up certain parts of them, like specific brain cell circuits. Hereditability is one of the biggest advantages of GFP application. Animal expressing the GFP gene can pass this property to their descendants, making the longitudinal study of certain cells and tissues with GFP expressing in it possible. Besides, not only observation of GFP is noninvasive, but also GFP itself does not hinder biological processes, making GFP one of the best markers for *in vivo* imaging [231,232].

1.6.1 Fluorescence microscopy

Fluorescence microscopy, as an essential imaging tool, is vastly used for studying various properties of organic or inorganic substances. Differs from conventional microscopy, fluorescence microscopy uses fluorescence and phosphorescence, in place of, or together with scattering, reflection, and attenuation, to generate images. There are various types of fluorescence microscopies, from simple epifluorescence microscope to complex confocal and two-photon microscopes. The primary function of laser scanning confocal microscopy (LSCM), is to increase the contrast and optical resolution of conventional fluorescence microscopy. Fluorescence signals are acquired point by point, using laser beams, instead of the mercury lamp, led by scanner mirrors. Out-of-focus light is blocked by a spatial pinhole from entering the detector, producing clear optical sections. Consecutively acquired optical sections at different levels perpendicular to the optical axis within a specimen are called “z-stack”. Based on a series of z-stack sections, a 3D reconstruction of the scanned area can be created.

1.6.2 In vivo two-photon microscopy

Two-photon excitation microscopy is a fluorescence imaging approach that can image living tissue to a depth of approximately 1 mm, which is 2–3 times more compared to confocal microscopy. Unlike confocal microscopy, which generates single excitation light at a wavelength shorter than the emission wavelength, two-photon microscopy generates two exciting photons within 1 femtosecond, whose wavelengths are longer than the wavelength of the emitted light. Due to the multiphoton excitation, the background signal can be decidedly suppressed (Fig. 13). On top of that, instead of UV light used by confocal microscopy, two-photon microscopy uses near-infrared excitation light, minimizing scattering in the tissue.

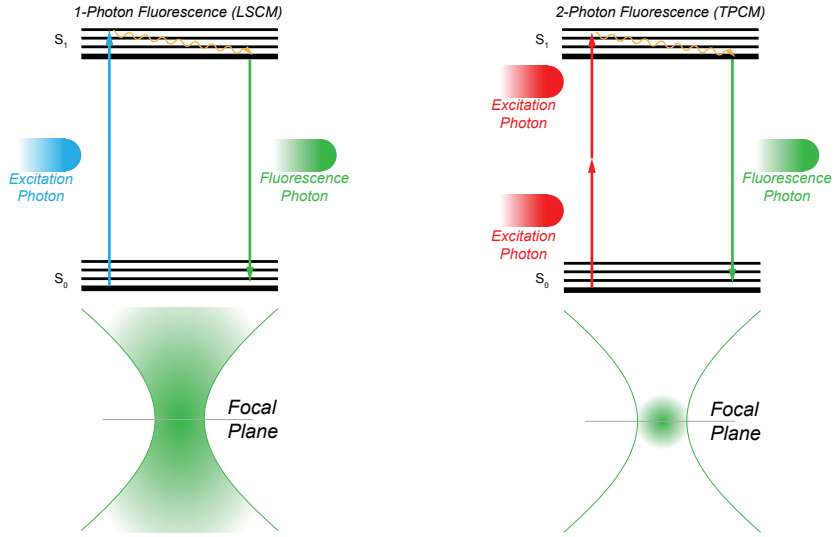

Figure 13. Schematic diagram of one- and two-photon excitation. In one-photon excitation, a single photon with sufficient energy is absorbed to excite the fluorophore from the ground state (S_0) to the excited higher-energy state (S_1) and emits a photon with slightly lower energy when transiting back to the initial ground state S_0. In two-photon excitation, two lower-energy photons are simultaneously absorbed to the fluorophore, emitting a photon in the visible wavelength.

2. Methods

2.1 Animals

GFP-M (Thy1-eGFP) transgenic mice [232], PV-Cre mice, and APPswe/PS1deltaE9 mice were obtained from the Jackson Laboratory. Homozygous mice with quadruple (H-R) point mutation of $GABA_AR$ (*Gabra RRRR* mice) were generated from single point-mutated mice [11]. TSPO knockout (C57BL/6-Tspo$^{tm1GuMu(GuwiyangWurra)}$) (*Tspo* $^{-/-}$) mice were generated and validated as described previously [233]. In this study, PV-Cre, *Tspo* $^{-/-}$, and APPswe/PS1deltaE9$^{+/-}$ × *Tspo* $^{-/-}$ mice were interbred with GFP-M mice to generate heterozygous GFP reporter lines, respectively. All the transgenic mice were C57BL/6 genetic background except for the *Gabra RRRR* mice, which were maintained on the 129X1/SvJ genetic background (Tab. 7). Gender-mixed mice were included in the studies, and age-matched WT littermates served as controls. For the behavioural experiments, mice were assigned to the experimental groups with uniformly distributed sexes and ages. All the behavioural analyses were performed during the 0700–1900 light cycle. Mice were kept under pathogen-free conditions (21 ±1 °C, at a cycle of 12-h light / 12-h dark) with *ad libitum* access to food and water in the animal facility at the Centre for Neuropathology, Ludwig Maximilian University of Munich. All mice were kept individually in standard cages after surgery. All animal experimental protocols were in compliance with the regulations of the Ludwig Maximilian University of Munich and approved by the Government of Upper Bavaria.

Table 7. Experimental models.

Experimental models	Source	Identifier
Mouse: B6.129P2-*Pvalb*$^{tm(cre)Arbr}$/J	The Jackson Laboratory	JAX: 017320
Mouse: B6.129P2-*Pvalb*$^{tm(cre)Arbr}$/J x Tg(Thy1-EGFP)MJrs/J	This paper	N/A
Mouse: B6.Cg-Tspo$^{tm1.1Guwu}$	Banati et al., 2014	RRID: MGI: 5603428
Mouse: B6.Cg-Tspo$^{tm1.1Guwu}$ x Tg(Thy1-EGFP)MJrs/J	This paper	N/A
Mouse: B6.Cg-Tg(APPswe, PSEN1dE9)85Dbo/Mmjax	The Jackson Laboratory	JAX: 34832-JAX
Mouse: B6.Cg-Tg(APPswe, PSEN1dE9)85Dbo/Mmjax x Tg(Thy1-EGFP)MJrs/J	This paper	N/A
Mouse: B6.Cg-Tg(APPswe, PSEN1dE9)85Dbo/Mmjax x B6.Cg-Tspo$^{tm1.1Guwu}$ x Tg(Thy1-EGFP)MJrs/J	This paper	N/A
Mouse: *Gabra RRRR*	Ralvenius et al., 2015	N/A
Mouse: Tg(Thy1-EGFP)MJrs/J	The Jackson Laboratory	JAX: 007788

2.2 Genotyping

Animals were genotyped following the standard protocols. In brief, the tail tip (approximately 3 mm in length) or ear punch (approximately 2-mm-diameter diste) tissues were collected when mice were at one month of age. All samples were kept at -20 °C until analysis. Invisorb DNA Tissue HTS 96 Kit (Invitek Molecular, Germany) and peqGOLD Tissue DNA Mini Kit (VWR, USA) were used to isolate genomic DNA. Subsequent polymerase chain reaction (PCR) was performed to amplify the respective transgenic construct using OneTaq Hot Start Quick-Load (NEB, USA) and specific forward and reverse primers (Tab. 8) on a Mastercycler (Eppendorf, Germany). The amplification products were analyzed on 1.5–2% agarose gel with electrophoresis and ethidium bromide staining.

Table 8. Primers for genotyping.

Strain	Primer	Sequence (5'-3')	Length (bp)
APPswe/PS1deltaE9	IMR 42	CTA GGC CAC AGA ATT GAA AGA TCT	24
	IMR 43	GTA GGT GGA AAT TCT AGC ATC ATC C	25
	IMR 1644	AAT AGA GAA CGG CAG GA	17
	IMR 1645	GCC ATG AGG GCA CTA AT	17
GFP-M	IMR 0872	AAG TTC ATC TGC ACC ACC G	19
	IMR 1416	TCC TTG AAG AAG ATG GTG CG	20
Pvalb	oIMR 1084	GCG GTC TGG CAG TAA AAA CTA TC	23
	oIMR 1085	GTG AAA CAG CAT TGC TGT CAC TT	23
	oIMR 8290	CAG AGC AGG CAT GGT CAC TA	20
	oIMR 8291	AGT ACC AAG CAG GCA GGA GA	20
Tspo $^{-/-}$	P1	GGT AGA CTA GTG TGG GAA GAT TTG A	25
	P2	ATG GTG ATT GCA ACT GAT GTT C	22
	P3	TAG ATA CTG ACC CTA TCT GGG ATG T	25
Gabra-RRRR (Gabra1 H101R)	UR 12	CAA TGG TAG GCT CAC TCT GGG AGA TGA TA	29
	UR 70	AAC ACA CAC TGG CAG GAC TGG CTA GG	26
Gabra-RRRR (Gabra2 H101R)	KL 25	GCA TGC ACC ACC CAG GAA GCG ATT	24
	KL 5	TCC ATC ATC CTG GAT TCG AAG CAG C	25
Gabra-RRRR (Gabra3 H126R)	UR 75	GAC AGA CAT GGC ATG ATG AAA GAC TGA AAT	30
	UR 106	ACA AAA TGT AAG AAC AAG AAC CAA GAA AAT	30
Gabra-RRRR (Gabra5 H105R)	RK 4	TTA AAC CGC AGC CTT TCA TCT TTC	24
	RK 5	GAG GCC ACC TAA TGC TTC CAG CTT	24

2.3 Postmortem human brain tissue

Brain samples from patients with AD or noncognitively impaired individuals were obtained from the Neurobiobank Munich, Ludwig Maximilian University of Munich. All studies involving human samples were in accordance with the Ludwig Maximilian University of Munich Ethics Board. Whole hemispheres were formalin-fixed at autopsy and samples from cortices obtained after two weeks fixation when

hemispheres had been cut into 1 cm thick slices. AD tissues were from patients with neuropathological features (Tab. 9). To assure blinded handling with personal data, brain bank pseudonyms of AD and non-AD cases were randomly assigned to new numerical pseudonyms.

Table 9. Clinical characterization of AD cases.

Pseudonym	Age at death	Gender	p.m. interval (h)	Neuropathological diagnosis	Thal stage	Braak stage
#01	87	female	37	AD 6 Aβ 5 CAA 2 (discrete amyloid pathology) CERAD C LBD 6	5	negative
#03	73	female	17	AD 2 Aβ 5 CAA 0 CERAD 0* (AT8 not evaluated) AGD 2	5	2
#08	76	male	13 till 36	AD 3 Aβ >=3 (midbrain and cerebellum not evaluated) CAA 0 CERAD B AGD 1 (low)	>3	3
#10	85	male	69	AD 1 Aβ 5 CAA >=1 CERAD 0*	5	negative

2.4 Drug administration

The key chemicals involved in the study are catalogued as in Tab. 10. Diazepam and zolpidem were purchased from Ratiopharm (Ulm, Germany) and STADApharm (Bad Vilbel, Germany), respectively. XBD173 and allopregnanolone were obtained from Sigma-Aldrich (St. Louis, MO, USA). Flumazenil and clozapine *N*-oxide (CNO) were acquired from Abcam (Cambridge, UK). PLX5622 was provided by Plexxikon (Berkeley, CA, USA) and formulated in AIN-76A standard chow by Research Diets (New Brunswick, NJ, USA) at 1200 mg/kg. Diazepam, zolpidem, and XBD173 were suspended in 0.5% sodium carboxymethyl cellulose aqueous solution and administrated intragastrically (i.g.). Flumazenil and CNO were suspended in saline containing 0.5% Tween 80 for intraperitoneal (i.p.) injection. Allopregnanolone was suspended in saline containing 0.5% Tween 80 for subcutaneous (s.c.) injection. All suspensions of drugs were administered between 0800 and 0900 a.m. at a volume of 10 mL/kg body weight, once daily for seven or twenty-eight consecutive days, unless otherwise specified. The drug doses used were: diazepam (5 mg/kg), zolpidem (2.5 mg/kg), XBD173 (5 mg/kg), allopregnanolone (10 mg/kg), flumazenil (15 mg/kg), and CNO (1 mg/kg). Flumazenil was injected at the dose of 15 mg/kg 15 min before diazepam, considering the duration of action of flumazenil is short compared to diazepam, supplemental flumazenil was provided to mice via drinking water at the dose of 10 mg/kg per day to maintain the desired antagonism effects. In this case, flumazenil was dissolved in drinking water containing 0.5% ethylene glycol. To pharmacologically ablate microglia, mice were fed with PLX5622 chow *ad libitum* for 6 weeks before the one-week diazepam treatment and continued along the whole imaging process.

Table 10. Key chemicals.

Chemicals	Source	Identifier
5α-Pregnan-3α-ol-20-one	Sigma-Aldrich	CAS: 516-54-1
Clozapine *N*-oxide	Abcam	CAS: 34233-69-7
Diazepam	Ratiopharm	CAS: 439-14-5
Flumazenil	Abcam	CAS: 78755-81-4
PLX5622	Plexxikon	https://www.plexxikon.com/
XBD173	Sigma-Aldrich	CAS: 226954-04-7
Zolpidem	STADApharm	CAS: 82626-48-0

2.5 Cranial window implantation

The surgical procedure of cranial window implantation was performed as previously described [234] with modifications. Briefly, mice were anaesthetized by intraperitoneal injection with a mixture of 5.0 mg/kg midazolam, 0.05 mg/kg fentanyl, and 0.5 mg/kg medetomidine [235] and mounted onto a stereotaxic frame. The surface of the somatosensory cortex was exposed by removing a 4 mm-diameter circular piece of the skull with a dental drill, and the craniotomy was closed immediately by covering a 4 mm-diameter circular coverslip. Dental acrylic was then used to seal the margin between the circular coverslip and the skull. A z-shaped holder was cemented on the mouse skull for fixing the mouse on the framework attached to the microscope stage during imaging. After surgical implantation, mice were single-housed and allowed to recover for 4 weeks before being included in subsequent *in vivo* two-photon imaging.

2.6 AAV vector construction

The pAAV-hSyn-DIO-mCherry and pAAV-hSyn-DIO-hM3D(Gq)-mCherry plasmids [236] were obtained from Dr. Bryan Roth at the University of North Carolina at Chapel Hill and packaged in serotype 2 by Addgene (# 50459-AAV2, # 44361-AAV2; Cambridge, MA, USA) at titer ≥ 4 × 10^{12} vg/mL (Tab. 11). The Cre-dependent adeno-associated virus (AAV) expresses designer receptors exclusively activated by designer drugs (DREADDs) under human synapsin 1 promoter with mCherry reporter and confer activation by CNO.

Table 11. Adeno-associated virus strains.

Virus strains	Source	Identifier
pAAV-hSyn-DIO-hM3D(Gq)-mCherry	Krashes *et al.*, 2011 [236]	Addgene AAV2; 44361-AAV2
pAAV-hSyn-DIO-mCherry	A gift from Bryan Roth	Addgene AAV2; 50459-AAV2

2.7 Stereotactic injection

Mice were anaesthetized by intraperitoneal injection with a mixture of 0.05 mg/kg fentanyl, 5.0 mg/kg midazolam, and 0.5 mg/kg medetomidine [235] and fixed on a stereotaxic injection setup. The AAV vector containing doubly floxed hM3D(Gq)-mCherry (pAAV-hSyn-DIO-hM3D(Gq)-mCherry) was stereotactically infused into the bilateral somatosensory cortex. A volume of 150-300 nL AAV vector was inoculated into each site at a titer of 10^{12} vg/mL. The inoculation was performed at 5 different sites at the depth of 700–800 μm, followed by cranial window implantation as mentioned above for the subsequent *in vivo* two-photon imaging. The pAAV-hSyn-DIO-mCherry vector containing doubly floxed mCherry was used as a control. After surgical injection, animals were single-housed and allowed to recover for 4 weeks before being included in subsequent experiments.

2.8 Longitudinal *in vivo* imaging using two-photon microscopy

All mice were anaesthetized under isoflurane during imaging. The consecutive *in vivo* two-photon micrographs of eGFP-labelled layer-V-pyramidal-neurons-origin apical dendritic tufts in the somatosensory cortex were consecutively imaged once per week through a 20× water-immersion objective on a Zeiss LSM 7 MP microscope (Zeiss, Germany). For imaging sessions, the wavelength was set to 880 nm to excite eGFP. For z-stack images acquisition, the ZEN software (Zeiss, Germany) for Zeiss LSM 7 MP microscope was used. Overview image stacks were taken as 424 × 424 × 350 μm^3, with a 0.83 μm/pixel xy-resolution and 1 μm/pixel z-resolution. In subsequent imaging sessions, the same imaging field was repositioned by orienting at the unique pattern of blood vessels. Individual dendrites were aligned to the same position according to the acquired images from the first imaging session. The period of each imaging session is no more than 60 min. Two to three positions per mouse, containing 10–15 dendrites were imaged. The data were acquired in a consistent manner throughout the experiments.

2.9 *In vivo* two-photon images processing and analysis of dendritic spines

Due to the restrained resolution in z-dimension, for further analysis, only spines which sprout laterally from the dendrites in the acquired images with sufficient signal-to-noise ratio were included. Dendritic spines along the dendrite were manually identified and tagged as newly gained, lost or stable based on the following criteria: during the consecutive imaging sessions, dendritic spines which emerged or disappeared were tagged as gained or lost, respectively; dendritic spines which remained unaltered locations along the dendrite for at least two consecutive imaging sessions were classified as stable (acceptable range <0.5 μm). The fraction of gained, lost, or stable dendritic spines was calculated by normalizing the number of gained, lost, or stable dendritic spines to the enumerated total dendritic spine

numbers. The dendritic spine density was calculated and normalized to the length (1 μm) of the dendrite for each imaging time point. The spine density in the first imaging time point was used as a baseline to determine the changes of spine density at the following different time points. For illustration purposes, maximum intensity projections of the three-dimensional (3D) images in the z-dimension were processed using LSM Image examiner (Zeiss, Germany) with distracting neighbouring dendritic elements removed. The maximum-intensity-projection images were then deconvolved using AutoQuant X3 (Media Cybernetics, USA), followed by the contrast and brightness adjustment.

2.10 Immunohistochemistry

Deep sedation anaesthesia was conducted on mice, followed by transcardially perfused using 4 °C phosphate-buffered saline (PBS) and 4% paraformaldehyde. The cerebral hemispheres selected for immunohistochemistry were sectioned into 50 μm thick after being immersed in 4% paraformaldehyde for 24 h for the post-fix. Permeabilization of free-floating sections was performed with 2% Triton X-100 overnight. Sections were then blocked at room temperature with blocking buffer (10% normal goat serum (NGS) with 2% bovine serum albumin (BSA) and 0.3% Triton X-100 in PBS (PBTx)) for 2–4 h. Sections were then incubated with primary antibodies (Tab. 12) for 24–48 h at 4 °C, respectively. After being washed for 3 × 10 min in PBS, sections were then processed with secondary antibodies for 4 h at room temperature, respectively. To visualize the Aβ plaques, sections were stained with methoxy-X04 (10 μg/mL in 50% ethanol; Tocris Bioscience, UK) for 30 min and were washed for 3 × 10 min with 50% ethanol at room temperature. Sections were then set on the microscope slides and mounted using a fluorescence mounting medium (Dako, Germany). Images were obtained through a 40×/1.4 oil objective on a Zeiss LSM780 confocal microscope (Zeiss, Germany).

Table 12. Primary antibodies used in this study.

Antibodies	Source	Identifier
Rabbit monoclonal anti-C1q antibody	Abcam	Cat# ab182451; RRID: AB_2732849
Rat monoclonal anti-CD68	Bio-Rad	Cat# MCA1957; RRID: AB_322219
Guinea pig polyclonal anti-c-Fos	Synaptic Systems	Cat# 226 004; RRID: AB_2619946
Rabbit polyclonal anti-$GABA_A$ receptor alpha 1	Abcam	Cat# ab33299; RRID: AB_732498
Rabbit monoclonal anti-GAPDH	Cell Signaling Technology	Cat# 5174S; RRID: AB_10622025
Mouse monoclonal anti-GFAP (Cy3)	Abcam	Cat# ab49874; RRID: AB_880203
Rabbit polyclonal anti-GFP (Alexa Fluor 488)	Thermo Fisher Scientific	Cat# A-21311; RRID: AB_221477
Goat polyclonal anti-GFP (FITC)	Abcam	Cat# ab6662; RRID: AB_305635
Guinea pig polyclonal anti-Homer1	Synaptic Systems	Cat# 160 004; RRID: AB_10549720
Guinea pig polyclonal anti-Iba1	Synaptic Systems	Cat# 234 004; RRID: AB_2493179
Rabbit polyclonal anti-Iba1	Wako	Cat# 019-19741; RRID: AB_839504
Mouse monoclonal anti-NeuN	Millipore	Cat# MAB377; RRID: AB_2298772
Goat polyclonal anti-Parvalbumin	Abcam	Cat# ab32895; RRID: AB_777105
Rabbit monoclonal anti-PBR	Abcam	Cat# ab109497; RRID: AB_10862345
Mouse monoclonal anti-PSD-95	Synaptic Systems	Cat# 124 011; RRID: AB_10804286
Guinea pig polyclonal anti-S100B	Synaptic Systems	Cat# 287 004; RRID: AB_2620025
Rabbit polyclonal anti-TSPO	Millipore	Cat# ABC139; RRID: AB_2801545

2.11 Golgi–Cox staining

The FD Rapid GolgiStain™ Kit (FD NeuroTechnologies, Inc., USA) was used for the Golgi–Cox staining. Briefly, mice were induced into deep anaesthesia using a mixture of ketamine and xylazine at the concentration of 200 mg/kg and 14 mg/kg, respectively, and transcardially perfused with 4 °C PBS. Brains were harvested and immersed immediately in a solution containing potassium dichromate, potassium chromate and mercuric chloride at room temperature for 14 days. The brains were then processed using a vibratome (VT1000S, Leica, Germany) into 200 μm thick sections, transferred and set on gelatin-coated microscope slides. The sections were dried at room temperature in the dark for 48 hours and then stained using a mixture of solutions according to the manufacturer's protocols. The sections were then dehydrated using 50%, 75%, 95%, and absolute ethanol consecutively, then cleared in xylene, mounted with Permount mounting medium (Fisher Chemical, USA) and preserved at room temperature in the dark for further analysis. Images of apical dendrites originating from Golgi–Cox-stained cortical layer V pyramidal neurons were obtained through a 63×/1.4 oil immersion objective on a Zeiss Axio Imager M2 microscope (Zeiss, Germany).

2.12 3D morphometric analysis of dendritic spines

Dendritic spine morphology was semi-automatically reconstructed and analyzed using FilamentTracer module in Imaris 9.3.1 (Bitplane, Switzerland) and automated categorized using Matlab (MathWorks, USA) according to the morphological criteria: stubby spine: length(spine) / mean_width(neck) < 3 and max_width(head) / min_width(neck) < 1.1; mushroom spine: max_width(head) / min_width(neck) >= 1.1 and max_width(head) > 0.2 μm and min_width(neck) > 0 μm; thin spine: max_width(head) / min_width(neck) >= 1.1 and max_width(head) <= 0.2 μm or

length(spine) / mean_width(neck) >= 3. Spine density refers to the number of spines per dendritic length. Spine head volumes were assessed automatically by Imaris.

2.13 Morphological analysis of microglia

The acquisition of 30 µm z-stack confocal images of 2048 x 2048 x 30 pixels was carried out through a 40×/1.4 oil objective using a Zeiss LSM780 confocal microscope (Zeiss, Germany) at 1 µm intervals. Deconvolution in AutoQuantX3 (Media Cybernetics, USA) was performed on all the confocal stacks which were included in the subsequently 3D analysis. FilamentTracer module in Imaris 9.3.1 (Bitplane, Switzerland) was used to trace and analyze the morphology of microglia from the somatosensory cortex. The total process length, total process volume, numbers of segments, terminal points, and branch points were measured. Three cortical microglia per animal from 3–5 animals per group were analyzed.

2.14 Quantification of microglia–spine interactions

Coronal free-floating sections obtained from GFP-M mice were co-stained with anti-Iba1 (1:500, Wako) and anti-GFP (FITC) (1:200, Abcam) primary antibodies followed by the anti-rabbit Alexa 594 secondary antibody (1:500, Life technologies) to visualize microglia and dendrites. Confocal stacks were obtained through a 40×/1.4 oil objective using a Zeiss LSM 780 confocal microscope (Zeiss, Germany). In the somatosensory cortical area of each mouse brain, 3D stacks were obtained. The resolutions of the acquired confocal stacks were set as follows: lateral: 0.041 µm/pixel; axial: 1 µm/pixel. For each mouse, two to three different regions of the somatosensory cortex were imaged and in which 15 dendrites in total were analyzed. The microglia–spine contact ratios were calculated by normalizing the number of microglia–spine contacting points to the enumerated total dendritic spine numbers. The 3D illustrations of microglia–spine interactions were processed using

AutoQuantX3 (Media Cybernetics, USA) and the Surface and Filament module in Imaris 9.3.1 (Bitplane, Switzerland).

2.15 Microglia engulfment analysis

Z-stack confocal images covering 30 μm thickness were acquired at 0.35 μm intervals using a Zeiss LSM780 confocal microscope (Zeiss, Germany) with a 40×/1.4 oil immersion objective and then deconvoluted using AutoQuantX3 (Media Cybernetics, USA) for further 3D analysis. $CD68^+$ lysosomes within the Iba^+ microglia were 3D-reconstructed using the Surface module in Imaris 9.3.1 (Bitplane, Switzerland). $PSD\text{-}95^+$ puncta located within the $CD68^+$ lysosomes were quantified. Eight cortical microglia per mouse from n = 3 mice per group were analyzed.

2.16 Microglia isolation

Microglia were immunomagnetically isolated following the manufacturer's protocols (Miltenyi Biotec, Germany). Briefly, mouse brain cortices were dissected and minced on ice. The minced tissue was enzymatically dissociated using Adult Brain Dissociation Kit containing papain (Miltenyi Biotec, Germany) and further mechanically dissociated by the gentleMACS Octo Dissociator (Miltenyi Biotec, Germany). Tissue debris and red blood cells were subsequently removed with multiple rounds of incubation and centrifugation as instructed in the manufacturer's guidelines. The prepared single-cell suspensions were immediately incubated using MicroBeads (Miltenyi Biotec, Germany) for anti-CD11b (Microglia) and separated on the MACS LS columns on a QuadroMACS Separator (Miltenyi Biotec, Germany). Cells in the $CD11b^+$ fraction were collected and used for the subsequent experiments (Fig.14).

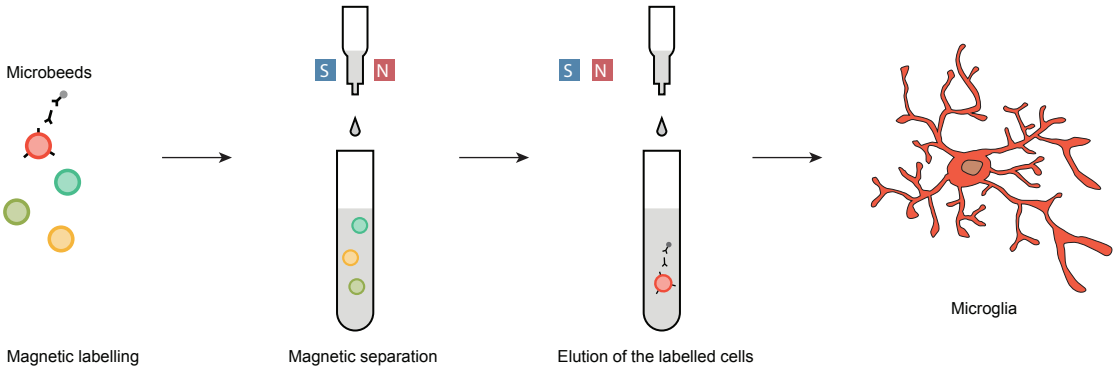

Figure 14. Schematic diagram of magnetic cell separation. Microglia are first magnetic labelled and are retained within the column during the magnetical separation. After washing steps, the magnetic field is removed, and microglia are eluted from the column.

2.17 Enzyme-linked immunosorbent assay

Immunomagnetically isolated cortical microglia from the brains of the indicated animals were resuspended in 100 µL PBS. The cell suspension was lysed by ultrasonication 4 times, then spun at 1,500 × g for 10 min, for subsequent measurement, the supernatant was collected. The concentration of TSPO was measured using the LSBio enzyme-linked immunosorbent assay (ELISA) Kit (Lifespan Biosciences, Inc., USA) according to the manufacturer's instruction. Absorbance at 450 nm was read on an Infinite M200 Pro NanoQuant microplate reader (Tecan, Switzerland). Readouts of TSPO concentration were normalized to the total protein amount, which was determined with bicinchoninic acid assay (Sigma-Aldrich, USA).

2.18 Immunoblotting

For Western blotting, homogenized cortical tissues or immunomagnetically isolated cortical microglia were lysed with Triton X-100 lysis buffer (Alfa Aesar, USA), and the protein levels of the homogenates were quantified by bicinchoninic acid assay (Sigma-Aldrich, USA) and adjusted accordingly. Samples were reduced in blue

loading buffer with 1.25 M dithiothreitol (CST, USA), and ran on 4–15% Mini-PROTEAN TGX precast protein gels (Bio-Rad, USA) or 10–15% Tris-Glycine gels. Gels then were blotted on Immobilon-P polyvinylidene fluoride membranes (Millipore, USA) and blocked with 3–5% skim milk (Sigma-Aldrich, USA). With primary antibodies (anti-PSD-95 (Abcam, 1:1000), anti-PBR (Abcam, 1:10000), anti-$GABA_A$ receptor alpha 1 (Abcam, 1:1000), anti-GAPDH (Cell Signaling Technology, 1:1000)), the membranes were then incubated at 4 °C overnight. Incubation with secondary antibodies (anti-rabbit (Promega, 1:3000), anti-goat (Jackson ImmunoResearch Laboratories, 1:20000)) was conducted at room temperature for 1 h. Membranes were then immersed in Western blotting detection reagent (GE Healthcare, USA) and scanned using a ChemiDoc MP imaging system (Bio-Rad, USA). Optical density was determined and quantified using ImageLab software (Bio-Rad, USA).

2.19 RNA purification and mRNA sequencing

Total RNA was isolated using RNeasy plus micro kit, and QIAcube connect (QIAGEN, Germany). The library preparation and subsequent sequencing were conducted with TruSeq targeted RNA custom panel kit, TruSeq targeted RNA index kit A, and MiniSeq Mid output kit (Illumina, USA), and sequenced on an Illumina MiniSeq sequencer. RNA STAR [237] was used to align the reads to the mouse genome (mm10), and featureCounts [238] was used to perform the subsequent quantification. Differential expression was analyzed using DESeq2 [239] and results with an absolute fold-change >2 and false discovery rate <0.05 were deemed statistically significant and biologically relevant.

2.20 Human tissue sectioning and immunofluorescence staining

For immunohistochemistry analysis, obtained 1 cm thick human tissue blocks were submerged in citrate buffer (10 mM, pH 6.0) overnight to equilibrate to the antigen

retrieval medium, followed by the actual antigen retrieval, which was conducted by incubating tissue blocks in a freshly prepared antigen retrieval solution at 99 °C for 20 min in an Eppendorf Thermomixer with continuous shaking. Afterwards, blocks were collected in PBS and cut into 50 µm thick sections using a VT1000E vibratome (Leica, Germany). Then sections were subjected to a free-floating staining procedure, starting with an over-night gentle shaking incubation in 2% PBTx at 4 °C followed by blocking in a 10% NGS containing 1% PBTx solution for 8 h at room temperature. Afterwards, sections were incubated with primary antibodies (anti-TSPO (Millipore, 1:200), anti-Homer1 (Synaptic Systems, 1:250), and anti-Iba1 (Synaptic Systems, 1:500)) diluted in a 5% NGS containing 0.3% PBTx solution for 72 h at 4°C. Sections were then washed 3 × 15 min in PBS and subsequently incubated with secondary antibodies, diluted in the 0.3% PBTx medium containing 5% NGS, for 2.5 h at room temperature. After an additional 3 times of washing, Aβ plaques were counterstained with methoxy-X04 (10 µg/mL) in 50% ethanol for 15 min. Then sections were washed again and transferred to Sudan black in 70% ethanol for 1.5 min for quenching the autofluorescence of the tissue. Finally, slices were mounted using the fluorescent mounting medium (Dako, Germany) after 3 washing steps. For the acquisition of images, a Zeiss LSM780 confocal microscope (Zeiss, Germany) equipped with a 40×/1.4 oil immersion objective was used.

2.21 Quantification of immunoreactive puncta

For C1q immunoreactive puncta quantification, all images were acquired in a scanned area of 42.43×42.43 µm^2 with a lateral resolution of 0.083 µm using a Zeiss LSM780 confocal microscope (Zeiss, Germany) with a 40×/1.4 oil immersion objective. The numbers of C1q immunoreactive puncta were sampled from two different regions: the layer 2/3 of the somatosensory cortex, and the molecular layer of the dentate gyrus. For each mouse, one image per region was acquired. In order

to quantify the postsynaptic Homer1 and TSPO densities in human cortices identified and plaque presence determined by manually focusing through the whole tissue section in a lower magnification (1× zoom). Five 106.22×106.22 µm² large regions of interest of each of three cortical brain sections per case were imaged individually with 2 times averaging, resulting in 16-bit information containing, 0.052 µm lateral resolution. Images were further processed in Imaris 9.3.1 to quantify the numbers of single punctum and their distribution around plaques with certain sizes. Briefly, C1q, Homer1, or TSPO immunoreactive puncta were measured manually in Slice mode for estimating average XY diameter and quantified in 3D view using the Spot module. Plaques were reconstructed and measured using the Surface module. Areas extending from the outer fringe of plaques, as well as intra-field Homer1 and TSPO spots, were determined and isolated using Matlab (MathWorks, USA). The densities of Homer1 and TSPO spots within corresponding areas were then calculated. These analyses were performed in a blinded manner.

2.22 Small animal PET Imaging

Two separate PET experiments were performed. First, C57BL/6 mice at 3.8 months of age received diazepam treatment by oral syringe (5 mg/kg, daily, n=13, 5 female) or vehicle (n=9, 4 female) two weeks prior to TSPO-PET. Second, APPswe-dE9 and C57BL/6 mice at 5.5 months of age received PLX5622 in food pellets (1200 mg/kg, ad libitum; APP/PS1dE9: n=9, 5 female / C57BL/6: n=10, 6 female) or placebo (AIN-76A control diet, ad libitum; APP/PS1dE9: n=7, 4 female / C57BL/6: n=14, 8 female) over a six week period prior to TSPO-PET.

All small animal PET procedures were performed as previously described [240]. Briefly, [^{18}F]-GE-180 TSPO-PET (12.0 ± 2.5 MBq) with a 60–90 min p.i. emission window was performed using a Siemens Inveon DPET (Siemens, USA). PMOD V3.5 (PMOD technologies, Switzerland) was used to perform all the analyses. Myocardium

correction method [241] was used to normalize the injected activity after global adjustment for therapeutic effects on the myocardial TSPO-PET signal. In order to make the results of both PET experiments comparable, a correction factor for the different ages was introduced via contrasting both C57BL/6 placebo groups (independent from statistical analyses). TSPO-PET readouts were extracted from a whole-brain volume-of-interest [242] and compared between the different groups by one-way ANOVA including Bonferroni post-hoc correction.

2.23 Novel object recognition

The novel object recognition test (NORT) was performed as formerly described [243]. Briefly, animals with or without one-week diazepam treatment were placed in an open-field apparatus (40 x 40 cm) to freely explore for a 10-min habituation trial, and the locomotor activity was recorded by a video-tracking system and assessed using the open field test (OFT). Twenty-four hours after the habituation, the animals were subjected individually to the open-field apparatus with a pair of indistinguishable objects for a 10-min of exploration as the familiarization phase. Twenty-four hours from the previous phase, one of the used objects was replaced by an object with a different shape and colour, and the animals were subjected to a test trial for 5 min. The duration of time that the animals spent on each object were counted as exploration time. The mean exploration times the animals took on the novel and familiar objects were calculated as the ratios and compared through the Wilcoxon signed-rank test.

2.24 Critical commercial assays

Table 13. Commercial assays used in this study.

Commercial assays	Source	Identifier
Mouse TSPO / PBR ELISA Kit	LifeSpan BioSciences	LS-F33263-1
Adult Brain Dissociation Kit	Miltenyi Biotec	130-107-677
CD11b (Microglia) MicroBeads	Miltenyi Biotec	130-093-634
FD Rapid GolgiStain Kit	FD NeuroTechnologies	PK401
Bicinchoninic Acid Kit for Protein Determination	Sigma-Aldrich	BCA1-1KT
TruSeq Targeted RNA Index Kit A	Illumina	RT-402-1001
TruSeq Targeted RNA Custom Panel Kit	Illumina	RT-102-1001
MiniSeq Mid Output Kit	Illumina	FC-420-1004

2.25 Software

Table 14. Software used in this study.

Software	Source	Identifier
AutoQuant X3	Media Cybernetics	http://www.mediacy.com/autoquantx3
Igor Pro 7	WaveMetrics	https://www.wavemetrics.com/products/igorpro
Imaris 9.3.1	Bitplane	https://imaris.oxinst.com
MATLAB	MathWorks	https://www.mathworks.com/products/matlab
Image Lab 6.0.1	Bio-Rad	http://www.bio-rad.com/en-us/product/image-lab-software
PMOD V3.5	PMOD technologies	https://www.pmod.com/
Prism 7	GraphPad	https://www.graphpad.com/scientific-software/prism/
ZEN Imaging Software	Zeiss	https://www.zeiss.com/microscopy/int/products/microscope-software/zen

2.26 Statistics

GraphPad Prism 7 (GraphPad Software, USA) was employed to perform all the statistical analyses. Comparisons between the consecutive *in vivo* two-photon data were performed using the two-way ANOVA test; for illustration and comparison

purpose, the *in vivo* time series data from the diazepam-treated group in Fig.16 are also presented using dash-line in the subsequent figures. Two-tailed Student's *t* test was used for analyzing data between two different groups, and one-way ANOVA followed by Bonferroni's post-hoc test was used for multiple-comparison. Comparisons between the numbers of differently shaped spines were performed using the χ^2 test. Spine head volume data and Sholl analysis data were compared using the Mann-Whitney test. For the analysis of ratios of the animals explored between the novel and familiar objects, the Wilcoxon signed-rank test was performed. Statistical analysis of differential gene expression from RNAseq data was described as above. All data are presented as mean ± s.e.m unless specified otherwise. *p*-value less than 0.05 was defined as statistically significant.

3. Results

3.1 Long-term diazepam treatment impairs the structural plasticity of dendritic spines

3.1.1 Diazepam suppresses mouse locomotor activity

To investigate how diazepam affects dendritic spines, I used GFP-M mice to visualize the apical dendritic tufts originating from pyramidal neurons in cortical layer V region. Mice were administrated with a sedative dose of diazepam (5 mg/kg) which reduced the locomotor activity substantially but not completely (Fig. 15a, b) once daily during the daytime.

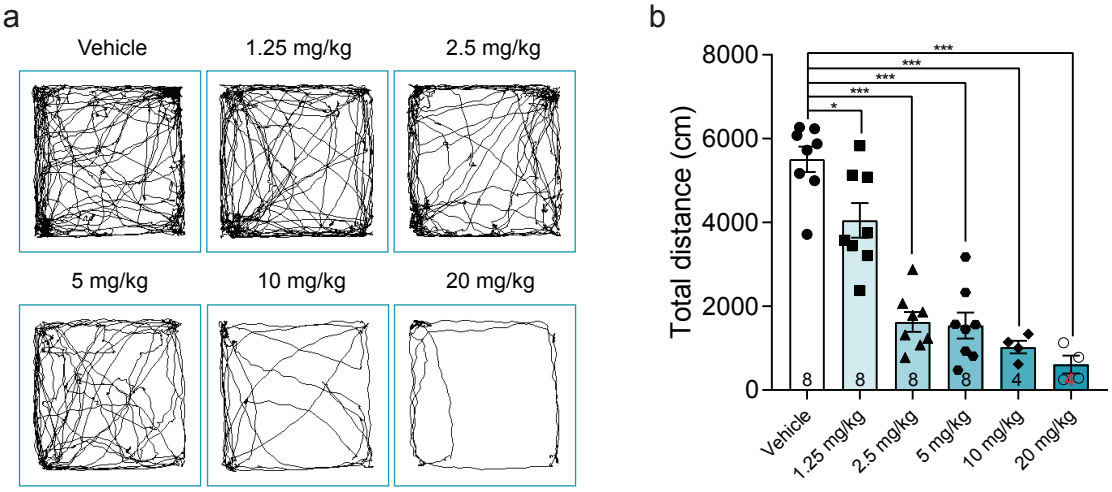

Figure 15. Effects of diazepam on mouse locomotor activity at different doses. a, Representative traces of mouse movement during the 10-minute test period show that diazepam suppresses mouse locomotor activity in a dose-dependent manner. **b**, Respective effects of diazepam (1.25–20 mg/kg, i.g.) on the locomotor activity in mice. Diazepam or vehicle was administered i.g. 15 min before locomotor activity tests. n = 4–8 animals per group as indicated on the bar diagrams. Data are presented as mean ± s.e.m. One-way ANOVA followed by Bonferroni's post-hoc test (**b**). *p<0.05, ***p<0.001.

3.1.2 Diazepam impairs dendritic spine plasticity

Consecutive *in vivo* two-photon imaging was conducted over a period of 78 days before, during, and after diazepam treatment to record the structural plasticity of dendritic spines in comparison with controls administrated with the vehicle (Fig. 16a). Spine density was significantly decreased in diazepam treated mice (Fig. 16b, c), due to moderately suppressed spine formation (Fig. 16d) and highly elevated spine elimination (Fig. 16e). The decrease of dendritic spine density induced by 1-week diazepam treatment lasted for several weeks after drug withdrawal and was followed by a gradual recovery to the baseline within 56 days. However, in mice treated with diazepam for up to 4 weeks, a full restoration of spine density was not observed (Fig. 16h, Fig. 17a-g), indicating that a more prolonged diazepam treatment might rather cause irreversible alterations in the structural plasticity of dendritic spines. The recorded dendritic spines in the initial session of imaging were further tracked and monitored longitudinally to explore how the pre-existing neural networks react to diazepam. Results showed that the survival rate of pre-existing spines was not affected by diazepam (Fig. 16f), while the survival rate of newly formed spines was significantly reduced in diazepam-treated mice (Fig. 16g). These results suggest that diazepam selectively alters those dynamic synaptic structures, which are involved in currently active cognition processes, while pre-existing, already stable synaptic structures remain unaffected.

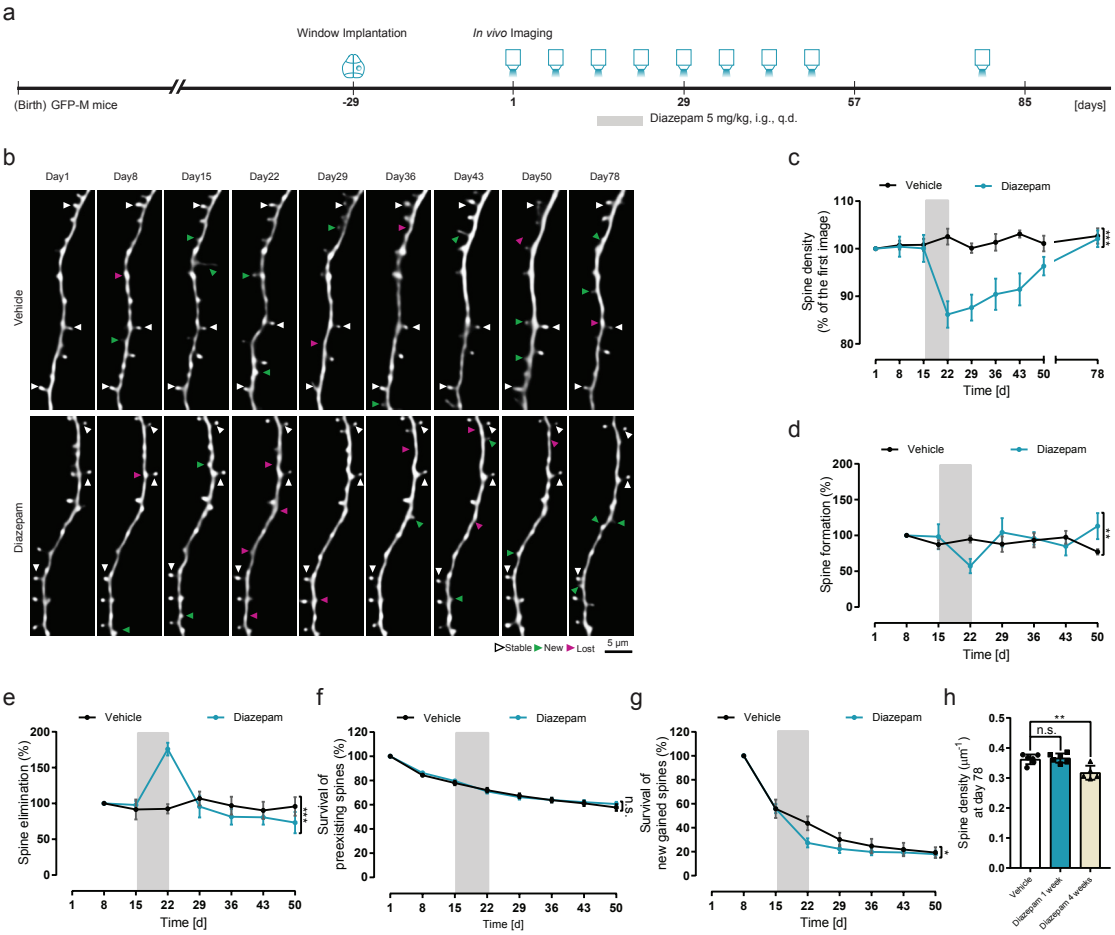

Figure 16. Diazepam alters dendritic spine plasticity *in vivo*. a, Schematic of the experimental design. **b**, Consecutive *in vivo* two-photon micrographs of apical dendritic tufts. Arrowheads denote stable (white), newly gained (green), or lost (magenta) spines. **c**-**g,** Quantifications of relative dendritic spine density (**c**), newly gained (**d**) and lost dendritic spines (**e**), the survival of preexisting spines (**f**) and newly gained spines (**g**) in animals with one-week diazepam or vehicle treatment. **h**, Quantification of spine density at day 78. n = 6 animals per group (**c**-**g**); n = 4–6 animals per group (**h**). Data are presented as mean ± s.e.m. Two-way ANOVA (**c**, **d**, **e**, **f**, **g**); one-way ANOVA with Bonferroni's post-hoc test (**h**). *p<0.05, **p<0.01, ***p<0.001. n.s. – no significant difference. Scale bar = 5 µm.

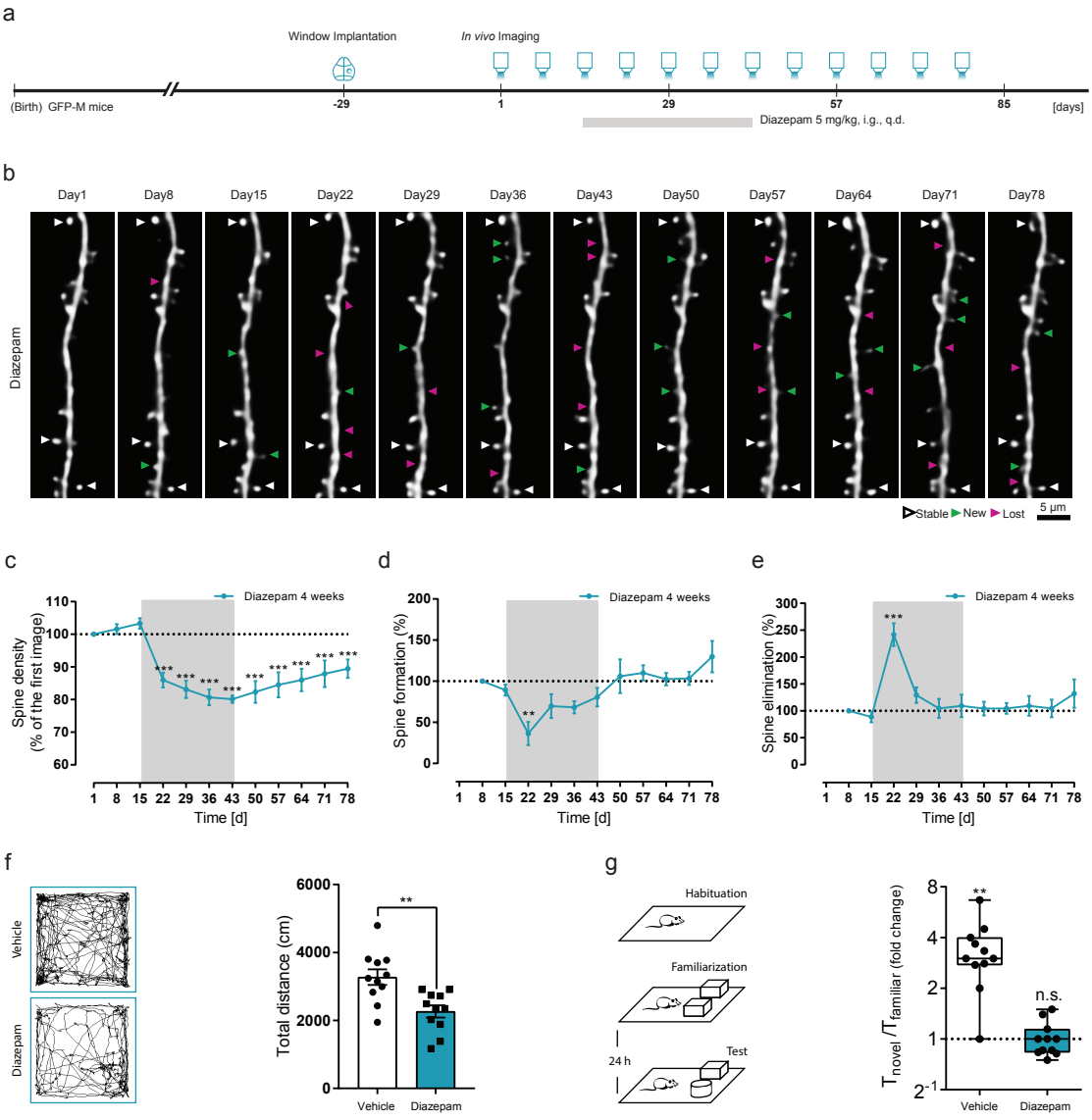

Figure 17. Prolonged diazepam administration impairs the structural plasticity of dendritic spines without short-term recovery after the drug withdrawal. a, Schematic of the experimental design. **b**, Consecutive *in vivo* two-photon micrographs of apical dendritic tufts. Arrowheads denote stable (white), newly gained (green), or lost (magenta) spines. **c**, Spine density is reduced in animals administrated with diazepam. **d** & **e**, The fractions of both gained (**d**) and lost spines (**e**) are altered in four-week diazepam-treated mice. **f**, Total distance travelled during a 10-min OFT. **g**, The ratios of time spent exploring the novel and familiar objects in the NORT. n = 4 animals per group (**c**, **d**, **e**); n = 11 animals per group (**f**, **g**). Data are presented as mean ± s.e.m. Repeated measures one-way ANOVA (**c**, **d**, **e**); two-tailed Student's *t* test (**f**); Wilcoxon signed-rank test (**g**): compared to the hypothetical value 1. ***p*<0.01, ****p*<0.001. n.s. – no significant difference. Scale bar = 5 µm.

3.1.3 Diazepam impairs long-term recognition memory

To evaluate whether the diazepam-impaired dendritic spine plasticity corresponds to perturbed cognitive performance, mice were subjected to the NORT. For evaluating the inter-individual variability as a baseline, mouse exploratory activity was assessed using the OFT. These tests were performed 24 hours after the last diazepam administration and locomotion, as measured by OFT, did not differ significantly between groups (Fig. 18a). In NORT, contrary to vehicle-treated mice, which explored the novel object longer, diazepam-treated mice spent similar time on exploring familiar and novel objects, suggesting a drug-induced decline in memory and cognitive functions (Fig. 18b).

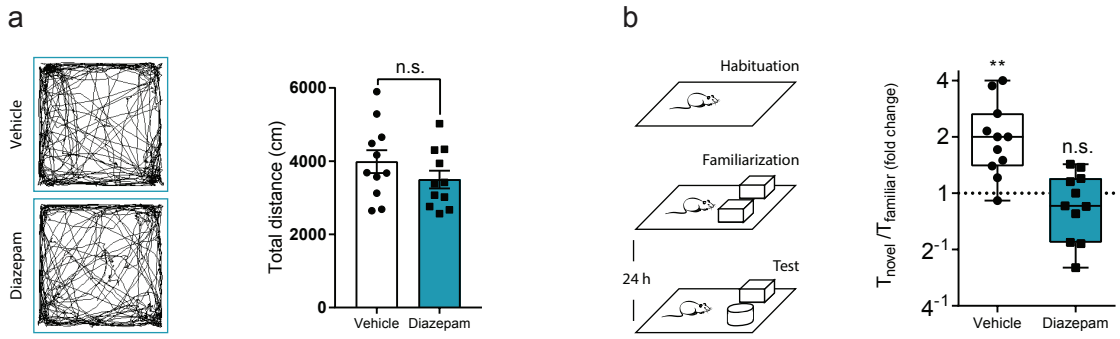

Figure 18. Diazepam impairs long-term recognition memory. a, Total distance travelled during a 10-min OFT. **b**, The ratios of time spent exploring the novel and familiar objects in the NORT. n = 11 animals per group (**a**, **b**). Data are presented as mean ± s.e.m. Two-tailed Student's *t* test (**a**); Wilcoxon signed-rank test (**b**): compared to the hypothetical value 1. ***p*<0.01. n.s. – no significant difference.

Taken together, these experimental data demonstrate that the cognition-related formation and stabilization of synaptic connections are impaired under continual diazepam treatment.

3.2 Diazepam-induced dendritic spine pathology is independent of $GABA_ARs$

3.2.1 Flumazenil fails to block diazepam-induced dendritic spine pathology

Diazepam and other classical benzodiazepines exert their prototypical pharmacological effects by enhancing GABAergic currents through α1, α2, α3, and α5 subtypes of $GABA_ARs$ [11,244]. To investigate whether diazepam-induced synaptic pathology can be attributed to the enhanced GABAergic activity, I chose flumazenil, a competitive inhibitor of benzodiazepines at the $GABA_ARs$, to block the GABAergic effects (Fig. 19a, b).

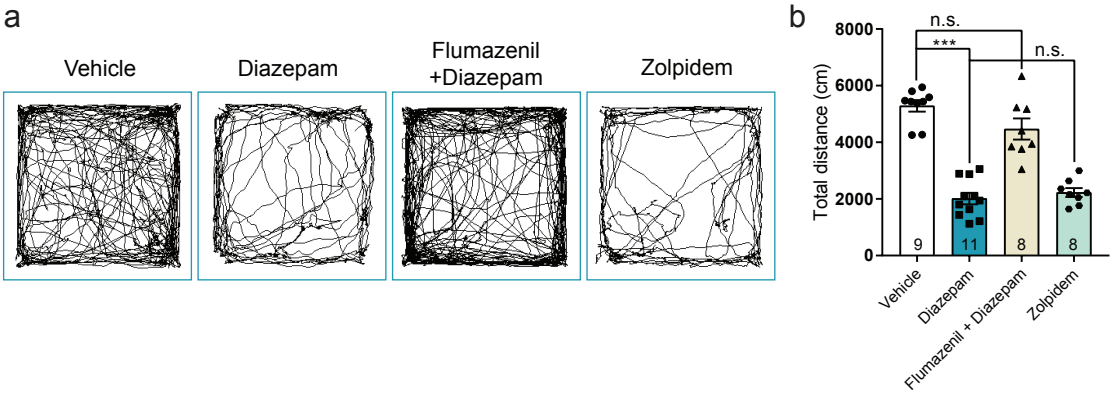

Figure 19. Effects of various compounds on mouse locomotor activity. a, Representative traces of mouse movement during the 10-minute test period in the vehicle, diazepam, flumazenil + diazepam, and zolpidem groups. **b**, Flumazenil blocks the observed effects of diazepam on the mouse locomotor activity, while zolpidem was able to induce similar locomotor sedation as diazepam. Mice were pretreated with flumazenil 15 min before diazepam and 30 min before locomotor activity tests, n = 8–11 animals per group as indicated on the bar diagrams. Data are presented as mean ± s.e.m. One-way ANOVA followed by Bonferroni's post-hoc test (**b**). ***p<0.001. n.s. – no significant difference.

Surprisingly, the effects of diazepam on dendritic spine plasticity persisted (Fig. 20a-f).

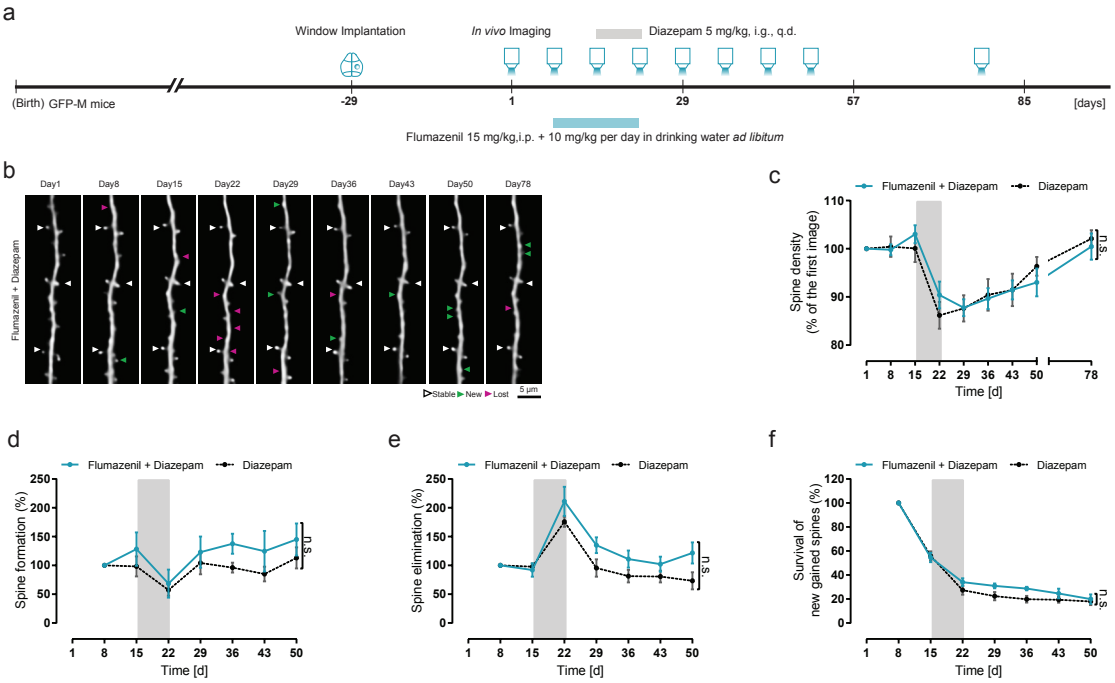

Figure 20. Flumazenil does not block diazepam-altered dendritic spine plasticity. a, Schematic of the experimental design. **b**, Consecutive *in vivo* two-photon micrographs of apical dendritic tufts. Arrowheads denote stable (white), newly gained (green), or lost (magenta) spines. **c**-**f**, Flumazenil cannot block the effects of diazepam on spine density (**c**), spine formation (**d**), spine elimination (**e**), and survival of newly gained spines (**f**). n = 4 animals treated with flumazenil + diazepam (**c**-**f**). Data are presented as mean ± s.e.m. Two-way ANOVA (**c**, **d**, **e**, **f**). n.s. – no significant difference. Scale bar = 5 µm.

3.2.2 Chemogenetic DREADDs cannot phenocopy diazepam-induced dendritic spine pathology

To corroborate this observation, I mimicked diazepam-enhanced GABAergic neuronal inhibition by directly activating parvalbumin (PV)-expressing GABAergic interneurons, which play a central role in regulating cortical oscillations and cognitive information processing [245,246], using the pharmacogenetic tool - DREADDs. PV-Cre x GFP-M mice were injected with pAAV-hSyn-DIO-hM3D(Gq)-mCherry virus to specifically express the pharmacogenetic neuromodulator hM3D on PV interneurons

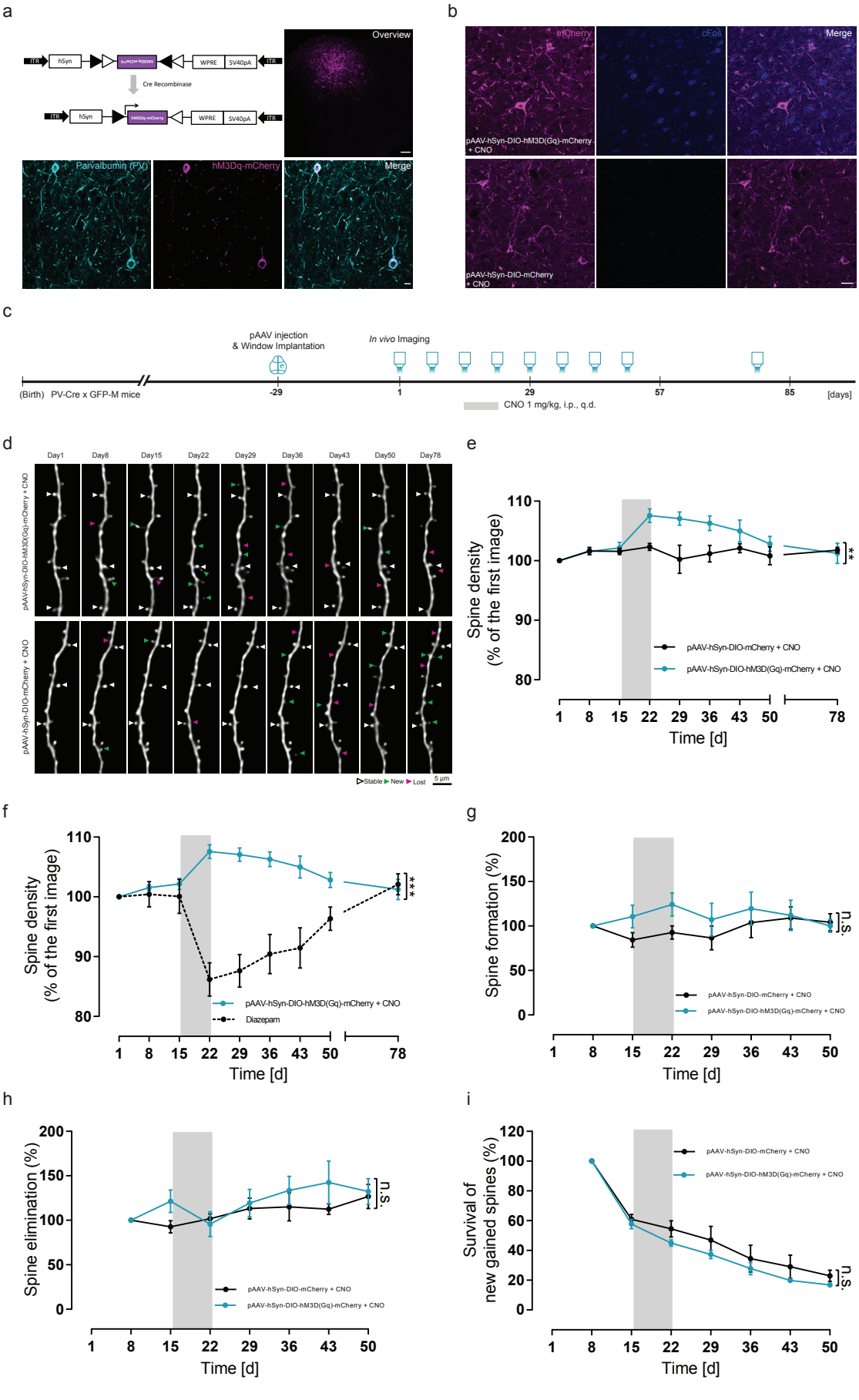
a
ITR
hSyn
WPRE
SV40pA
Cre Recombinase
Overview
Parvalbumin (PV)
hM3Dq-mCherry
Merge
b
mCherry
cFos
Merge
pAAV-hSyn-DIO-hM3D(Gq)-mCherry + CNO
pAAV-hSyn-DIO-mCherry + CNO
c
pAAV injection & Window Implantation
In vivo Imaging
(Birth) PV-Cre x GFP-M mice
-29
1
29
57
85
[days]
CNO 1 mg/kg, i.p., q.d.
d
Day1
Day8
Day15
Day22
Day29
Day36
Day43
Day50
Day78
pAAV-hSyn-DIO-hM3D(Gq)-mCherry + CNO
pAAV-hSyn-DIO-mCherry + CNO
Stable
New
Lost
5 µm
e
Spine density (% of the first image)
pAAV-hSyn-DIO-mCherry + CNO
pAAV-hSyn-DIO-hM3D(Gq)-mCherry + CNO
Time [d]
f
Spine density (% of the first image)
pAAV-hSyn-DIO-hM3D(Gq)-mCherry + CNO
Diazepam
Time [d]
g
Spine formation (%)
n.s.
pAAV-hSyn-DIO-mCherry + CNO
pAAV-hSyn-DIO-hM3D(Gq)-mCherry + CNO
Time [d]
h
Spine elimination (%)
n.s.
pAAV-hSyn-DIO-mCherry + CNO
pAAV-hSyn-DIO-hM3D(Gq)-mCherry + CNO
Time [d]
i
Survival of new gained spines (%)
n.s.
pAAV-hSyn-DIO-mCherry + CNO
pAAV-hSyn-DIO-hM3D(Gq)-mCherry + CNO
Time [d]

Figure 21. CNO-enhanced GABAergic inhibition cannot phenocopy diazepam-impaired structural plasticity of dendritic spines. a, Construct of hM3Dq-mCherry AAV and PV-immunostaining in the cortex of PV-Cre mice expressing hM3Dq. **b**, CNO increases the expression of c-fos in the cortex of PV-Cre mice expressing hM3Dq. **c**, Schematic of the experimental design. **d**, Consecutive *in vivo* two-photon micrographs of apical dendritic tufts in CNO-treated PV-Cre mice inoculated with pAAV-hSyn-DIO-hM3D(Gq)-mCherry or control virus pAAV-hSyn-DIO-mCherry. Arrowheads denote stable (white), newly gained (green), or lost (magenta) spines. **e**, Spine density is increased upon CNO treatment in animals injected with pAAV-hSyn-DIO-hM3D(Gq)-mCherry, while remains unchanged in animals inoculated with control virus pAAV-hSyn-DIO-mCherry. **f**, CNO-enhanced GABAergic inhibition cannot phenocopy diazepam-induced dendritic spine loss. **g**-**i**, CNO treatment alters dendritic spine plasticity in animals inoculated with pAAV-hSyn-DIO-hM3D(Gq)-mCherry. n = 6 animals per group. Data are presented as mean ± s.e.m. Two-way ANOVA (**e**, **f**, **g**, **h**, **i**). ***p*<0.01, ****p*<0.001. n.s. – no significant difference. Scale bars: **a** = 100 µm (upper right), 10 µm (lower panel); **b** = 20 µm; **d** = 5 µm.

in the cortex (Fig. 21a). After the activation of pharmacogenetic neuromodulator hM3D (Fig. 21b) induced by intraperitoneal injection of CNO once daily for one week, with no significant alterations in the control group (pAAV-hSyn-DIO-mCherry + CNO treatment), an ~7.5% increase in spine density was observed, which was opposite to that observed in diazepam-treated animals (Fig. 21c-i).

3.2.3 Zolpidem does not affect dendritic spine plasticity

Next, I tested the effects of zolpidem on dendritic spine plasticity. Zolpidem is a selective benzodiazepine binding site agonist that preferentially binds to $GABA_A$Rs expressing α1 subunit [247] but unlike diazepam, not to the mitochondrial TSPO [248]. The data show that at the previously used equivalence dose of diazepam that causes comparable reductions in locomotor activity (Fig. 19a, b), zolpidem does not interfere with the structural plasticity of dendritic spines (Fig. 22a-f) rather than the induction of an upregulation of $GABA_A$R α1 subunits (Fig. 22g, h).

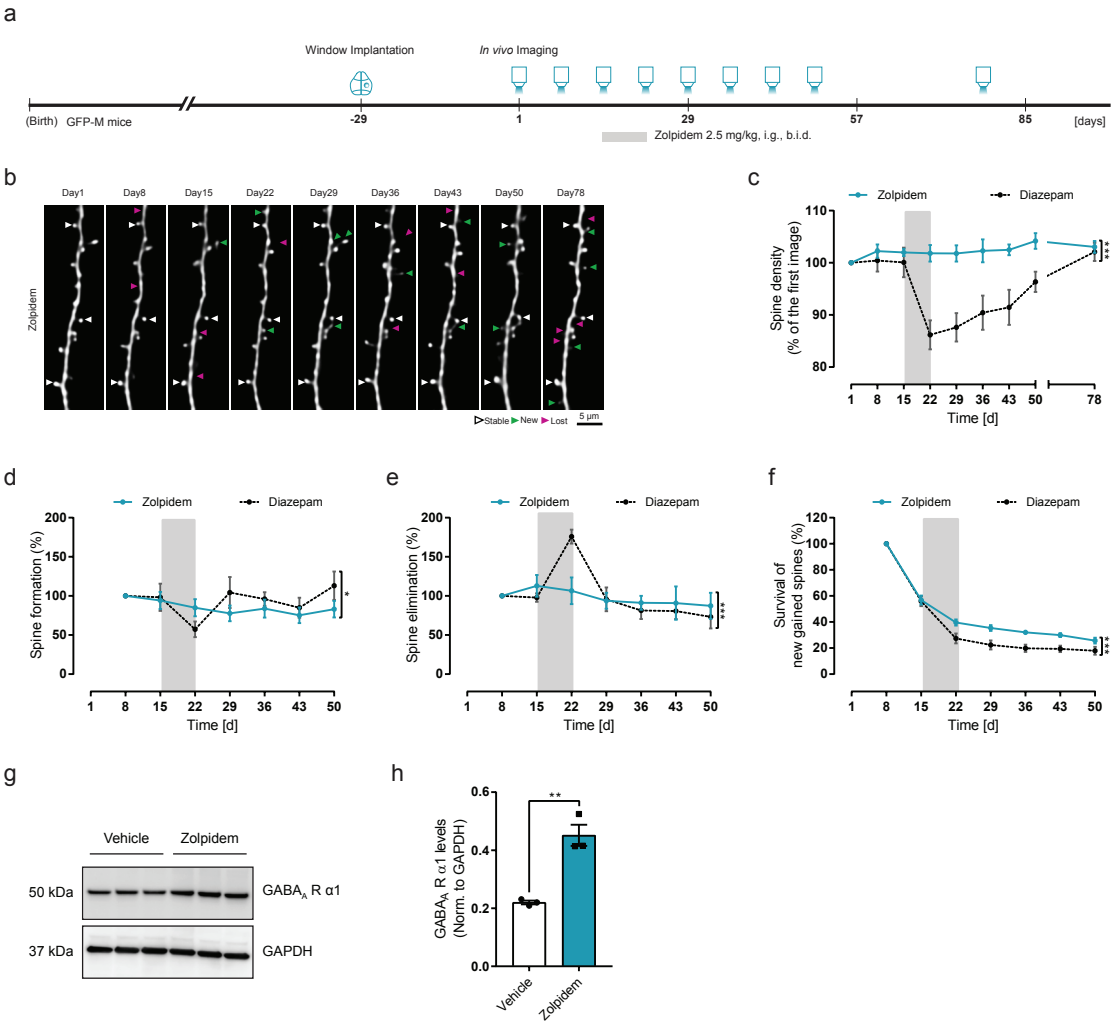

Figure 22. Zolpidem has no effect on the structural plasticity of dendritic spines. a, Schematic of the experimental design. **b**, Consecutive *in vivo* two-photon micrographs of apical dendritic tufts. Arrowheads denote stable (white), newly gained (green) or lost (magenta) spines. **c**, Spine density remains unchanged in animals administrated with zolpidem. **d** & **e**, The fractions of both gained (**d**) and lost spines (**e**) remain unchanged in zolpidem-treated mice. **f**, The survival of newly gained spines is significantly higher from day 22 compared to the diazepam group. **g**, Representative immunoblots for the indicated proteins from one-week zolpidem or vehicle-treated mice whole-brain homogenates. **h**, Quantitation of GABA$_A$ R α1 immunoblots, normalized to GAPDH. n = 6 animals per group (**c**, **d**, **e**, **f**); n = 3 animals per group (**h**). Data are presented as mean ± s.e.m. Two-way ANOVA (**c**, **d**, **e**, **f**); two-tailed Student's *t* test (**h**). **p*<0.05, ***p*<0.01, ****p*<0.001. Scale bar = 5 µm.

3.2.4 Diazepam induces dendritic spine pathology in Gabra RRRR mice

To further confirm the findings, I administrated diazepam to genetically modified *Gabra RRRR* mice. Homozygous *Gabra RRRR* mice carry a point mutation in each α1, α2, α3, and α5 $GABA_AR$ subunits, which changes a histidine residue necessary for benzodiazepine binding to an arginine residue. This occurs physiologically in α4 and α6 subunits, which are naturally insensitive to benzodiazepines. Thus, in these mutant mice, all $GABA_ARs$ are rendered unresponsive to diazepam, while their sensitivity to the physiological neurotransmitter GABA is preserved [9,249,250]. However, a spine loss was still observed in *Gabra RRRR* mice given diazepam (Fig. 23a). The ratios of both mushroom and thin spines showed a (non-significant) trend towards decrease (Fig. 23b). Intriguingly, the overall spine head volume was reduced (Fig. 23c), indicating a decrease in synaptic strength induced by diazepam. I also tested novel object recognition in diazepam treated *Gabra RRRR* mice, which showed a similar impairment in cognitive performance as WT mice (Fig. 23d, e), further confirming that $GABA_ARs$ signify little in diazepam-induced spine loss.

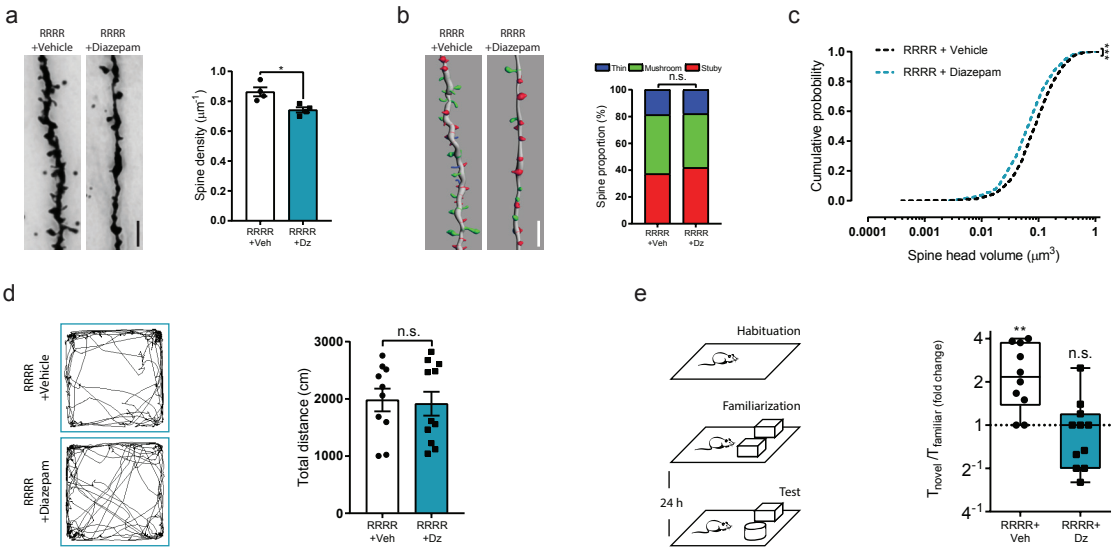

Figure 23. Diazepam alters dendritic spines in *Gabra RRRR* mice. a-c, Diazepam induces spine loss in *Gabra RRRR* mice (**a**), with spine morphologies (**b**) and spine head volumes (**c**) altered. **d**, Total distance travelled during a 10-min OFT by *Gabra RRRR* mice. **e**, The ratios of time spent exploring the novel and familiar objects in the NORT by *Gabra RRRR* mice. n = 4 animals per group (**a**-**c**); n = 10–11 animals per group (**d**, **e**). Data are presented as mean ± s.e.m. Two-tailed Student's *t* test (**a**, **d**); $\chi 2$ test (**b**); Mann-Whitney U test (**c**); Wilcoxon signed-rank test (**e**): compared to the hypothetical value 1. **p*<0.05, ***p*<0.01, ****p*<0.001. n.s. – no significant difference. Scale bar = 5 µm.

In summary, these observations suggest that there is no evidence of direct involvement of $GABA_AR$s in diazepam-induced impairment of the structural plasticity of dendritic spines.

3.3. Diazepam induces dendritic spine pathology via TSPO

3.3.1 XBD173 phenocopies diazepam-induced dendritic spine pathology

In addition to $GABA_AR$s, diazepam also binds to TSPO. To investigate whether diazepam-induced dendritic spine pathology is mediated via TSPO, I chose the specific TSPO ligand XBD173 to modulate TSPO without affecting $GABA_AR$s. Interestingly, XBD173 administration phenocopied diazepam-impaired dendritic spine plasticity (Fig. 24a-f). The impaired dendritic spine plasticity, induced by XBD173 and

diazepam, have a comparable duration (Fig. 24c), decreased spine formation (Fig. 24d) and increased spine elimination (Fig. 24e). A similar decreased survival of newly formed spines was also observed in XBD173-treated mice (Fig. 24f) as in diazepam treated ones.

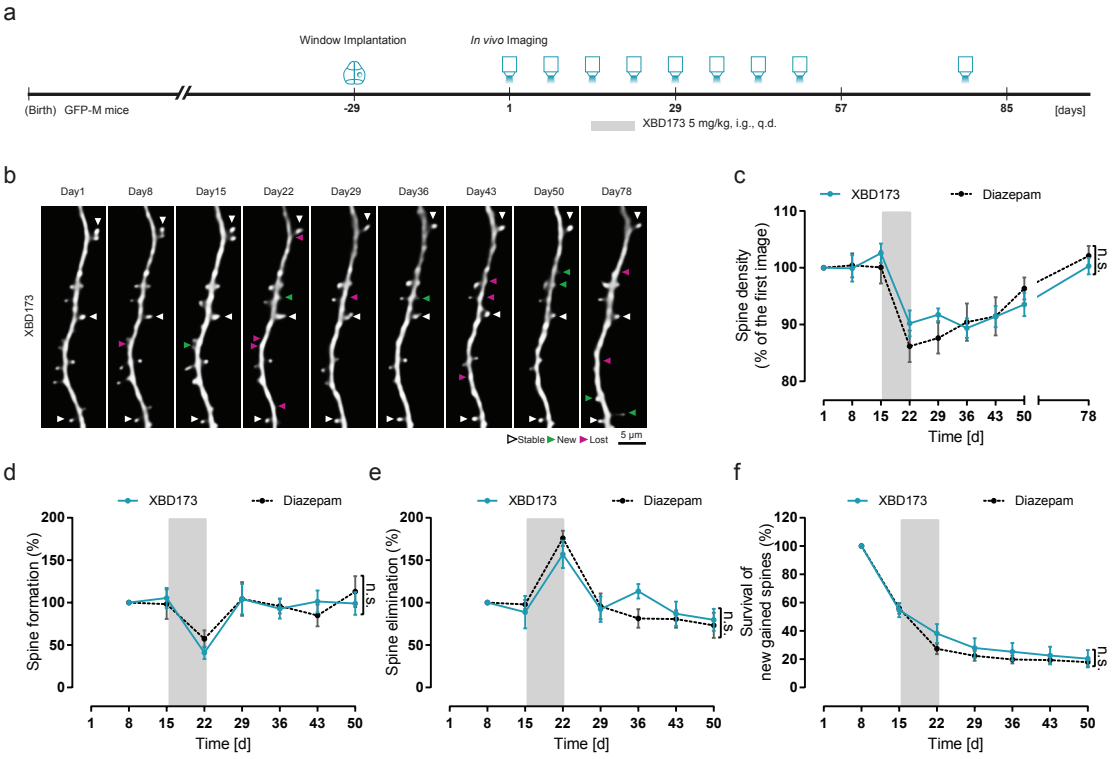

Figure 24. XBD173 alters dendritic spine plasticity. a, Schematic of the experimental design. **b**, Consecutive *in vivo* two-photon micrographs of apical dendritic tufts imaged before, during, and after XBD173 administration. Arrowheads denote stable (white), newly gained (green), or lost (magenta) spines. **c**-**f**, XBD173 alters spine density (**c**), spine formation (**d**), spine elimination (**e**), and survival of newly gained spines (**f**). n = 5 animals treated with XBD173 (**c**-**f**). Data are presented as mean ± s.e.m. Two-way ANOVA (**c**, **d**, **e**, **f**). n.s. – no significant difference. Scale bar = 5 µm.

3.3.2 TSPO deficiency abolishes diazepam-induced dendritic spine pathology

To unequivocally establish the central role of the mitochondrial TSPO in the mechanism by which diazepam impairs the dendritic spine plasticity, I used the extensively characterized *Tspo*$^{-/-}$ mice (Fig. 25) crossed with GFP-M mice as control animals.

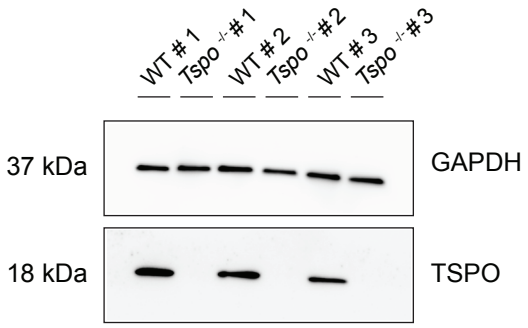

Figure 25. Characterization of TSPO expression in *Tspo* $^{-/-}$ mice. Representative immunoblots showing the complete absence of TSPO in *Tspo* $^{-/-}$ mice.

As illustrated in Fig. 26a-f, in the complete absence of the TSPO, the diazepam-induced dendritic spine loss and alterations in dendritic spine formation and elimination can no longer be observed (Fig. 26c-e). Furthermore, diazepam failed to impair the survival rate of newly formed spines in *Tspo* $^{-/-}$ x GFP-M mice (Fig. 26f), establishing the critical dependence of the non-$GABA_A$Rs-mediated effects of diazepam on the presence of the TSPO.

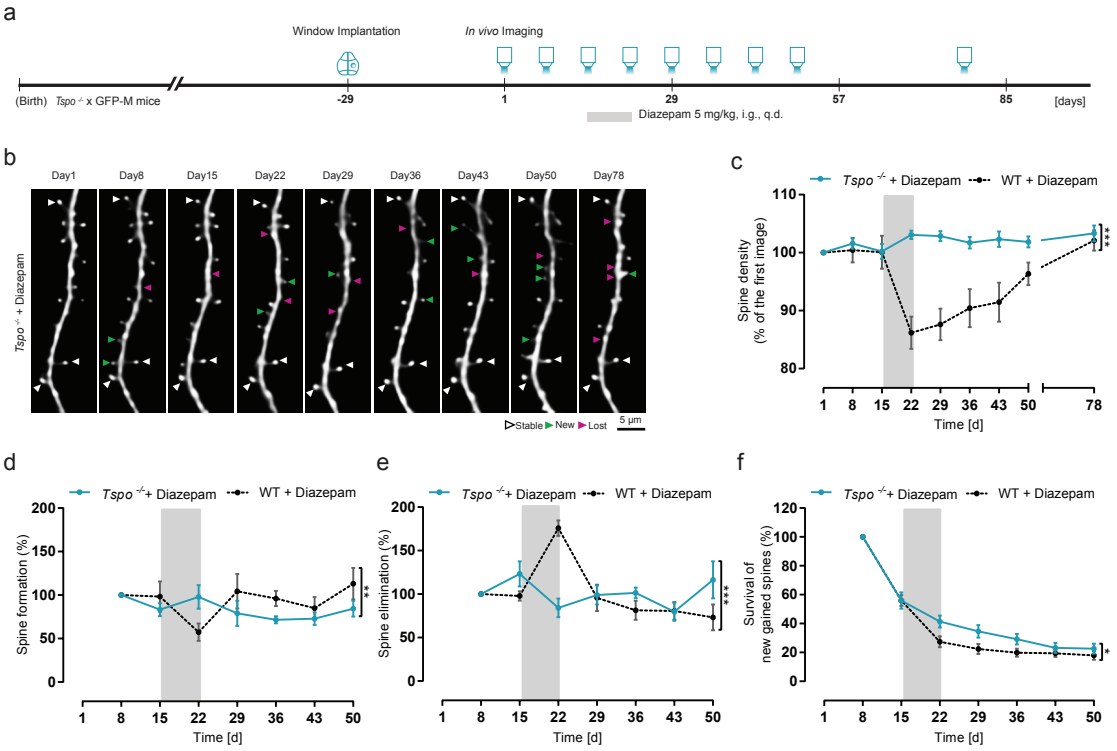

Figure 26. Diazepam alters dendritic spines via TSPO. a, Schematic of the experimental design. **b**-**f**, Consecutive *in vivo* two-photon micrographs of apical dendritic tufts (**b**) show that TSPO deficiency abolishes diazepam-induced dendritic spine loss (**c**), with dendritic spine formation (**d**), elimination (**e**), and survival of newly gained spines (**f**) unaffected. Arrowheads denote stable (white), newly gained (green), or lost (magenta) spines. n = 6 animals in *Tspo* $^{-/-}$ group (**b**-**f**). Data are presented as mean ± s.e.m. Two-way ANOVA (**c**, **d**, **e**, **f**). **p*<0.05, ***p*<0.01, ****p*<0.001. Scale bar = 5 µm.

Furthermore, unlike in diazepam-treated WT mice, the NORT performance of diazepam-treated TSPO deficient mice is comparable to that of vehicle controls (Fig. 27a, b).

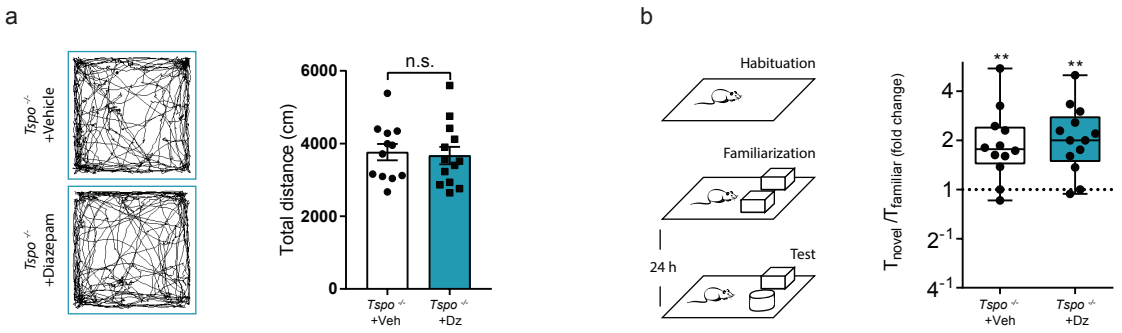

Figure 27. TSPO deficiency abolishes diazepam-impaired long-term recognition memory. a, Total distance travelled during a 10-min OFT by *Tspo* $^{-/-}$ mice. **b**, The ratios of time spent exploring the novel and familiar objects in the NORT by *Tspo* $^{-/-}$ mice. n = 12–13 animals per group (**a**, **b**). Data are presented as mean ± s.e.m. Two-tailed Student's *t* test (**a**); Wilcoxon signed-rank test (**b**): compared to the hypothetical value 1. ***p*<0.01. n.s. – no significant difference.

Together, these observations demonstrate that diazepam impairs the structural plasticity of dendritic spines in a TSPO-dependent manner.

3.4 Diazepam enhances microglial spine engulfment via TSPO

3.4.1 Allopregnanolone cannot phenocopy diazepam-induced dendritic spine pathology

TSPO is a key regulator in various mitochondrial functions in the brain, such as neurosteroid synthesis [34]. Previous studies showed that diazepam and other TSPO ligands increase neurosteroidogenesis in the brain [251]. To check if the impairment of dendritic spine plasticity upon TSPO activation is a consequence of elevated neurosteroid levels, I applied the neurosteroid allopregnanolone to GFP-M mice and longitudinally monitored the dendritic spine plasticity. In contrast to diazepam, one-week of allopregnanolone administration increased dendritic spine density by ~6% (Fig. 28a-f), suggesting diazepam impairs the structural plasticity of dendritic spines independently of enhanced neurosteroidogenesis.

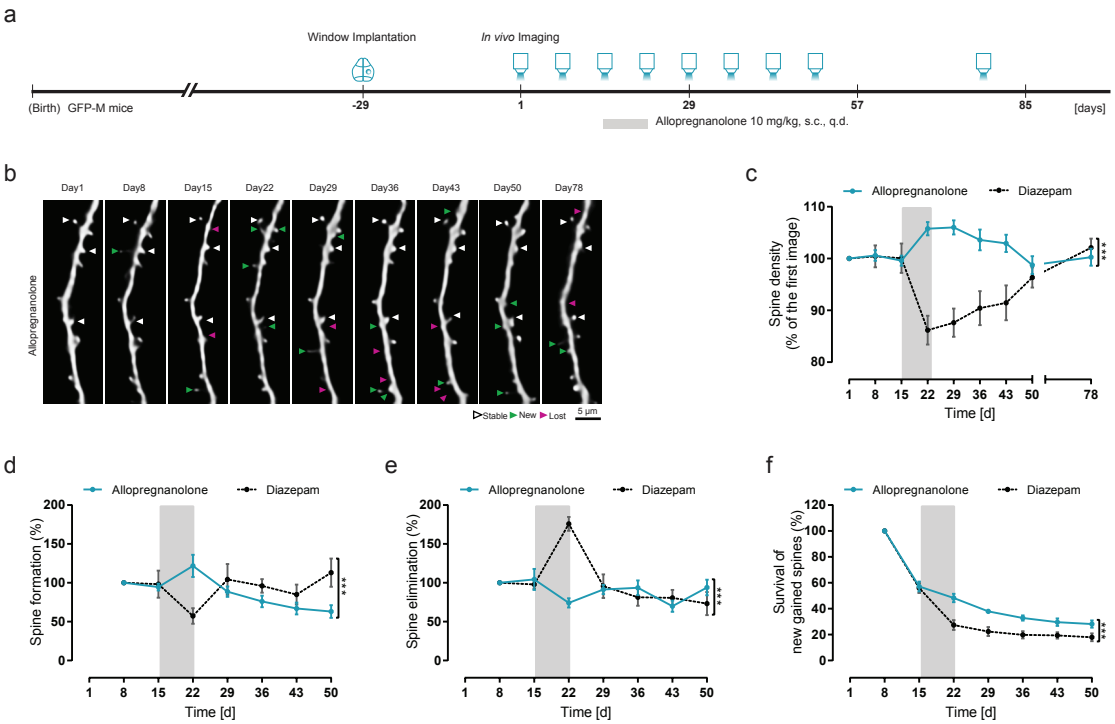

Figure 28. Allopregnanolone alters the structural plasticity of dendritic spines. a, Schematic of the experimental design. **b**, Consecutive *in vivo* two-photon micrographs of apical dendritic tufts imaged before, during, and after allopregnanolone treatment. Arrowheads denote stable (white), newly gained (green), or lost (magenta) spines. **c**, Spine density increases in animals administrated with allopregnanolone. **d** & **e** The fraction of gained spines increases (**d**) and the fraction of lost spines decreases (**e**) in animals administrated with allopregnanolone. **f**, The survival of newly gained spines is significantly higher from day 22 compared to the diazepam group. n = 6 animals. Data are presented as mean ± s.e.m. Two-way ANOVA (**c**, **d**, **e**, **f**). ***p<0.001. Scale bar = 5 µm.

3.4.2 Diazepam alters microglial morphology via TSPO

In the brain, TSPO is highly expressed in microglia [34]. Based on recent findings that microglia exert a vital role in synapse elimination [252,253], I raised the intriguing hypothesis that modulation of TSPO function might result in abnormal synaptic engulfment by microglia. To investigate this possibility, next how diazepam affects microglia via TSPO was explored. Microglial numbers and morphology in WT, *Gabra RRRR*, and *Tspo* $^{-/-}$ mice upon diazepam or vehicle administration were analyzed.

There was no difference in the number of microglia (Fig.30e, Fig.31b), nor was there an overt accumulation of microglia in any of the groups tested (Fig.29a-c).

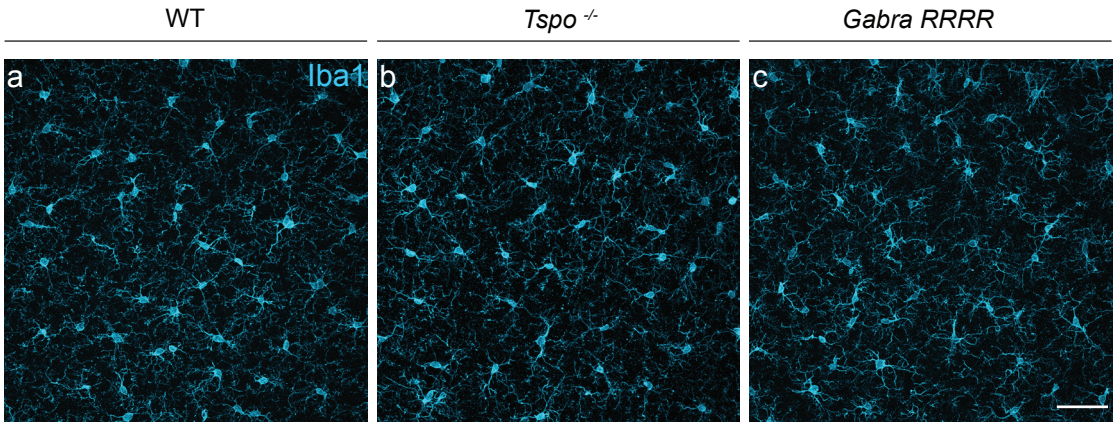

Figure 29. Characterization of microglial morphology in *Tspo* $^{-/-}$ and *Gabra RRRR* mice. a-c, Representative confocal micrographs of cortical Iba1^{+} microglia. No overt accumulation in *Tspo* $^{-/-}$ (**b**) and *Gabra RRRR* mice (**c**) compared to WT mice (**a**). Scale bar = 50 µm.

However, significantly longer processes with bigger process volume, higher segment counts, and more complicated structures were found in microglia from WT mice given diazepam, compared to those from vehicle-treated WT mice (Fig. 31a, c-g). Similar alterations were also observed in *Gabra RRRR* mice (Fig.30a-d, f-j), but not in *Tspo*$^{-/-}$ mice (Fig. 31a, c-g). These morphological data indicate that evident alterations occurred in microglia upon diazepam treatment, which is mediated by TSPO.

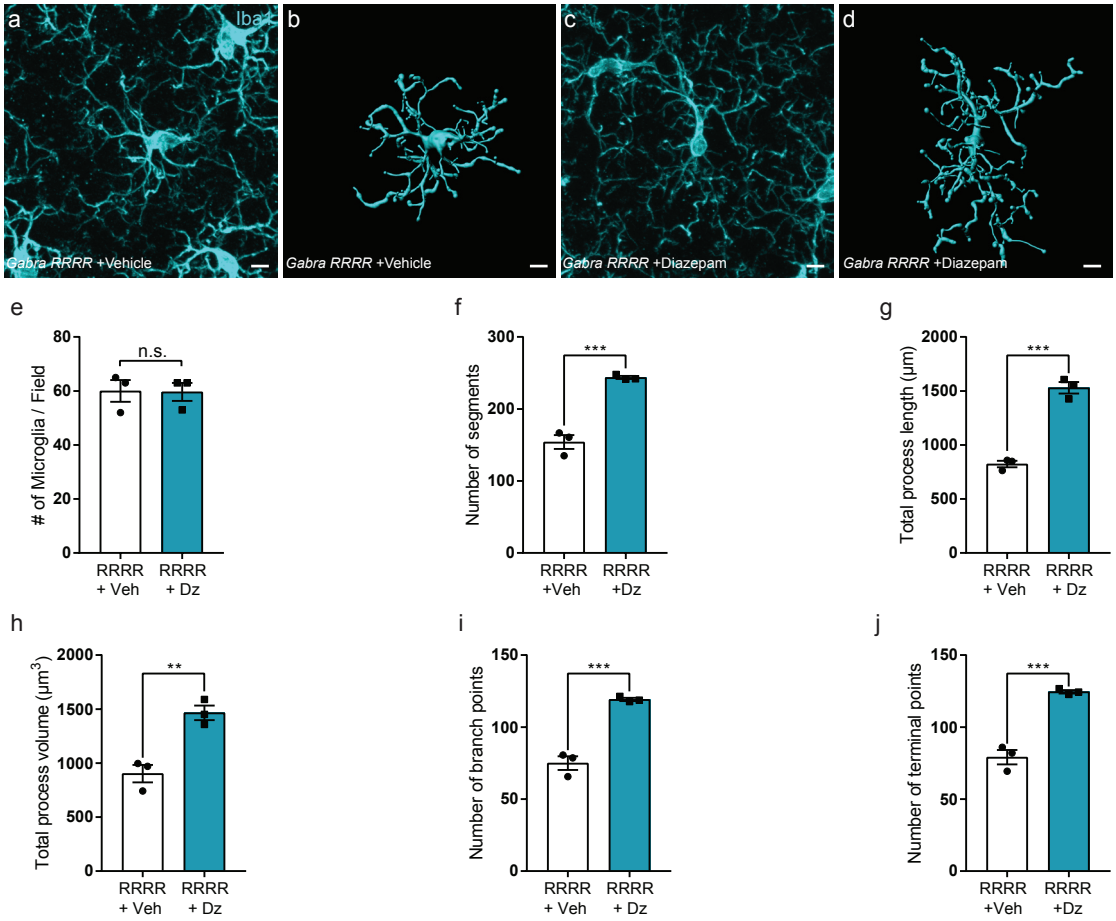

Figure 30. Diazepam alters microglial morphology in *Gabra RRRR* mice. a-d, Representative confocal micrographs and 3D reconstruction of cortical Iba1$^+$ microglia in *Gabra RRRR* mice with one-week diazepam or vehicle treatment. **e**, No changes in microglia numbers between diazepam and vehicle-treated *Gabra RRRR* mice. **f-j**, Morphometric analysis of microglia in *Gabra RRRR* mice with one-week diazepam or vehicle treatment. n = 3 animals per group. Data are presented as mean ± s.e.m. Two-tailed Student's *t* test (**e**, **f**, **g**, **h**, **i**, **j**). ***p*<0.01, ****p*<0.001. n.s. – no significant difference. Scale bar = 5 µm.

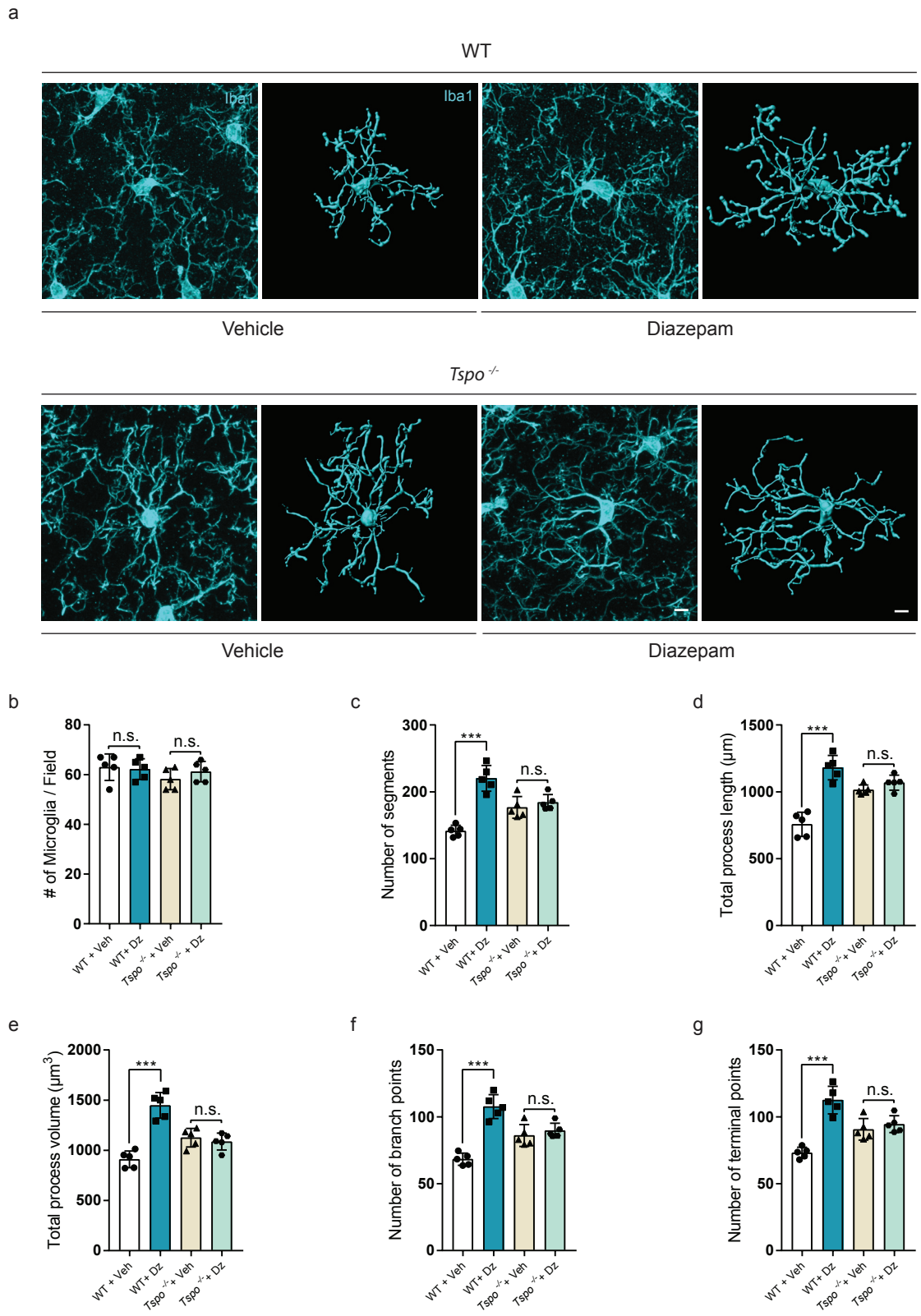
a
WT
Iba1
Iba1
Vehicle
Diazepam
Tspo -/-
Vehicle
Diazepam
b
# of Microglia / Field
n.s.
n.s.
c
Number of segments
***
n.s.
d
Total process length (µm)
***
n.s.
e
Total process volume (µm3)
***
n.s.
f
Number of branch points
***
n.s.
g
Number of terminal points
***
n.s.
WT + Veh
WT+ Dz
Tspo -/- + Veh
Tspo -/- + Dz

Figure 31. Diazepam alters microglia morphology via TSPO. a, Representative confocal micrographs and 3D reconstruction of cortical Iba1$^+$ microglia. **b**-**g**, Morphometric analysis of microglia. n = 5 animals per group (**b**-**g**). Data are presented as mean ± s.e.m. One-way ANOVA with Bonferroni's post-hoc test (**b**, **c**, **d**, **e**, **f**, **g**). ***p<0.001. n.s. – no significant difference. Scale bar = 5 µm.

3.4.3 Diazepam increases microglia–spine interactions

To examine the functional consequences of diazepam-induced microglial response, I analyzed the microglia–spine interactions upon one-week diazepam administration. Functionally, microglial processes constantly monitor the environment and activity-dependently contact with synapses, which subsequently increases the turnover of synaptic connections [254]. Iba1-labelled microglial processes were in constant contact with eGFP-labelled postsynaptic spines (Fig. 32a-d). Diazepam administration significantly increased the microglia–spine interactions in WT mice, but not in *Tspo* $^{-/-}$ mice (Fig. 32e).

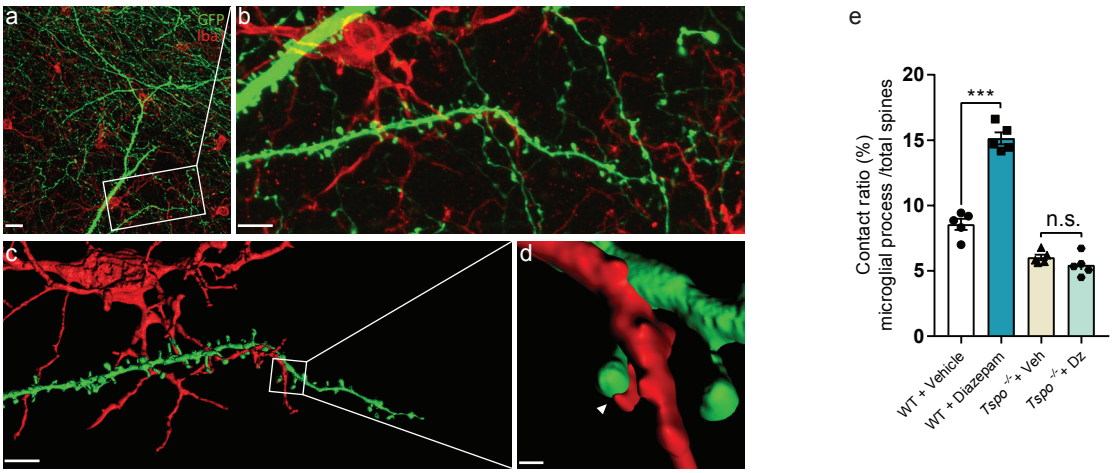

Figure 32. Diazepam increases microglia–spine interactions. a-**e**, 3D reconstruction of GFP-labelled dendrites (green)–Iba1$^+$ microglia (red) interaction (**a**-**d**) and the quantification (**e**). n = 5 animals per group (**e**). Data are presented as mean ± s.e.m. One-way ANOVA with Bonferroni's post-hoc test (**e**). ***p<0.001. n.s. – no significant difference. Scale bars: **a** = 10 µm; **b** = 5 µm; **c** = 5 µm; **d** = 0.5 µm.

3.4.4 Microglial engulfment of PSD-95^{+} puncta

To further examine whether more postsynaptic material is engulfed by microglia upon diazepam administration, I quantified immunostained postsynaptic PSD-95^{+} puncta present within CD68^{+} microglial lysosomes. The relative number of PSD-95^{+} puncta engulfed inside the microglial lysosomes in cortex region from WT animals administrated with diazepam was increased by ~1.5-fold, but remained unchanged in *Tspo* $^{-/-}$ mice (Fig. 33a, b). Such observations were further confirmed by Western blotting. Immunomagnetically isolated cortical microglia from one-week diazepam or vehicle-treated WT and *Tspo* $^{-/-}$ mice were analyzed. In these highly purified microglia, a higher level of PSD-95 in WT animals administrated with diazepam was observed, but not in *Tspo* $^{-/-}$ mice (Fig. 33c).

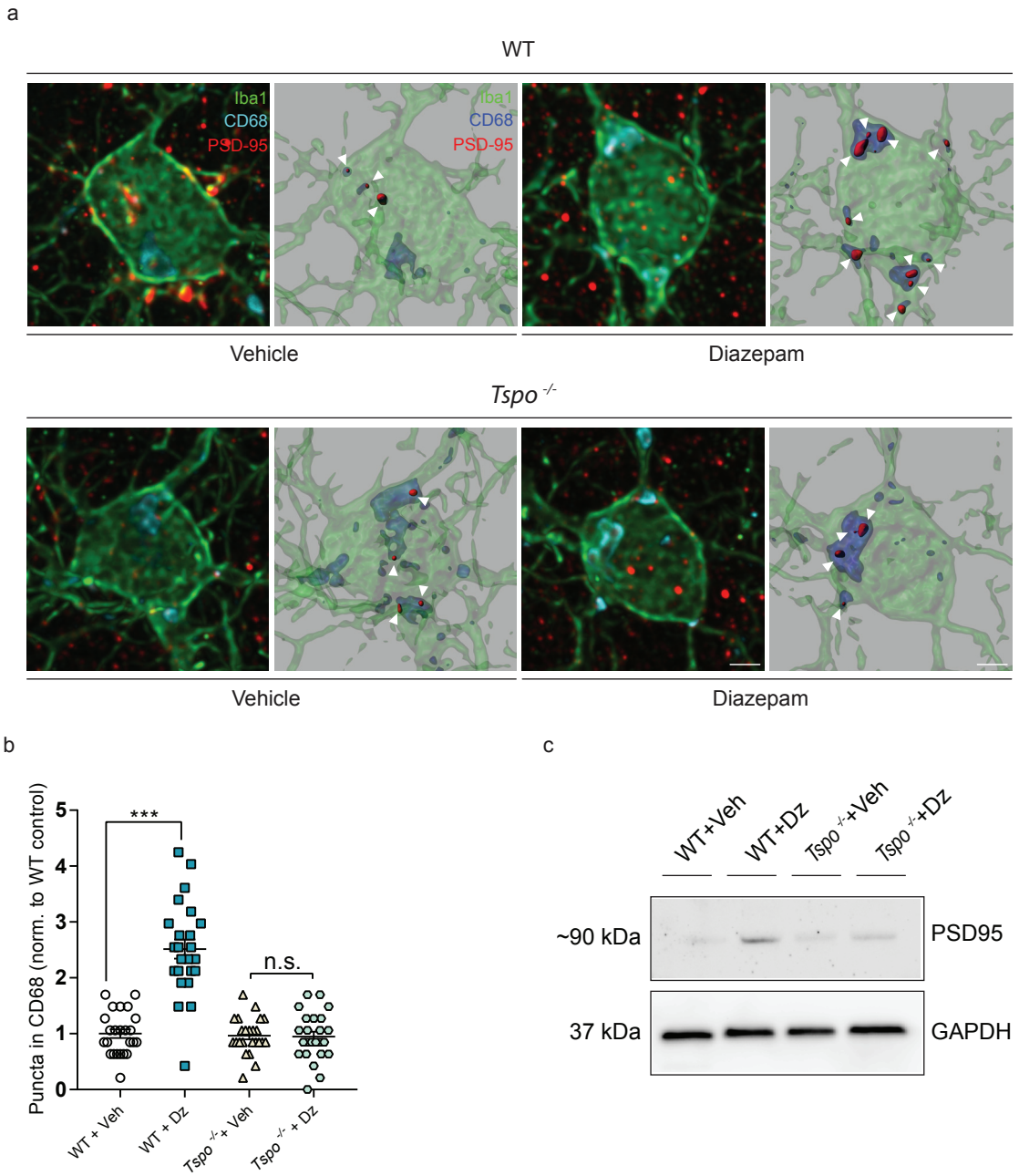

Figure 33. Diazepam induces excessive microglial spine engulfment. a, 3D reconstruction of the PSD-95^{+} puncta engulfed in CD68^{+} microglial lysosomes in diazepam- or vehicle-treated WT or *Tspo* $^{-/-}$ animals. **b**, Quantitation of the PSD-95^{+} puncta engulfed in CD68^{+} lysosomes, normalized to vehicle-treated mice. **c**, Immunoblots of microglial PSD-95. n = 5 animals per group (**b**). Data are presented as mean ± s.e.m. One-way ANOVA with Bonferroni's post-hoc test (**b**). ***p<0.001. n.s. – no significant difference. Scale bar = 5 µm.

3.4.5 Accumulation of complement C1q

To extend the investigations to a more fundamental level, I performed targeted RNA sequencing in isolated cortical microglia from WT and *Tspo* $^{-/-}$ mice with diazepam or vehicle treatment. Synapse-associated C1q, the component that initiates the classical complement pathway, was significantly upregulated in WT animals administrated with diazepam, but not in *Tspo* $^{-/-}$ mice (Fig.34a, b). C1q deposition on synapses is thought to drive microglial synapse engulfment, which contributes to the elimination of dendritic spines [175]. The synaptic C1q immunoreactivity was further confirmed by immunohistochemistry (Fig.34c). Quantification of C1q-positive puncta showed a significant elevation of C1q in cortical area and dentate gyrus of hippocampal area from WT mice with diazepam administration, while similar alterations were not observed in *Tspo* $^{-/-}$ mice (Fig. 34d, e).

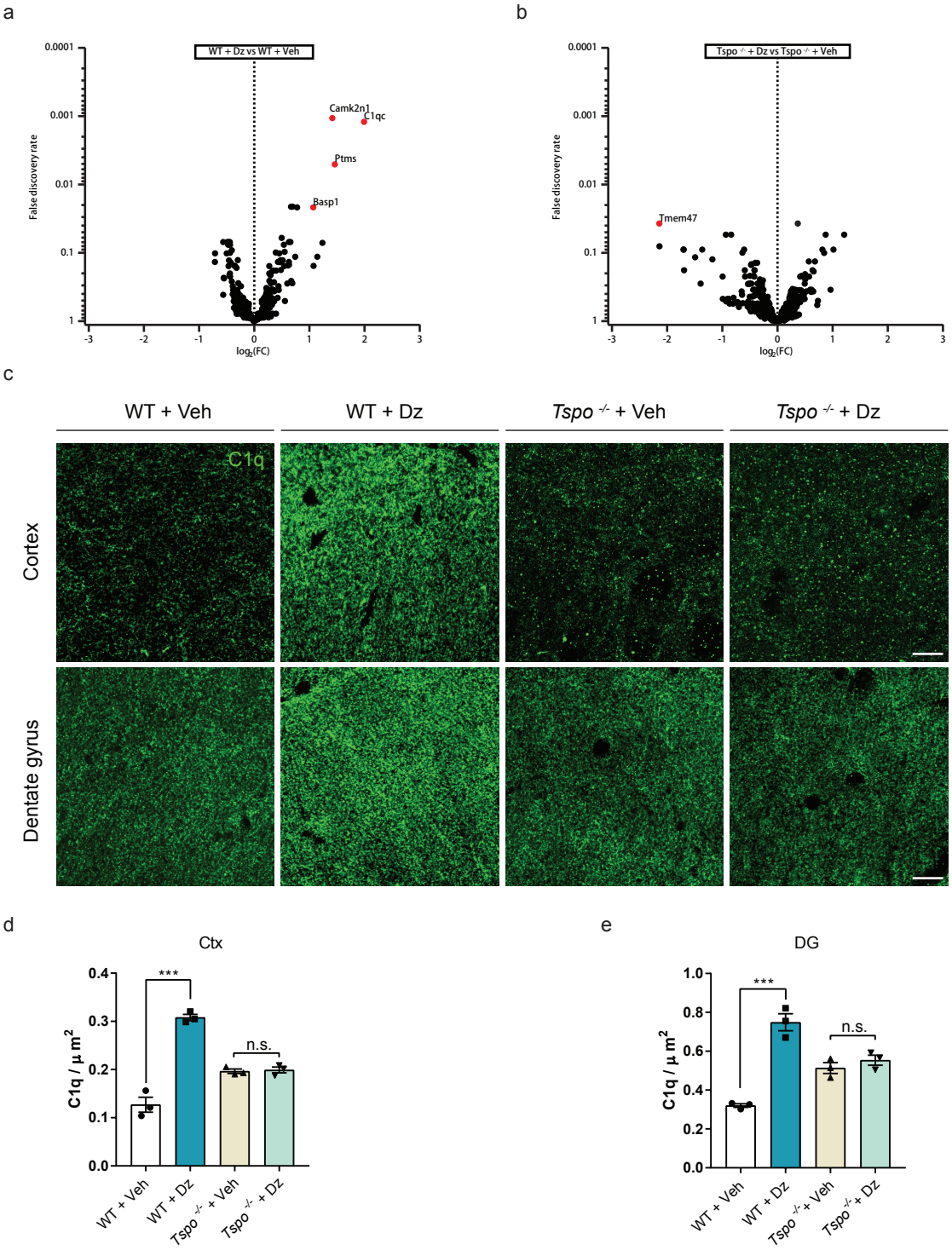

Figure 34. C1q accumulates in the diazepam-treated mouse brain. a & **b**, RNA sequencing. **c**, Representative confocal micrographs from C1q immunohistochemistry in animals with one-week diazepam or vehicle treatment. **d** & **e**, Quantification of C1q$^+$ puncta in the cortex (**d**) and dentate gyrus (**e**) of animals administrated with vehicle or diazepam. n = 3 animals per group (**a**, **b**, **d**, **e**). Data are presented as mean ± s.e.m. One-way ANOVA with Bonferroni's post-hoc test (**d**, **e**). ***p<0.001. n.s. – no significant difference. Scale bar = 10 µm.

3.4.6 PLX5622 abolishes diazepam-induced microglial synaptic engulfment *in vivo*

In addition, to confirm that diazepam induces microglial synaptic engulfment *in vivo*, I took advantage of a selective inhibitor of colony-stimulating factor 1 receptor (CSF1R) to eliminate resident microglia from adult mouse brain [255]. Application of the CSF1R inhibitor, PLX5622, for six weeks reduced microglia numbers by >95% (Fig. 35a-c), without affecting astrocytes or neurons (Fig. 36a-k).

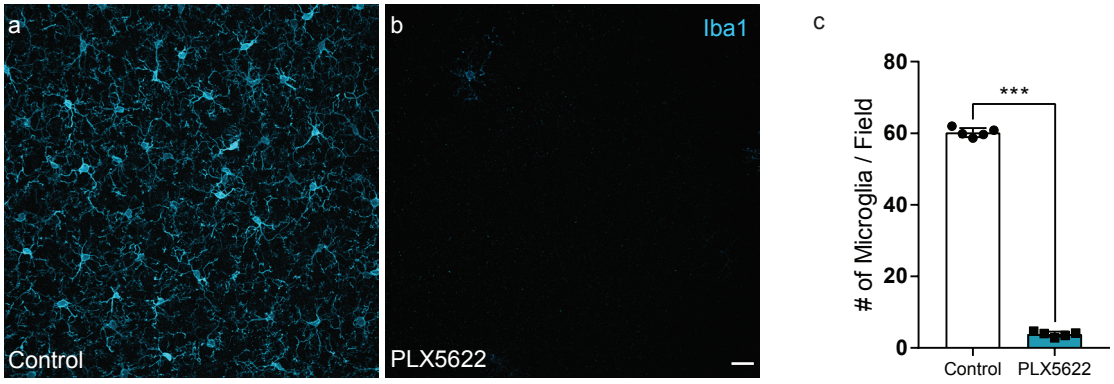

Figure 35. Long-term PLX5622 treatment eliminates microglia from the adult mouse brain. a & **b**, Representative confocal micrographs show that full elimination of microglia in animals treated with PLX5622 for 6 weeks (**b**) compare to control diet treated animals (**a**). **c**, Quantification of Iba^+ cell bodies in the somatosensory cortex as shown were performed via Imaris spot counts and shown in (**c**), revealing robust decreases in microglial numbers. n = 5 animals per group. Data are presented as mean ± s.e.m. Two-tailed Student's *t* test (**c**). ****p*<0.001. Scale bar = 20 μm.

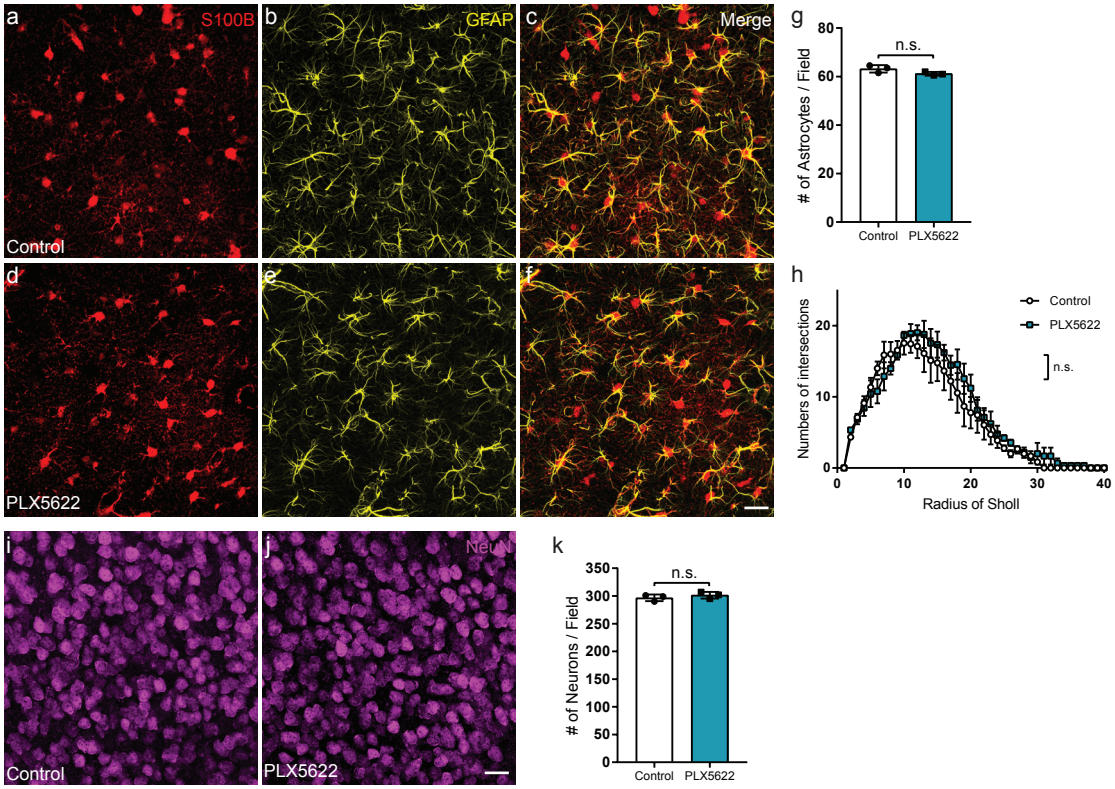

Figure 36. Long-term microglia elimination does not affect astrocytes or neurons. a-**h**, Brain sections from 3–4 month-old WT mice fed with 6-week PLX5622 or control diet were stained with the astrocytic markers GFAP and S100B. Representative confocal micrographs from control (**a**-**c**) and PLX5622 (**d**-**f**) groups are shown. **g**, Quantification of GFAP and S100B double-positive cells encompassing the hippocampus as shown were performed via Imaris spot counts and shown in (**g**), revealing no changes. **h**, Sholl analysis. **i** & **j**, Brain sections were stained with the neuronal marker NeuN. Representative confocal micrographs from control (**i**) and PLX5622 (**j**) groups are shown. **k**, Relative numbers of NeuN$^+$ cells per field in the somatosensory cortex as shown were performed via Imaris spot counts and shown in (**k**), revealing no changes. n = 3 animals per group. Data are presented as mean ± s.e.m. Two-tailed Student's *t* test (**g**, **k**); Mann-Whitney U test (**h**). n.s. – no significant difference. Scale bar = 20 µm.

No changes in spine density, formation, or elimination were observed upon one-week diazepam administration in microglia-depleted mice (Fig. 37a-e). Moreover, the survival rate of newly formed spines in microglia-depleted mice remained unchanged upon diazepam treatment (Fig. 37f).

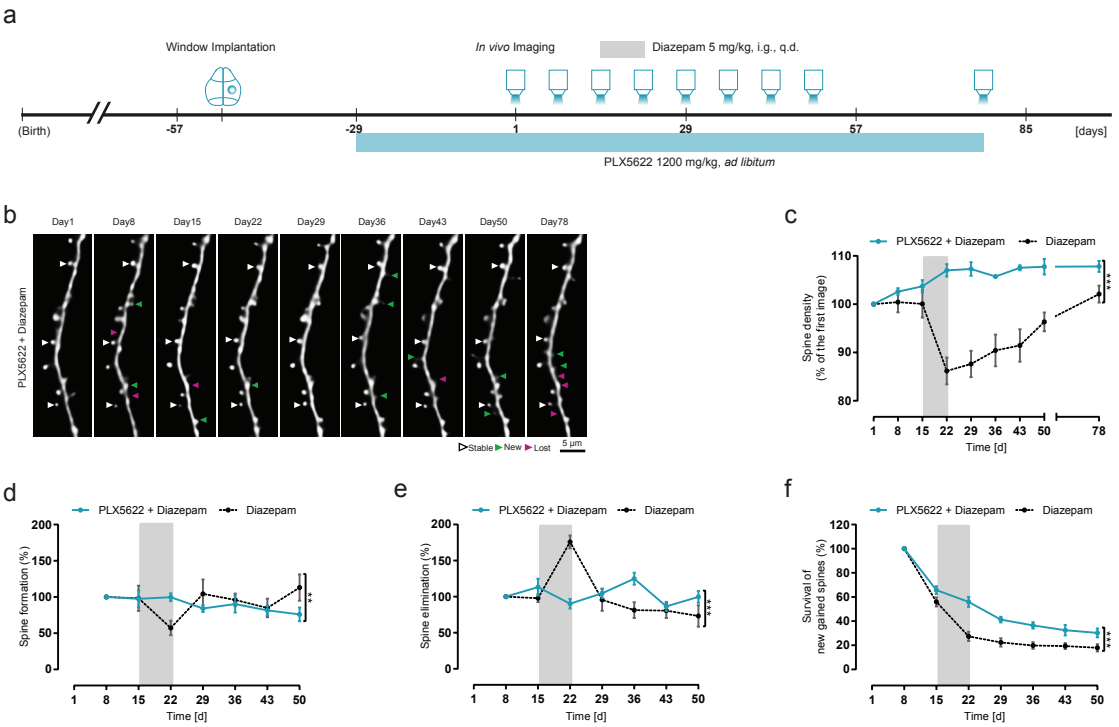

Figure 37. Microglial depletion abolishes diazepam-induced dendritic spine loss. a, Schematic of the experimental design. **b**-**f**, Consecutive *in vivo* two-photon micrographs of apical dendritic tufts (**b**) show that globally microglia depletion abolishes diazepam-induced dendritic spine loss (**c**), with dendritic spine formation (**d**), elimination (**e**), and survival of newly gained spines (**f**) unaffected. n = 5 animals in PLX5622 + diazepam-treated group (**c**, **d**, **e**, **f**). Data are presented as mean ± s.e.m. Two-way ANOVA (**c**, **d**, **e**, **f**). ***p*<0.01, ****p*<0.001. Scale bar = 5 µm.

Collectively, results of RNA-sequencing and imaging show multiple diazepam-induced alterations in microglia, which subsequently cause excessive microglial synaptic engulfment.

3.5 TSPO deficiency eases dendritic spine pathology in AD

3.5.1 TSPO positron emission tomography

Emerging PET studies show upregulation of TSPO in AD brains [67,240,256], although its role in pathogenesis remains inconclusive. Having demonstrated that TSPO mediates diazepam-induced impairment of dendritic spine plasticity, I investigated whether there are similarities in the induction of TSPO expression in diazepam-

treated mice and AD mouse brains using small-animal PET imaging and ELISA. Fig. 38 illustrates an elevation of TSPO in both diazepam-treated WT mice (Fig. 38a, b, e) as well as in a mouse model of AD (Fig. 38c, d, e). The depletion of microglia by the CSF1R inhibitor, PLX5622, resulted in a significant reduction of the TSPO PET-signal, suggesting that the *in vivo* measured TSPO binding is closely associated with the *de novo* expression of TSPO by disease-activated microglia (Fig. 38c, d).

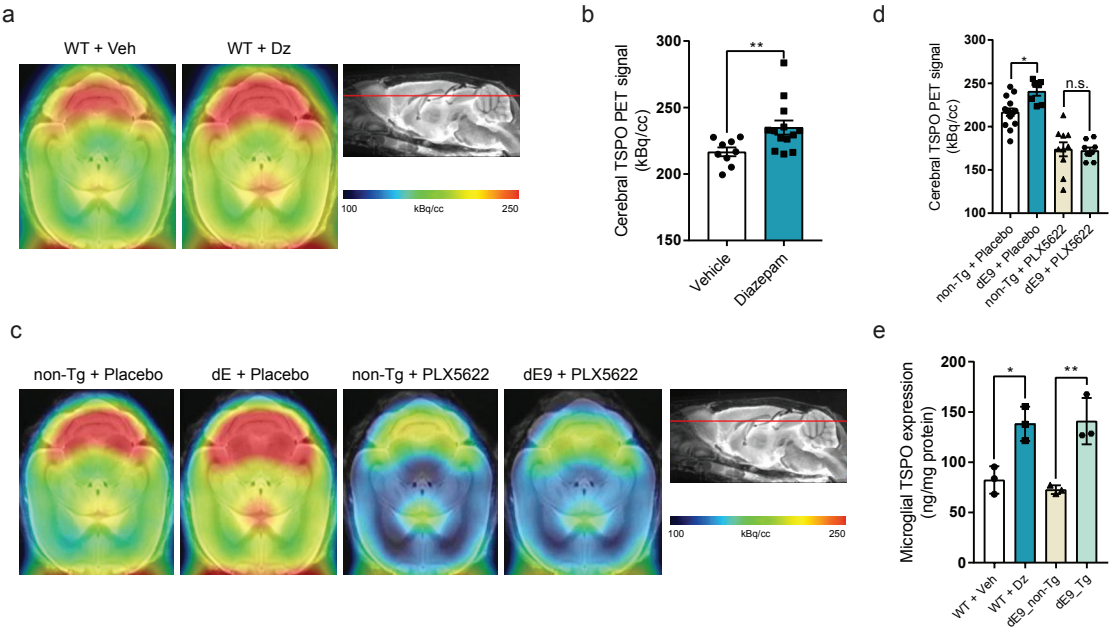

Figure 38. TSPO elevates in both diazepam-treated and AD mouse brains. a-d, Representative PET images (scaled by myocardium correction and projected upon an MRI template) in axial planes and quantifications are shown for diazepam/vehicle-treated WT mouse brains (**a**, **b**) and PLX5622/vehicle-treated dE9/non-Tg mouse brains (**c**, **d**). **e**, Quantitation of microglial TSPO by ELISA. n = 9–13 animals per group (**b**); n = 7–14 animals per group (**d**); n = 3 animals per group (**e**). Data are presented as mean ± s.e.m. Two-tailed Student's *t* test (**b**); one-way ANOVA with Bonferroni's post-hoc test (**d**, **e**). **p*<0.05, ***p*<0.01. n.s. – no significant difference.

3.5.2 Characterization of TSPO expression in APPswe/PS1deltaE9 mice

Fluorescent immunostaining for TSPO and specific cellular markers in brain sections from APPswe/PS1deltaE9 mice further revealed that TSPO co-localized mainly with Iba1$^+$ microglia, rather than with astrocytes or neurons (Fig. 39a-m).

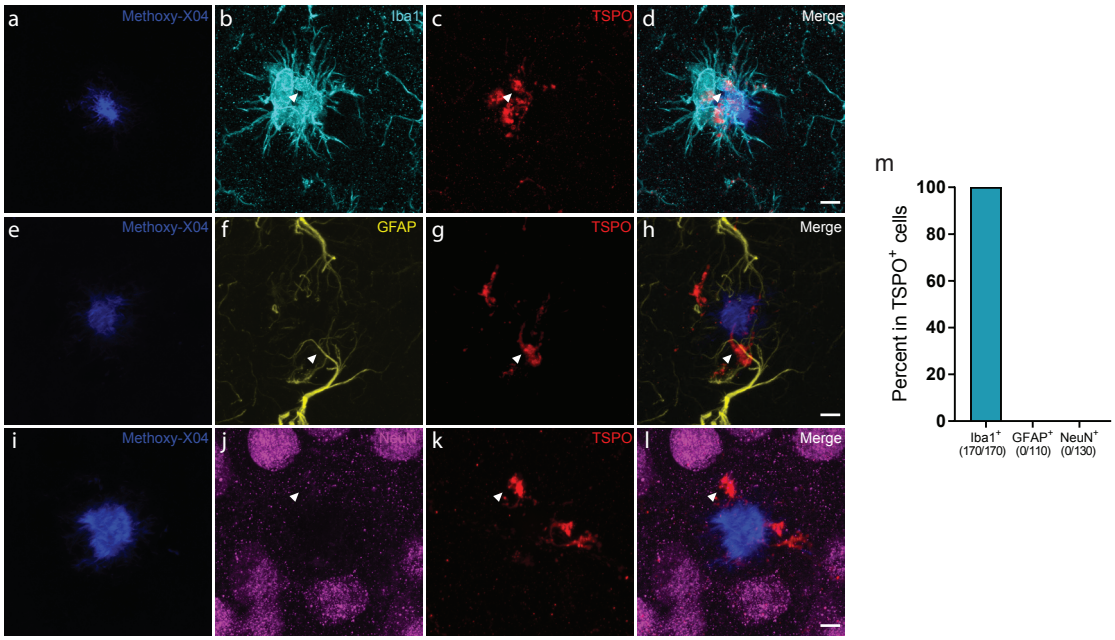

Figure 39. Characterization of TSPO expression in the APPswe/PS1deltaE9 mouse cortex. a-l, Representative confocal micrographs show that around methoxy-X04 stained plaques elevated TSPO mainly colocalized with Iba1$^+$ microglia but not GFAP$^+$ astrocytes, or NeuN$^+$ neurons in the somatosensory cortex in 5-month-old APPswe/PS1deltaE9 mice. **m**, Quantitation of TSPO$^+$ cells colocalized with different cell types. The number of cells counted in each group is indicated below the x-axis. n = 3 animals per group. Scale bar = 20 µm.

3.5.3 TSPO deficiency ameliorates AD-related dendritic spine pathology

To address whether AD-related dendritic spine plasticity is critically influenced by the mitochondrial TSPO, I bred *Tspo* $^{-/-}$ mice to APPswe/PS1deltaE9 x GFP-M mice and performed a 3D analysis of dendritic spines. Spine density was quantified in apical dendritic tufts originating from the layer V pyramidal neurons in proximity to plaques or distant to plaque (<30 µm from plaques, Fig. 40a-g).

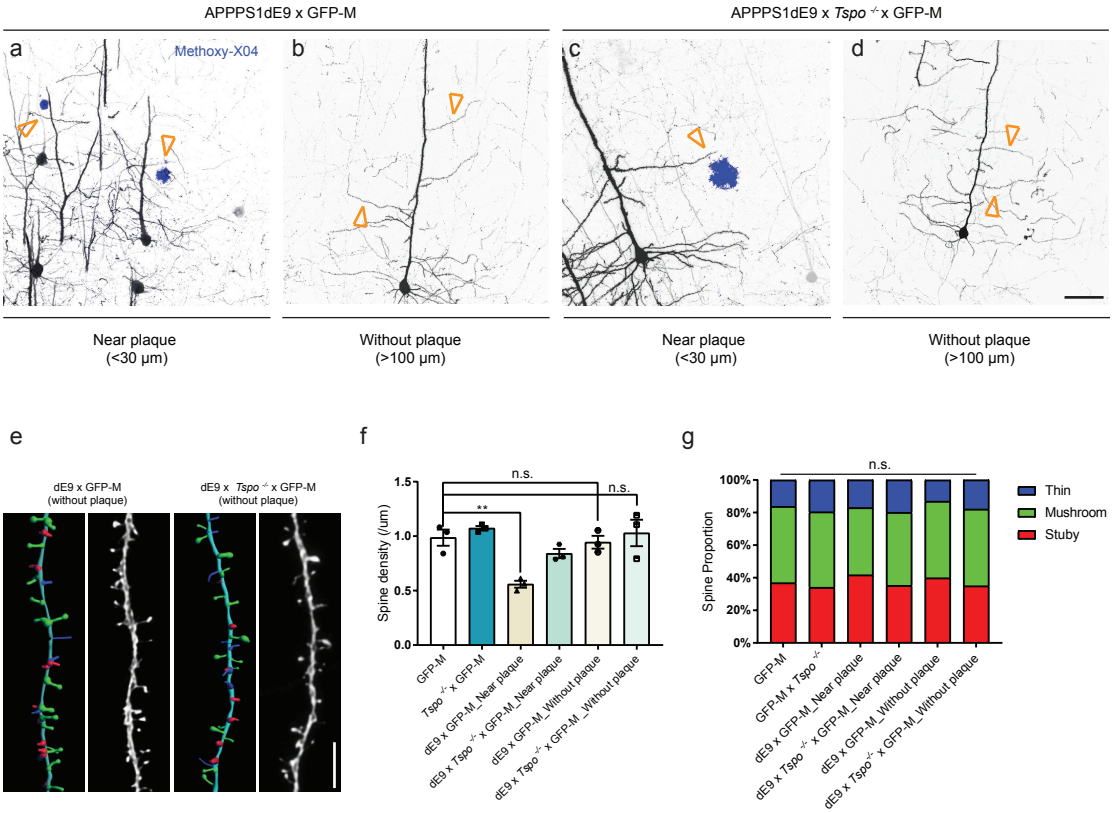

Figure 40. Dendrites at different distances from plaques in APPswe/PS1deltaE9 x GFP-M and APPswe/PS1deltaE9 x *Tspo* $^{-/-}$ x GFP-M mice. **a**-**d**, Representative confocal micrographs showing methoxy-X04 labelled plaques (blue) and eGFP-labelled dendrites (grey). Dendrites localized at regions <30 µm to plaques are classified as "plaque-proximal" dendrites (**a**, **c**) and the ones localized at regions >30 µm to plaques or plaque-free regions are classified as "plaque-distant" dendrites (**b**, **d**). Arrowheads denote the "plaque-proximal" or "plaque-distant" dendrites included in the dendritic spine analysis. **e**-**g**, 3D analysis of dendritic spines in APPswe/PS1deltaE9 x GFP-M and APPswe/PS1deltaE9 x *Tspo* $^{-/-}$ x GFP-M mice. n = 3 animals per group (**f**, **g**). Data are presented as mean ± s.e.m. One-way ANOVA with Bonferroni's post-hoc test (**f**); $\chi 2$ test (**g**). **p*<0.05, ***p*<0.01. n.s – no significant difference. Scale bars: **a**-**d** = 50 µm; **e** = 5 µm.

Compared to GFP-M mice, spine density in apical dendritic tufts originating from the layer V pyramidal neurons in proximity to plaques is significantly reduced in APPswe/PS1deltaE9 x GFP-M mice (Fig. 41a, b), while this reduction in spine density is attenuated in APPswe/PS1deltaE9 x *Tspo* $^{-/-}$ x GFP-M mice (Fig. 41a, b). The loss of spine density in APPswe/PS1deltaE9 x GFP-M mice was associated with a trend decline in mushroom spines, which was not seen in TSPO knockout animals

on the APPswe/PS1deltaE9 background (Fig. 41c). It is notable that the absence of TSPO on the WT background did not affect the spine morphological proportion (Fig. 41c).

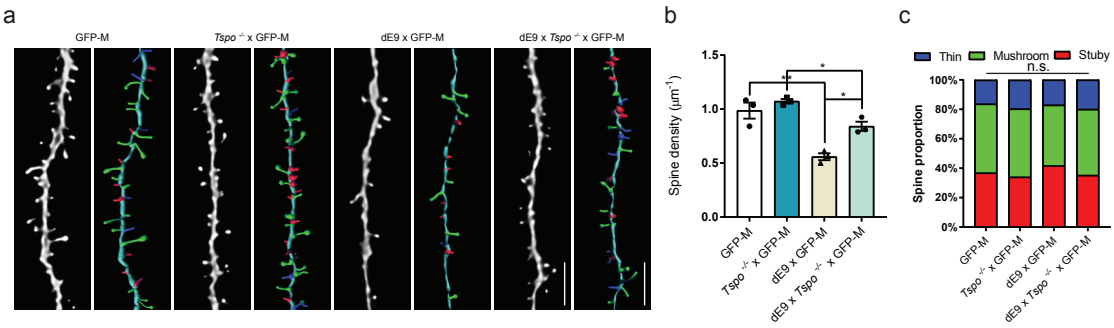

Figure 41. TSPO deficiency ameliorates dendritic spine pathology in AD mouse brain. a-c, 3D analysis of dendritic spines in APPswe/PS1deltaE9 x GFP-M and APPswe/PS1deltaE9 x *Tspo* $^{-/-}$ x GFP-M mice. n = 3 animals per group (**b**, **c**). Data are presented as mean ± s.e.m. One-way ANOVA with Bonferroni's post-hoc test (**b**); χ2 test (**c**). **p*<0.05, ***p*<0.01. n.s. – no significant difference. Scale bar = 5 µm.

3.5.4 Expression of TSPO in the cortex of patients with AD

To illustrate the relevance of the above-described central role of the TSPO in human brain pathology, I evaluated the expression of TSPO in the cortex of patients with AD. TSPO immunohistochemistry on formalin-fixed, free-floating sections from human cortex revealed that in AD brains, TSPO, which co-localizes mainly with the Iba1^{+} microglia (Fig. 42a-d), was markedly increased (Fig. 43a, b, d), while the postsynaptic marker Homer1 expression was reduced (Fig. 43a, c, d).

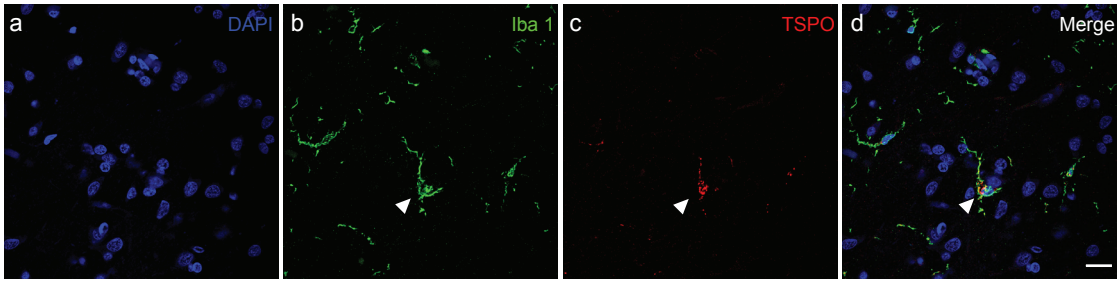

Figure 42. TSPO co-localizes with microglia in AD human brain. a-d, The majority of TSPO-expressing cells are microglia, as shown with Iba1 labelling. Scale bars = 20 µm.

Furthermore, an inverse correlation was found between TSPO and Homer1 levels (Fig. 43e).

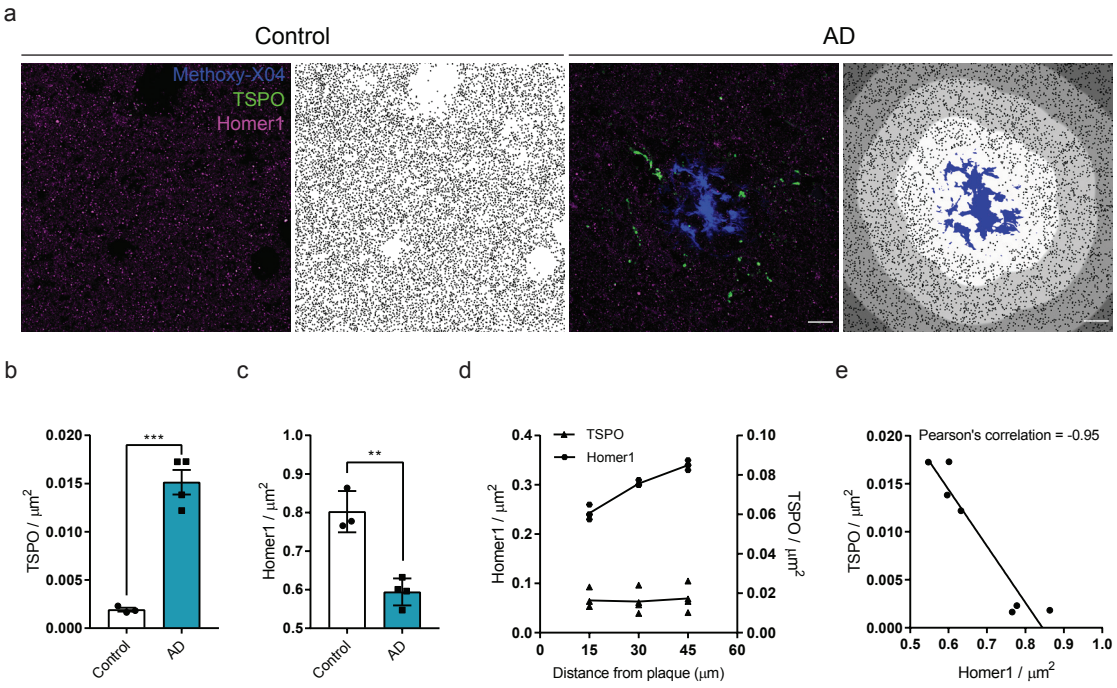

Figure 43. TSPO expression in AD human brain. a, Representative confocal micrographs of methoxy-X04 (blue), TSPO (green), and Homer1 (magenta) in human AD cases and age-matched controls. Homer1$^+$ puncta were automatically detected and binarized. Puncta around plaques are overlaid on a distance transform highlighting the distance from the plaque (blue) in 15 µm wild bins (greyscale). **b** & **c**, Quantifications of TSPO (**b**) and (**c**) Homer1 levels. **d**, Quantification of the densities of Homer1 and TSPO at varying distances from the plaque. **e**, Correlation between TSPO and Homer1 levels. Pearson's correlation = -0.95, significance (two-tailed) p = 0.0009. n = 3 for control cases, n = 4 for AD cases (**b**, **c**, **d**, **e**). Data are presented as mean ± s.e.m. Two-tailed Student's t test (**b**, **c**). $^{**}p<0.01$, $^{***}p<0.001$. Scale bar = 10 µm.

Together, these data indicate that increased TSPO expression in AD brains and mouse models correlates with synaptic loss.

4. Discussion

So far, it remains to be elucidated how the cumulative dose of benzodiazepines can cause cognitive decline and increase the risk of developing dementia such as AD [28,30,33,257]. Here, by showing synaptic deficits in animals after one-week consecutive administration of a sedative dose of diazepam (Fig. 16), I reveal how the benzodiazepine diazepam can cause cognitive decline. Over the past decades, huge progress has been made in comprehending distinct contributions of $GABA_ARs$ subtypes towards various clinical effects [10,11,258], revealing that benzodiazepines exert transient effects on short-term memory via specific $GABA_ARs$ subtypes [9]. Considering their potent and complex pharmacological properties, one would primarily expect a pivotal role of $GABA_ARs$ in diazepam-induced dendritic spine pathology. In contrast, I found that diazepam interferes with dendritic spine plasticity via TSPO without utilizing allosteric modulation at $GABA_ARs$. Upon binding, TSPO drives microglia to deposit C1q and engulf dendritic spines, ultimately leading to a loss of dendritic spines in a process termed synaptic pruning. However, only spines amenable to immediate plasticity are affected by this cascade, whereas stable spines are resistant to these effects. This is consistent with previous clinical studies that memory stored prior to benzodiazepine use is not affected [27] and points towards a physiological role of TSPO-mediated regulation of synaptic plasticity, which is affected by TSPO ligands. Additionally, certain benzodiazepines, most notably clonazepam or alprazolam, bind only weakly to TSPO [53,54]. Based on my findings, a lower risk of dementia would be expected upon the administration of such benzodiazepines. However, for drawing conclusions with regard to the use of benzodiazepines in clinical practice, a systematic screening for the affinity of benzodiazepines to TSPO should be conducted. Notably, although here I observed a critical role of TSPO in the cumulative dose of diazepam-induced synaptic loss, the

role of $GABA_A$Rs in regulating cognitive performance should not be overlooked, especially when considering the complexity of cognition process. For instance, in acutely benzodiazepine treated mice, extrasynaptic α5 $GABA_A$Rs have been implicated in the temporal processing of associative learning via regulating dendritic excitability of hippocampal pyramidal neurons [250], while inverse agonists of α5 $GABA_A$Rs have been developed to enhance cognitive processes [259].

Moreover, the progressive region-specific synaptic loss that precedes neuronal dysfunction and ultimately death functionally correlates with overt memory deficits and cognitive impairment in AD [129]. Here, I show synaptic pathology mediated by increased TSPO in both AD mouse models and patients with AD. Depleting TSPO reduced synaptic loss in an animal model of AD. Moreover, the synaptic loss in diazepam-treated mice occurred in a C1q label-based fashion, which has been observed extensively in AD mouse models [175,260]. Jointly, my results put TSPO as a link between diazepam use and AD pathology. However, ablation of TSPO in APPswe/PS1deltaE9 mice only partially prevented the synaptic loss, indicating that synaptic dysfunction and cognitive decline in AD is multifactorial. For instance, previous studies suggested that α5 $GABA_A$Rs activation suppresses gamma oscillations [261] while restoring the gamma oscillations improves cognition in animal models of AD [262].

Growing evidence points to a key role of microglia in regulating synaptic pruning and function in both physiological and pathological conditions [175,263,264]. Previous studies also demonstrated that TSPO is enriched in microglia compared to other CNS-resident glia and neurons [34]. This is consistent with my data that TSPO-dependent microglial synaptic pruning is crucial for synaptic pathology upon diazepam treatment and in AD. Besides synaptic pruning, a recent study also showed that microglia phagocytic activity is increased when exposed to benzodiazepine [265]. In addition, by depleting microglia, diazepam no longer causes synaptic loss. Thus, my results

strongly point towards microglial TSPO signalling in synaptic pathology. Nevertheless, the contribution of other CNS neurons and glia has yet to be ruled out. This would require the development of new mouse models specifically ablating TSPO in microglia versus other cell types.

Apart from TSPO, other microglia–synapse-associated genes have been studied in disease states. For instance, the gene encoding TREM2, mutations of which are considered as the risk factor for non-FAD, has recently been proved to be essential for microglial synaptic pruning [169]. In addition, genetic depletion of TDP-43, a DNA/RNA binding protein regulating microglial phagocytosis, in APP mutant mice, also leads to significant synapse loss [174]. Here, by demonstrating TSPO-dependent microglial synaptic pruning, I added a new candidate to this group. This further enforces the picture that multiple-gene-related defects in microglial synaptic pruning may constitute the origin of cognitive impairments in a broad range of pathological conditions such as long-term psychotropic drug use (e.g. benzodiazepines), neurodegenerative or psychiatric disorders (e.g. AD). Nevertheless, mechanisms of upstream and downstream TSPO signalling in regulating synaptic pruning remain to be elucidated. For instance, my confocal data provide some evidence that there is a TSPO-mediated upregulation of C1q label-based microglial synaptic pruning upon diazepam treatment. This raises the question of how TSPO signalling interferes with the complement cascade. Moreover, multiple microglial receptors are capable of modulating synaptic pruning. It remains to be determined whether all these receptors regulate synaptic pruning in a similar C1q label-based manner, or through individual pathways of their own.

In conclusion, three points can be made based on these results. First and foremost, TSPO-dependent synaptic pathology is identified as a synaptic mechanism linking the use of benzodiazepine to the increased risk of developing AD in the experimental models, which argues for designing new psychopharmacological drugs with more

beneficial side effect profile. Secondly, the current observations indicate that alterations of TSPO expression are heavily involved in synaptic pathology in AD, suggesting TSPO as a target of interest of novel therapeutic approaches for AD-associated cognitive decline. However, in view of the expression of TSPO also in peripheral tissues, the side effects of TSPO ligands should be carefully evaluated. Finally, TSPO has arisen as an interesting target for developing drugs for psychiatric disorders [34]. For instance, XBD173, a TSPO-selective ligand, exerts robust anxiolytic activity in both animals and humans without causing sedation and withdrawal symptoms [57]. In spite of promising results from the first clinical trials, I observed that activating TSPO by prolonged XBD173 administration causes synaptic loss in mouse models, which calls for caution with regard to the long-term clinical use of TSPO ligands. However, the TSPO ligand etifoxine has been clinically used for a long time in France with no reports on cognitive decline [266].

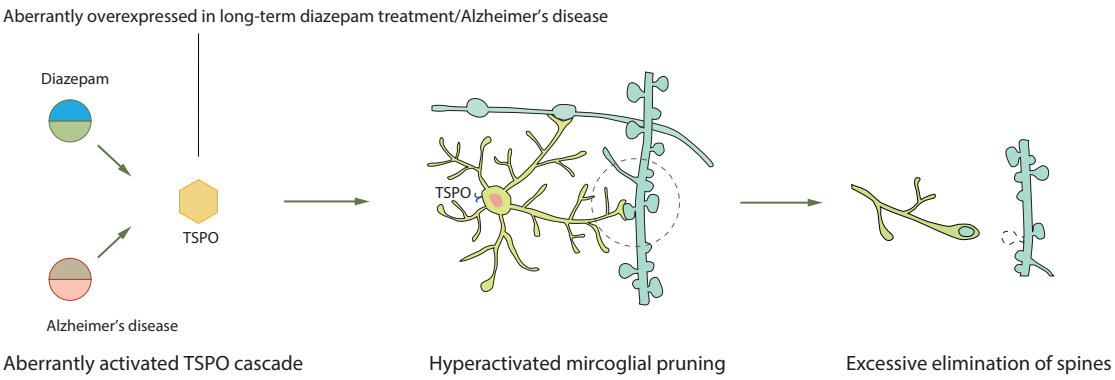

Figure 44. Diagram of the hypothesis. Aberrant upregulation of TSPO occurs upon prolonged diazepam use or in AD pathophysiology. Upon TSPO elevation, dendritic spines are subsequently engulfed by stimulated microglia, resulting in the excessive elimination of spines, which thereby contributes to synapse loss and cognitive impairment.

Overall, this study demonstrates the disruptive role of TSPO on synaptic plasticity and provides first avenues for targeting microglial synapse loss not only for the design of new drugs which may avoid cognitive decline but also for therapy and prevention for cognitive decline in AD, which need to be confirmed in clinical studies.

List of Figures and Tables

Bibliography

1 López-Muñoz, F., Álamo, C. & García-García, P. The discovery of chlordiazepoxide and the clinical introduction of benzodiazepines: half a century of anxiolytic drugs. *Journal of Anxiety Disorders* **25**, 554-562 (2011).

2 Hall, R. & Zisook, S. Paradoxical reactions to benzodiazepines. *British Journal of Clinical Pharmacology* **11**, 99S-104S (1981).

3 Archer, G. A. & Sternbach, L. H. Chemistry of benzodiazepines. *Chemical Reviews* **68**, 747-784 (1968).

4 Gerecke, M. Chemical structure and properties of midazolam compared with other benzodiazepines. *British Journal of Clinical Pharmacology* **16**, 11S-16S (1983).

5 Rudolph, U. & Knoflach, F. Beyond classical benzodiazepines: novel therapeutic potential of $GABA_A$ receptor subtypes. *Nature Reviews Drug Discovery* **10**, 685 (2011).

6 Batlle, E., Lizano, E., Viñas, M. & Pujol, M. D. in *Medicinal Chemistry* (IntechOpen, 2018).

7 Mody, I., De Koninck, Y., Otis, T. S. & Soltesz, I. Bridging the cleft at GABA synapses in the brain. *Trends in Neurosciences* **17**, 517-525 (1994).

8 Möhler, H. The rise of a new GABA pharmacology. *Neuropharmacology* **60**, 1042-1049 (2011).

9 Rudolph, U. *et al.* Benzodiazepine actions mediated by specific γ-aminobutyric $acid_A$ receptor subtypes. *Nature* **401**, 796 (1999).

10 McKernan, R. *et al.* Sedative but not anxiolytic properties of benzodiazepines are mediated by the $GABA_A$ receptor α_1 subtype. *Nature Neuroscience* **3**, 587 (2000).

11 Ralvenius, W. T., Benke, D., Acuna, M. A., Rudolph, U. & Zeilhofer, H. U. Analgesia and unwanted benzodiazepine effects in point-mutated mice expressing only one benzodiazepine-sensitive $GABA_A$ receptor subtype. *Nature Communications* **6**, 6803 (2015).

12 Lader, M. Benzodiazepines revisited—will we ever learn? *Addiction* **106**, 2086-2109 (2011).

13 Pakes, G., Brogden, R., Heel, R., Speight, T. & Avery, G. Triazolam: a review of its pharmacological properties and therapeutic efficacy in patients with insomnia. *Drugs* **22**, 81-110 (1981).

14 Morgan, K., Adam, K. & Oswald, I. Effects of loprazolam and of triazolam on psychological functions. *Psychopharmacology* **82**, 386-388 (1984).

15 Briggs, R., Castleden, C. & Kraft, C. Improved hypnotic treatment using chlormethiazole and temazepam. *British Medical Journal* **280**, 601-604 (1980).

16 Ashton, H. Guidelines for the rational use of benzodiazepines. *Drugs* **48**, 25-40 (1994).

17 Dawson, G., Jue, S. & Brogden, R. Alprazolam: a review of its pharmacodynamic properties and efficacy in the treatment of anxiety and depression. *Drugs* **27**, 132-147 (1984).

18 Riss, J., Cloyd, J., Gates, J. & Collins, S. Benzodiazepines in epilepsy: pharmacology and pharmacokinetics. *Acta Neurologica Scandinavica* **118**, 69-86 (2008).

19 Kleinknecht, R. A. & Donaldson, D. A review of the effects of diazepam on cognitive and psychomotor performance. *Journal of Nervous and Mental Disease* (1975).

20 Medicines, C. O. T. R. O. Systematic review of the benzodiazepines: guidelines for data sheets on diazepam, chlordiazepoxide, medazepam, clorazepate, lorazepam, oxazepam, temazepam, triazolam, nitrazepam, and flurazepam. *British Medical Journal*, 910-912 (1980).

21 Romach, M., Busto, U., Somer, G., Kaplan, H. L. & Sellers, E. Clinical aspects of chronic use of alprazolam and lorazepam. *The American Journal of Psychiatry* **152**, 1161-1167 (1995).

22 Nordt, S. P. & Clark, R. F. Midazolam: a review of therapeutic uses and toxicity. *The Journal of Emergency Medicine* **15**, 357-365 (1997).

23 Pat McAndrews, M. *et al.* Cognitive effects of long-term benzodiazepine use in older adults. *Human Psychopharmacology: Clinical and Experimental* **18**, 51-57 (2003).

24 Arolfo, M. P. & Brioni, J. D. Diazepam impairs place learning in the Morris water maze. *Behavioral and Neural Biology* **55**, 131-136 (1991).

25 Golombok, S., Moodley, P. & Lader, M. Cognitive impairment in long-term benzodiazepine users. *Psychological Medicine* **18**, 365-374 (1988).

26 Stewart, S. A. The effects of benzodiazepines on cognition. *The Journal of Clinical Psychiatry* (2005).

27 Mejo, S. L. Anterograde amnesia linked to benzodiazepines. *The Nurse Practitioner* **17**, 44, 49-50 (1992).

28 De Gage, S. B. *et al.* Benzodiazepine use and risk of Alzheimer's disease: case-control study. *BMJ* **349**, g5205 (2014).

29 Gallacher, J. *et al.* Benzodiazepine use and risk of dementia: evidence from the Caerphilly Prospective Study (CaPS). *Journal of Epidemiology and Community Health* **66**, 869-873 (2012).

30 Penninkilampi, R. & Eslick, G. D. A systematic review and meta-analysis of the risk of dementia associated with benzodiazepine use, after controlling for protopathic bias. *CNS Drugs* **32**, 485-497 (2018).

31 Gray, S. L. *et al.* Benzodiazepine use and risk of incident dementia or cognitive decline: prospective population based study. *BMJ* **352**, i90 (2016).

32 Picton, J. D., Marino, A. B. & Nealy, K. L. Benzodiazepine use and cognitive decline in the elderly. *The Bulletin of the American Society of Hospital Pharmacists* **75**, e6-e12 (2018).

33 Zhang, Y., Zhou, X.-h., Meranus, D. H., Wang, L. & Kukull, W. A. Benzodiazepine use and cognitive decline in elderly with normal cognition. *Alzheimer Disease and Associated Disorders* **30**, 113 (2016).

34 Rupprecht, R. *et al.* Translocator protein (18 kDa)(TSPO) as a therapeutic target for neurological and psychiatric disorders. *Nature Reviews Drug Discovery* **9**, 971 (2010).

35 Papadopoulos, V. *et al.* Translocator protein (18 kDa): new nomenclature for the peripheral-type benzodiazepine receptor based on its structure and molecular function. *Trends in Pharmacological Sciences* **27**, 402-409 (2006).

36 Joseph-Liauzun, E., Delmas, P., Shire, D. & Ferrara, P. Topological analysis of the peripheral benzodiazepine receptor in yeast mitochondrial membranes supports a five-transmembrane structure. *Journal of Biological Chemistry* **273**, 2146-2152 (1998).

37 McEnery, M. W., Snowman, A. M., Trifiletti, R. R. & Snyder, S. H. Isolation of the mitochondrial benzodiazepine receptor: association with the voltage-dependent anion channel and the adenine nucleotide carrier. *Proceedings of the National Academy of Sciences* **89**, 3170-3174 (1992).

38 Garnier, M. *et al. In vitro* reconstitution of a functional peripheral-type benzodiazepine receptor from mouse Leydig tumor cells. *Molecular Pharmacology* **45**, 201-211 (1994).

39 Veenman, L., Shandalov, Y. & Gavish, M. VDAC activation by the 18 kDa translocator protein (TSPO), implications for apoptosis. *Journal of Bioenergetics and Biomembranes* **40**, 199-205 (2008).

40 Gut, P., Zweckstetter, M. & Banati, R. B. Lost in translocation: the functions of the 18-kD translocator protein. *Trends in Endocrinology & Metabolism* **26**, 349-356 (2015).

41 Park, C. H., Carboni, E., Wood, P. L. & Gee, K. W. Characterization of peripheral benzodiazepine type sites in a cultured murine BV-2 microglial cell line. *Glia* **16**, 65-70 (1996).

42 Itzhak, Y., Baker, L. & Norenberg, M. D. Characterization of the peripheral-type benzodiazepine receptors in cultured astrocytes: evidence for multiplicity. *Glia* **9**, 211-218 (1993).

43 Anholt, R., Murphy, K., Mack, G. E. & Snyder, S. H. Peripheral-type benzodiazepine receptors in the central nervous system: localization to olfactory nerves. *Journal of Neuroscience* **4**, 593-603 (1984).

44 Casellas, P., Galiegue, S. & Basile, A. S. Peripheral benzodiazepine receptors and mitochondrial function. *Neurochemistry International* **40**, 475-486 (2002).

45 Sprengel, R. *et al.* Molecular cloning and expression of cDNA encoding a peripheral-type benzodiazepine receptor. *Journal of Biological Chemistry* **264**, 20415-20421 (1989).

46 Parola, A. L. *et al.* Cloning and expression of a pharmacologically unique bovine peripheral-type benzodiazepine receptor isoquinoline binding protein. *Journal of Biological Chemistry* **266**, 14082-14087 (1991).

47 RIOND, J. *et al.* Molecular cloning and chromosomal localization of a human peripheral-type benzodiazepine receptor. *European Journal of Biochemistry* **195**, 305-311 (1991).

48 Besman, M. J. *et al.* Identification of des-(Gly-Ile)-endozepine as an effector of corticotropin-dependent adrenal steroidogenesis: stimulation of cholesterol delivery is mediated by the peripheral benzodiazepine receptor. *Proceedings of the National Academy of Sciences* **86**, 4897-4901 (1989).

49 Lacapere, J.-J. & Papadopoulos, V. Peripheral-type benzodiazepine receptor: structure and function of a cholesterol-binding protein in steroid and bile acid biosynthesis. *Steroids* **68**, 569-585 (2003).

50 Liu, G.-J. *et al.* Functional gains in energy and cell metabolism after TSPO gene insertion. *Cell Cycle* **16**, 436-447 (2017).

51 Milenkovic, V. M. *et al.* CRISPR-Cas9 Mediated TSPO Gene Knockout alters Respiration and Cellular Metabolism in Human Primary Microglia Cells. *International Journal of Molecular Sciences* **20**, 3359 (2019).

52 Gatliff, J. *et al.* A role for TSPO in mitochondrial Ca^{2+} homeostasis and redox stress signaling. *Cell Death & Disease* **8**, e2896 (2017).

53 McCauley, L. D. *et al.* Benzodiazepines and peptides stimulate pregnenolone synthesis in brain mitochondria. *European Journal of Pharmacology* **276**, 145-153 (1995).

54 Schmoutz, C. D., Guerin, G. F. & Goeders, N. E. Role of GABA-active neurosteroids in the efficacy of metyrapone against cocaine addiction. *Behavioural Brain Research* **271**, 269-276 (2014).

55 Le Fur, G. *et al.* Peripheral benzodiazepine binding sites: effect of PK 11195, 1-(2-chlorophenyl)-N-methyl-N-(1-methylpropyl)-3-isoquinolinecarboxamide: I. *In vitro* studies. *Life Sciences* **32**, 1839-1847 (1983).

56 Le Fur, G. *et al.* Peripheral benzodiazepine binding sites: effect of PK 11195, 1-(2-chlorophenyl)-N-methyl-(1-methylpropyl)-3 isoquinolinecarboxamide: II. *In vivo* studies. *Life Sciences* **32**, 1849-1856 (1983).

57 Rupprecht, R. *et al.* Translocator protein (18 kD) as target for anxiolytics without benzodiazepine-like side effects. *Science* **325**, 490-493 (2009).

58 Guidotti, A. *et al.* Isolation, characterization, and purification to homogeneity of an endogenous polypeptide with agonistic action on benzodiazepine receptors. *Proceedings of the National Academy of Sciences* **80**, 3531-3535 (1983).

59 Mills, C. D., Bitler, J. L. & Woolf, C. J. Role of the peripheral benzodiazepine receptor in sensory neuron regeneration. *Molecular and Cellular Neuroscience* **30**, 228-237 (2005).

60 Romeo, E. *et al.* Stimulation of brain steroidogenesis by 2-aryl-indole-3-acetamide derivatives acting at the mitochondrial diazepam-binding inhibitor receptor complex. *Journal of Pharmacology and Experimental Therapeutics* **267**, 462-471 (1993).

61 Veiga, S., Carrero, P., Pernia, O., Azcoitia, I. & Garcia-Segura, L. M. Translocator protein (18 kDa) is involved in the regulation of reactive gliosis. *Glia* **55**, 1426-1436 (2007).

62 Veiga, S., Azcoitia, I. & Garcia-Segura, L. M. Ro5-4864, a peripheral benzodiazepine receptor ligand, reduces reactive gliosis and protects hippocampal hilar neurons from kainic acid excitotoxicity. *Journal of Neuroscience Research* **80**, 129-137 (2005).

63 Girard, C. *et al.* Etifoxine improves peripheral nerve regeneration and functional recovery. *Proceedings of the National Academy of Sciences* **105**, 20505-20510 (2008).

64 Verleye, M. *et al.* The anxiolytic etifoxine activates the peripheral benzodiazepine receptor and increases the neurosteroid levels in rat brain. *Pharmacology Biochemistry and Behavior* **82**, 712-720 (2005).

65 Lavisse, S. *et al.* Reactive astrocytes overexpress TSPO and are detected by TSPO positron emission tomography imaging. *Journal of Neuroscience* **32**, 10809-10818 (2012).

66 Charbonneau, P. *et al.* Peripheral-type benzodiazepine receptors in the living heart characterized by positron emission tomography. *Circulation* **73**, 476-483 (1986).

67 Cagnin, A. *et al.* In-vivo measurement of activated microglia in dementia. *The Lancet* **358**, 461-467 (2001).

68 Gerhard, A. *et al. In vivo* imaging of microglial activation with [^{11}C](R)-PK11195 PET in idiopathic Parkinson's disease. *Neurobiology of Disease* **21**, 404-412 (2006).

69 Bloomfield, P. S. *et al.* Microglial activity in people at ultra high risk of psychosis and in schizophrenia: an [^{11}C] PBR28 PET brain imaging study. *The American Journal of Psychiatry* **173**, 44-52 (2015).

70 Simmons, D. A. *et al.* TSPO–PET imaging using [^{18}F] PBR06 is a potential translatable biomarker for treatment response in Huntington's disease: preclinical evidence with the p75^{NTR} ligand LM11A-31. *Human Molecular Genetics* **27**, 2893-2912 (2018).

71 Yui, J. *et al.* Visualization of early infarction in rat brain after ischemia using a translocator protein (18 kDa) PET ligand [^{11}C] DAC with ultra-high specific activity. *Neuroimage* **54**, 123-130 (2011).

72 Chauveau, F. *et al.* Comparative evaluation of the translocator protein radioligands ^{11}C-DPA-713, ^{18}F-DPA-714, and ^{11}C-PK11195 in a rat model of acute neuroinflammation. *Journal of Nuclear Medicine* **50**, 468-476 (2009).

73 Ikawa, M. *et al.* ^{11}C-ER176, a radioligand for 18-kDa translocator protein, has adequate sensitivity to robustly image all three affinity genotypes in human brain. *Journal of Nuclear Medicine* **58**, 320-325 (2017).

74 Fan, Z. *et al.* Flutriciclamide (^{18}F-GE180) PET: first-in-human PET study of novel third-generation *in vivo* marker of human translocator protein. *Journal of Nuclear Medicine* **57**, 1753-1759 (2016).

75 Owen, D., Guo, Q., Rabiner, E. & Gunn, R. The impact of the rs6971 polymorphism in TSPO for quantification and study design. *Clinical and Translational Imaging* **3**, 417-422 (2015).

76 Dugger, B. N. & Dickson, D. W. Pathology of neurodegenerative diseases. *Cold Spring Harbor Perspectives in Biology* **9**, a028035 (2017).

77 Serrano-Pozo, A., Frosch, M. P., Masliah, E. & Hyman, B. T. Neuropathological alterations in Alzheimer disease. *Cold Spring Harbor Perspectives in Medicine* **1**, a006189 (2011).

78 Saunders, A. M. *et al.* Association of apolipoprotein E allele ϵ4 with late-onset familial and sporadic Alzheimer's disease. *Neurology* **43**, 1467-1467 (1993).

79 Berchtold, N. C. & Cotman, C. W. Evolution in the conceptualization of dementia and Alzheimer's disease: Greco-Roman period to the 1960s. *Neurobiology of Aging* **19**, 173-189 (1998).

80 Alzheimer, A. Über eine eigenartige Erkrankung der Hirnrinde. *Allgemeine Zeitschrift fur Psychiatrie und Psychisch-gerichtliche Medizin* **64**, 146-148 (1907).

81 Bick, K., Amaducci, L. & Pepeu, G. *The Early Story of Alzheimer's Disease: Translation of the Historical Papers by Alois Alzheimer, Oskar Fischer, Francesco Bonfiglio, Emil Kraepelin, Gaetano Perusini*. (Liviana Press, 1987).

82 Ferri, C. P. *et al.* Global prevalence of dementia: a Delphi consensus study. *The Lancet* **366**, 2112-2117 (2005).

83 Wimo, A., Winblad, B., Aguero-Torres, H. & von Strauss, E. The magnitude of dementia occurrence in the world. *Alzheimer Disease & Associated Disorders* **17**, 63-67 (2003).

84 Reitz, C., Brayne, C. & Mayeux, R. Epidemiology of Alzheimer disease. *Nature Reviews Neurology* **7**, 137 (2011).

85 Hebert, L. E., Scherr, P. A., Bienias, J. L., Bennett, D. A. & Evans, D. A. Alzheimer disease in the US population: prevalence estimates using the 2000 census. *Archives of Neurology* **60**, 1119-1122 (2003).

86 Sperling, R. A. *et al.* Toward defining the preclinical stages of Alzheimer's disease: Recommendations from the National Institute on Aging-Alzheimer's Association workgroups on diagnostic guidelines for Alzheimer's disease. *Alzheimer's & Dementia* **7**, 280-292 (2011).

87 Pimplikar, S. W., Nixon, R. A., Robakis, N. K., Shen, J. & Tsai, L.-H. Amyloid-independent mechanisms in Alzheimer's disease pathogenesis. *Journal of Neuroscience* **30**, 14946-14954 (2010).

88 Herrup, K. Reimagining Alzheimer's disease—an age-based hypothesis. *Journal of Neuroscience* **30**, 16755-16762 (2010).

89 Ossenkoppele, R. *et al.* Prevalence of amyloid PET positivity in dementia syndromes: a meta-analysis. *JAMA* **313**, 1939-1950 (2015).

90 Gonneaud, J. *et al.* Relative effect of APOE ε4 on neuroimaging biomarker changes across the lifespan. *Neurology* **87**, 1696-1703 (2016).

91 Lee, C. D., Tse, W., Smith, J. D. & Landreth, G. E. Apolipoprotein E promotes β-amyloid trafficking and degradation by modulating microglial cholesterol levels. *Journal of Biological Chemistry* **287**, 2032-2044 (2012).

92 Jack Jr, C. R. *et al.* NIA-AA Research Framework: Toward a biological definition of Alzheimer's disease. *Alzheimer's & Dementia* **14**, 535-562 (2018).

93 Visser, P. J. *et al.* Prevalence and prognostic value of CSF markers of Alzheimer's disease pathology in patients with subjective cognitive impairment or mild cognitive impairment in the DESCRIPA study: a prospective cohort study. *The Lancet Neurology* **8**, 619-627 (2009).

94 Buerger, K. *et al.* CSF phosphorylated tau protein correlates with neocortical neurofibrillary pathology in Alzheimer's disease. *Brain* **129**, 3035-3041 (2006).

95 Besson, F. L. *et al.* Cognitive and brain profiles associated with current neuroimaging biomarkers of preclinical Alzheimer's disease. *Journal of Neuroscience* **35**, 10402-10411 (2015).

96 Mita, S., Schon, E. & Herbert, J. Widespread expression of amyloid beta-protein precursor gene in rat brain. *The American Journal of Pathology* **134**, 1253 (1989).

97 Priller, C. *et al.* Synapse formation and function is modulated by the amyloid precursor protein. *Journal of Neuroscience* **26**, 7212-7221 (2006).

98 Zou, C. *et al.* Intraneuronal APP and extracellular Aβ independently cause dendritic spine pathology in transgenic mouse models of Alzheimer's disease. *Acta Neuropathologica* **129**, 909-920 (2015).

99 Tyan, S.-H. *et al.* Amyloid precursor protein (APP) regulates synaptic structure and function. *Molecular and Cellular Neuroscience* **51**, 43-52 (2012).

100 Turner, P. R., O'Connor, K., Tate, W. P. & Abraham, W. C. Roles of amyloid precursor protein and its fragments in regulating neural activity, plasticity and memory. *Progress in Neurobiology* **70**, 1-32 (2003).

101 Nicolas, M. & Hassan, B. A. Amyloid precursor protein and neural development. *Development* **141**, 2543-2548 (2014).

102 Freude, K. K., Penjwini, M., Davis, J. L., LaFerla, F. M. & Blurton-Jones, M. Soluble amyloid precursor protein induces rapid neural differentiation of

human embryonic stem cells. *Journal of Biological Chemistry* **286**, 24264-24274 (2011).

103 Schmidt, C. *et al.* Amyloid precursor protein and amyloid β-peptide bind to ATP synthase and regulate its activity at the surface of neural cells. *Molecular Psychiatry* **13**, 953 (2008).

104 Anandatheerthavarada, H. K., Biswas, G., Robin, M.-A. & Avadhani, N. G. Mitochondrial targeting and a novel transmembrane arrest of Alzheimer's amyloid precursor protein impairs mitochondrial function in neuronal cells. *The Journal of Cell Biology* **161**, 41-54 (2003).

105 Coulson, E., Paliga, K., Beyreuther, K. & Masters, C. What the evolution of the amyloid protein precursor supergene family tells us about its function. *Neurochemistry International* **36**, 175-184 (2000).

106 Wasco, W. *et al.* Identification of a mouse brain cDNA that encodes a protein related to the Alzheimer disease-associated amyloid beta protein precursor. *Proceedings of the National Academy of Sciences* **89**, 10758-10762 (1992).

107 Wasco, W. *et al.* Isolation and characterization of APLP2 encoding a homologue of the Alzheimer's associated amyloid β protein precursor. *Nature Genetics* **5**, 95 (1993).

108 Kang, J. *et al.* The precursor of Alzheimer's disease amyloid A4 protein resembles a cell-surface receptor. *Nature* **325**, 733 (1987).

109 Dyrks, T. *et al.* Identification, transmembrane orientation and biogenesis of the amyloid A4 precursor of Alzheimer's disease. *The EMBO Journal* **7**, 949-957 (1988).

110 Walsh, D. M. *et al.* γ-Secretase cleavage and binding to FE65 regulate the nuclear translocation of the intracellular C-terminal domain (ICD) of the APP family of proteins. *Biochemistry* **42**, 6664-6673 (2003).

111 Eggert, S. *et al.* The Proteolytic Processing of the Amyloid Precursor Protein Gene Family Members APLP-1 and APLP-2 Involves α-, β-, γ-, and ϵ-Like Cleavages MODULATION OF APLP-1 PROCESSING BY N-GLYCOSYLATION. *Journal of Biological Chemistry* **279**, 18146-18156 (2004).

112 Vassar, R. *et al.* β-Secretase cleavage of Alzheimer's amyloid precursor protein by the transmembrane aspartic protease BACE. *Science* **286**, 735-741 (1999).

113 Haass, C. *et al.* Amyloid β-peptide is produced by cultured cells during normal metabolism. *Nature* **359**, 322 (1992).

114 Lammich, S. *et al.* Constitutive and regulated α-secretase cleavage of Alzheimer's amyloid precursor protein by a disintegrin metalloprotease. *Proceedings of the National Academy of Sciences* **96**, 3922-3927 (1999).

115 Haass, C., Kaether, C., Thinakaran, G. & Sisodia, S. Trafficking and proteolytic processing of APP. *Cold Spring Harbor Perspectives in Medicine* **2**, a006270 (2012).

116 Pimplikar, S. W. Reassessing the amyloid cascade hypothesis of Alzheimer's disease. *The International Journal of Biochemistry & Cell Biology* **41**, 1261-1268 (2009).

117 Tanzi, R. E. & Bertram, L. Twenty years of the Alzheimer's disease amyloid hypothesis: a genetic perspective. *Cell* **120**, 545-555 (2005).

118 Hardy, J. A. & Higgins, G. A. Alzheimer's disease: the amyloid cascade hypothesis. *Science* **256**, 184-186 (1992).

119 Selkoe, D. J. & Hardy, J. The amyloid hypothesis of Alzheimer's disease at 25 years. *EMBO Molecular Medicine* **8**, 595-608 (2016).

120 De Strooper, B. & Karran, E. The cellular phase of Alzheimer's disease. *Cell* **164**, 603-615 (2016).

121 Selkoe, D. J. Toward a comprehensive theory for Alzheimer's disease. Hypothesis: Alzheimer's disease is caused by the cerebral accumulation and cytotoxicity of amyloid β-protein. *Annals of the New York Academy of Sciences* **924**, 17-25 (2000).

122 Glenner, G. G. & Wong, C. W. Alzheimer's disease: initial report of the purification and characterization of a novel cerebrovascular amyloid protein. *Biochemical and Biophysical Research Communications* **120**, 885-890 (1984).

123 Glenner, G. G. & Wong, C. W. Alzheimer's disease and Down's syndrome: sharing of a unique cerebrovascular amyloid fibril protein. *Biochemical and Biophysical Research Communications* **122**, 1131-1135 (1984).

124 Hardy, J. & Selkoe, D. J. The amyloid hypothesis of Alzheimer's disease: progress and problems on the road to therapeutics. *Science* **297**, 353-356 (2002).

125 Chen, X., Reichert, M. C. & Gan, L. in *Genes, Environment and Alzheimer's Disease* 135-167 (Elsevier, 2016).

126 West, M. J., Coleman, P. D., Flood, D. G. & Troncoso, J. C. Differences in the pattern of hippocampal neuronal loss in normal ageing and Alzheimer's disease. *The Lancet* **344**, 769-772 (1994).

127 Terry, R. D. *et al.* Physical basis of cognitive alterations in Alzheimer's disease: synapse loss is the major correlate of cognitive impairment. *Annals of Neurology* **30**, 572-580 (1991).

128 Arendt, T. Synaptic degeneration in Alzheimer's disease. *Acta Neuropathologica* **118**, 167-179 (2009).

129 Mucke, L. & Selkoe, D. J. Neurotoxicity of amyloid β-protein: synaptic and network dysfunction. *Cold Spring Harbor Perspectives in Medicine* **2**, a006338 (2012).

130 Hsia, A. Y. *et al.* Plaque-independent disruption of neural circuits in Alzheimer's disease mouse models. *Proceedings of the National Academy of Sciences* **96**, 3228-3233 (1999).

131 Mucke, L. *et al.* High-level neuronal expression of $A\beta_{1-42}$ in wild-type human amyloid protein precursor transgenic mice: synaptotoxicity without plaque formation. *Journal of Neuroscience* **20**, 4050-4058 (2000).

132 Hormuzdi, S. G., Filippov, M. A., Mitropoulou, G., Monyer, H. & Bruzzone, R. Electrical synapses: a dynamic signaling system that shapes the activity of neuronal networks. *Biochimica et Biophysica Acta (BBA)-Biomembranes* **1662**, 113-137 (2004).

133 Miller, A. C. *et al.* A genetic basis for molecular asymmetry at vertebrate electrical synapses. *eLife* **6**, e25364 (2017).

134 Hall, Z. W. & Sanes, J. R. Synaptic structure and development: the neuromuscular junction. *Cell* **72**, 99-121 (1993).

135 Garner, C. C., Nash, J. & Huganir, R. L. PDZ domains in synapse assembly and signalling. *Trends in Cell Biology* **10**, 274-280 (2000).

136 Matteoli, M. *et al.* Differential effect of alpha-latrotoxin on exocytosis from small synaptic vesicles and from large dense-core vesicles containing calcitonin gene-related peptide at the frog neuromuscular junction. *Proceedings of the National Academy of Sciences* **85**, 7366-7370 (1988).

137 Unwin, N. Neurotransmitter action: opening of ligand-gated ion channels. *Cell* **72**, 31-41 (1993).

138 Kelly, R. B. Storage and release of neurotransmitters. *Cell* **72**, 43-53 (1993).

139 Crick, F. Do dendritic spines twitch? *Trends in Neurosciences* **5**, 44-46 (1982).

140 García-López, P., García-Marín, V. & Freire, M. The discovery of dendritic spines by Cajal in 1888 and its relevance in the present neuroscience. *Progress in Neurobiology* **83**, 110-130 (2007).

141 Glickstein, M. Golgi and Cajal: The neuron doctrine and the 100th anniversary of the 1906 Nobel Prize. *Current Biology* **16**, R147-R151 (2006).

142 Kasai, H., Fukuda, M., Watanabe, S., Hayashi-Takagi, A. & Noguchi, J. Structural dynamics of dendritic spines in memory and cognition. *Trends in Neurosciences* **33**, 121-129 (2010).

143 Nimchinsky, E. A., Sabatini, B. L. & Svoboda, K. Structure and function of dendritic spines. *Annual Review of Physiology* **64**, 313-353 (2002).

144 Nishiyama, J. & Yasuda, R. Biochemical computation for spine structural plasticity. *Neuron* **87**, 63-75 (2015).

145 Bloodgood, B. L. & Sabatini, B. L. Neuronal activity regulates diffusion across the neck of dendritic spines. *Science* **310**, 866-869 (2005).

146 Grunditz, Å., Holbro, N., Tian, L., Zuo, Y. & Oertner, T. G. Spine neck plasticity controls postsynaptic calcium signals through electrical compartmentalization. *Journal of Neuroscience* **28**, 13457-13466 (2008).

147 Müller, W. & Connor, J. A. Dendritic spines as individual neuronal compartments for synaptic Ca^{2+} responses. *Nature* **354**, 73 (1991).

148 Harnett, M. T., Makara, J. K., Spruston, N., Kath, W. L. & Magee, J. C. Synaptic amplification by dendritic spines enhances input cooperativity. *Nature* **491**, 599 (2012).

149 Ziff, E. B. Enlightening the postsynaptic density. *Neuron* **19**, 1163-1174 (1997).

150 Hering, H. & Sheng, M. Dentritic spines: structure, dynamics and regulation. *Nature Reviews Neuroscience* **2**, 880 (2001).

151 Husi, H., Ward, M. A., Choudhary, J. S., Blackstock, W. P. & Grant, S. G. Proteomic analysis of NMDA receptor–adhesion protein signaling complexes. *Nature Neuroscience* **3**, 661 (2000).

152 Kennedy, M. B. Signal-processing machines at the postsynaptic density. *Science* **290**, 750-754 (2000).

153 Spacek, J. & Harris, K. M. Three-dimensional organization of smooth endoplasmic reticulum in hippocampal CA1 dendrites and dendritic spines of the immature and mature rat. *Journal of Neuroscience* **17**, 190-203 (1997).

154 Andrews, S. B., Leapman, R. D., Landis, D. & Reese, T. S. Activity-dependent accumulation of calcium in Purkinje cell dendritic spines. *Proceedings of the National Academy of Sciences* **85**, 1682-1685 (1988).

155 Rose, C. R. & Konnerth, A. Stores not just for storage: intracellular calcium release and synaptic plasticity. *Neuron* **31**, 519-522 (2001).

156 Verkhratsky, A. Physiology and pathophysiology of the calcium store in the endoplasmic reticulum of neurons. *Physiological Reviews* **85**, 201-279 (2005).

157 Fischer, M., Kaech, S., Knutti, D. & Matus, A. Rapid actin-based plasticity in dendritic spines. *Neuron* **20**, 847-854 (1998).

158 Matus, A. Actin-based plasticity in dendritic spines. *Science* **290**, 754-758 (2000).

159 Steward, O. & Levy, W. B. Preferential localization of polyribosomes under the base of dendritic spines in granule cells of the dentate gyrus. *Journal of Neuroscience* **2**, 284-291 (1982).

160 Spacek, J. Three-dimensional analysis of dendritic spines. II. Spine apparatus and other cytoplasmic components. *Anatomy and Embryology* **171**, 235-243 (1985).

161 Tang, S. J. & Schuman, E. M. Protein synthesis in the dendrite. *Philosophical Transactions of the Royal Society of London. Series B: Biological Sciences* **357**, 521-529 (2002).

162 Nithianantharajah, J. & Hannan, A. J. Enriched environments, experience-dependent plasticity and disorders of the nervous system. *Nature Reviews Neuroscience* **7**, 697 (2006).

163 Sale, A., Berardi, N. & Maffei, L. Environment and brain plasticity: towards an endogenous pharmacotherapy. *Physiological Reviews* **94**, 189-234 (2014).

164 Peters, A. & Kaiserman-Abramof, I. R. The small pyramidal neuron of the rat cerebral cortex. The perikaryon, dendrites and spines. *American Journal of Anatomy* **127**, 321-355 (1970).

165 Harris, K. M., Jensen, F. E. & Tsao, B. Three-dimensional structure of dendritic spines and synapses in rat hippocampus (CA1) at postnatal day 15 and adult ages: implications for the maturation of synaptic physiology and long-term potentiation [published erratum appears in J Neurosci 1992 Aug; 12 (8): following table of contents]. *Journal of Neuroscience* **12**, 2685-2705 (1992).

166 Ziv, N. E. & Smith, S. J. Evidence for a role of dendritic filopodia in synaptogenesis and spine formation. *Neuron* **17**, 91-102 (1996).

167 Yang, G. *et al.* Sleep promotes branch-specific formation of dendritic spines after learning. *Science* **344**, 1173-1178 (2014).

168 Tsai, J., Grutzendler, J., Duff, K. & Gan, W.-B. Fibrillar amyloid deposition leads to local synaptic abnormalities and breakage of neuronal branches. *Nature Neuroscience* **7**, 1181 (2004).

169 Filipello, F. *et al.* The microglial innate immune receptor TREM2 is required for synapse elimination and normal brain connectivity. *Immunity* **48**, 979-991. e978 (2018).

170 Zou, C. *et al.* Neuroinflammation impairs adaptive structural plasticity of dendritic spines in a preclinical model of Alzheimer's disease. *Acta Neuropathologica* **131**, 235-246 (2016).

171 Blumenstock, S. *et al.* Seeding and transgenic overexpression of alpha-synuclein triggers dendritic spine pathology in the neocortex. *EMBO Molecular Medicine* **9**, 716-731 (2017).

172 Garey, L. *et al.* Reduced dendritic spine density on cerebral cortical pyramidal neurons in schizophrenia. *Journal of Neurology, Neurosurgery & Psychiatry* **65**, 446-453 (1998).

173 Glausier, J. R. & Lewis, D. A. Dendritic spine pathology in schizophrenia. *Neuroscience* **251**, 90-107 (2013).

174 Paolicelli, R. C. *et al.* TDP-43 depletion in microglia promotes amyloid clearance but also induces synapse loss. *Neuron* **95**, 297-308. e296 (2017).

175 Hong, S. *et al.* Complement and microglia mediate early synapse loss in Alzheimer mouse models. *Science* **352**, 712-716 (2016).

176 Chung, W.-S. *et al.* Novel allele-dependent role for APOE in controlling the rate of synapse pruning by astrocytes. *Proceedings of the National Academy of Sciences* **113**, 10186-10191 (2016).

177 Ransohoff, R. M. & Perry, V. H. Microglial physiology: unique stimuli, specialized responses. *Annual Review of Immunology* **27**, 119-145 (2009).

178 Kreutzberg, G. W. Microglia: a sensor for pathological events in the CNS. *Trends in Neurosciences* **19**, 312-318 (1996).

179 Gehrmann, J., Matsumoto, Y. & Kreutzberg, G. W. Microglia: intrinsic immuneffector cell of the brain. *Brain Research Reviews* **20**, 269-287 (1995).

180 Hanisch, U. K. Microglia as a source and target of cytokines. *Glia* **40**, 140-155 (2002).

181 Wu, Y., Dissing-Olesen, L., MacVicar, B. A. & Stevens, B. Microglia: dynamic mediators of synapse development and plasticity. *Trends in Immunology* **36**, 605-613 (2015).

182 Stevens, B. *et al.* The classical complement cascade mediates CNS synapse elimination. *Cell* **131**, 1164-1178 (2007).

183 Schafer, D. P. *et al.* Microglia sculpt postnatal neural circuits in an activity and complement-dependent manner. *Neuron* **74**, 691-705 (2012).

184 Harrison, J. K. *et al.* Role for neuronally derived fractalkine in mediating interactions between neurons and CX3CR1-expressing microglia. *Proceedings of the National Academy of Sciences* **95**, 10896-10901 (1998).

185 Jung, S. *et al.* Analysis of fractalkine receptor CX3CR1 function by targeted deletion and green fluorescent protein reporter gene insertion. *Molecular and Cellular Biology* **20**, 4106-4114 (2000).

186 Hoshiko, M., Arnoux, I., Avignone, E., Yamamoto, N. & Audinat, E. Deficiency of the microglial receptor CX3CR1 impairs postnatal functional development of thalamocortical synapses in the barrel cortex. *Journal of Neuroscience* **32**, 15106-15111 (2012).

187 Nimmerjahn, A., Kirchhoff, F. & Helmchen, F. Resting microglial cells are highly dynamic surveillants of brain parenchyma *in vivo*. *Science* **308**, 1314-1318 (2005).

188 Wake, H., Moorhouse, A. J., Jinno, S., Kohsaka, S. & Nabekura, J. Resting microglia directly monitor the functional state of synapses *in vivo* and determine the fate of ischemic terminals. *Journal of Neuroscience* **29**, 3974-3980 (2009).

189 Tremblay, M.-È., Lowery, R. L. & Majewska, A. K. Microglial interactions with synapses are modulated by visual experience. *PLoS Biology* **8**, e1000527 (2010).

190 Perry, V. H., Nicoll, J. A. & Holmes, C. Microglia in neurodegenerative disease. *Nature Reviews Neurology* **6**, 193 (2010).

191 Keren-Shaul, H. *et al.* A unique microglia type associated with restricting development of Alzheimer's disease. *Cell* **169**, 1276-1290. e1217 (2017).

192 Kamphuis, W., Kooijman, L., Schetters, S., Orre, M. & Hol, E. M. Transcriptional profiling of CD11c-positive microglia accumulating around amyloid plaques in a mouse model for Alzheimer's disease. *Biochimica et Biophysica Acta (BBA)-Molecular Basis of Disease* **1862**, 1847-1860 (2016).

193 Martin, E., Boucher, C., Fontaine, B. & Delarasse, C. Distinct inflammatory phenotypes of microglia and monocyte-derived macrophages in Alzheimer's

disease models: effects of aging and amyloid pathology. *Aging Cell* **16**, 27-38 (2017).

194 Sastre, M., Klockgether, T. & Heneka, M. T. Contribution of inflammatory processes to Alzheimer's disease: molecular mechanisms. *International Journal of Developmental Neuroscience* **24**, 167-176 (2006).

195 Brazil, M. I., Chung, H. & Maxfield, F. R. Effects of incorporation of immunoglobulin G and complement component C1q on uptake and degradation of Alzheimer's disease amyloid fibrils by microglia. *Journal of Biological Chemistry* **275**, 16941-16947 (2000).

196 Fu, H. *et al.* Complement component C3 and complement receptor type 3 contribute to the phagocytosis and clearance of fibrillar Aβ by microglia. *Glia* **60**, 993-1003 (2012).

197 Solito, E. & Sastre, M. Microglia function in Alzheimer's disease. *Frontiers in Pharmacology* **3**, 14 (2012).

198 El Khoury, J. *et al.* Scavenger receptor-mediated adhesion of microglia to β-amyloid fibrils. *Nature* **382**, 716 (1996).

199 Richard, K. L., Filali, M., Préfontaine, P. & Rivest, S. Toll-like receptor 2 acts as a natural innate immune receptor to clear amyloid β1–42 and delay the cognitive decline in a mouse model of Alzheimer's disease. *Journal of Neuroscience* **28**, 5784-5793 (2008).

200 Du Yan, S. *et al.* RAGE and amyloid-β peptide neurotoxicity in Alzheimer's disease. *Nature* **382**, 685 (1996).

201 Sheng, J., Mrak, R. & Griffin, W. Microglial inter leukin-1α expression in brain regions in Alzheimer's disease: correlation with neuritic plaque distribution. *Neuropathology and Applied Neurobiology* **21**, 290-301 (1995).

202 Yan, X. *et al.* Interleukin-1beta released by microglia initiates the enhanced glutamatergic activity in the spinal dorsal horn during paclitaxel-associated acute pain syndrome. *Glia* **67**, 482-497 (2019).

203 Garner, K. M., Amin, R., Johnson, R. W., Scarlett, E. J. & Burton, M. D. Microglia priming by interleukin-6 signaling is enhanced in aged mice. *Journal of Neuroimmunology* **324**, 90-99 (2018).

204 Ehrlich, L. C. *et al.* Cytokine regulation of human microglial cell IL-8 production. *The Journal of Immunology* **160**, 1944-1948 (1998).

205 Aloisi, F., Penna, G., Cerase, J., Iglesias, B. M. & Adorini, L. IL-12 production by central nervous system microglia is inhibited by astrocytes. *The Journal of Immunology* **159**, 1604-1612 (1997).

206 Hanisch, U.-K. *et al.* Mouse brain microglia express interleukin-15 and its multimeric receptor complex functionally coupled to Janus kinase activity. *Journal of Biological Chemistry* **272**, 28853-28860 (1997).

207 Prinz, M. & Hanisch, U. K. Murine microglial cells produce and respond to interleukin-18. *Journal of Neurochemistry* **72**, 2215-2218 (1999).

208 Cheeran, M. C.-J., Hu, S., Sheng, W. S., Peterson, P. K. & Lokensgard, J. R. CXCL10 production from cytomegalovirus-stimulated microglia is regulated by both human and viral interleukin-10. *Journal of Virology* **77**, 4502-4515 (2003).

209 Feng, C. *et al.* Expression of CCL2 and its receptor in activation and migration of microglia and monocytes induced by photoreceptor apoptosis. *Molecular Vision* **23**, 765 (2017).

210 Mitrasinovic, O. M. *et al.* Microglia overexpressing the macrophage colony-stimulating factor receptor are neuroprotective in a microglial-hippocampal organotypic coculture system. *Journal of Neuroscience* **25**, 4442-4451 (2005).

211 Walker, D. G. & Lue, L.-F. Immune phenotypes of microglia in human neurodegenerative disease: challenges to detecting microglial polarization in human brains. *Alzheimer's Research & Therapy* **7**, 56 (2015).

212 Kohno, H., Maeda, T., Perusek, L., Pearlman, E. & Maeda, A. CCL3 production by microglial cells modulates disease severity in murine models of retinal degeneration. *The Journal of Immunology* **192**, 3816-3827 (2014).

213 Shiratori, M., Tozaki-Saitoh, H., Yoshitake, M., Tsuda, M. & Inoue, K. P2X7 receptor activation induces CXCL2 production in microglia through NFAT and PKC/MAPK pathways. *Journal of Neurochemistry* **114**, 810-819 (2010).

214 Columba-Cabezas, S., Elena, B. S. & Aloisi, A., Francesca. Lymphoid chemokines CCL19 and CCL21 are expressed in the central nervous system during experimental autoimmune encephalomyelitis: implications for the maintenance of chronic neuroinflammation. *Brain Pathology* **13**, 38-51 (2003).

215 Welser-Alves, J. V. & Milner, R. Microglia are the major source of TNF-α and TGF-β1 in postnatal glial cultures; regulation by cytokines, lipopolysaccharide, and vitronectin. *Neurochemistry International* **63**, 47-53 (2013).

216 Lanfranco, M. F., Mocchetti, I., Burns, M. P. & Villapol, S. Glial-and neuronal-specific expression of CCL5 mRNA in the rat brain. *Frontiers in Neuroanatomy* **11**, 137 (2018).

217 Sato-Hashimoto, M. *et al.* Microglial SIRPα regulates the emergence of CD11c+ microglia and demyelination damage in white matter. *eLife* **8**, e42025 (2019).

218 Janova, H. *et al.* CD 14 is a key organizer of microglial responses to CNS infection and injury. *Glia* **64**, 635-649 (2016).

219 Marques, C. P., Cheeran, M. C., Palmquist, J. M., Hu, S. & Lokensgard, J. R. Microglia are the major cellular source of inducible nitric oxide synthase during experimental herpes encephalitis. *Journal of Neurovirology* **14**, 229-238 (2008).

220 Perlmutter, L., Scott, S., Barron, E. & Chui, H. MHC class II-positive microglia in human brain: association with Alzheimer lesions. *Journal of Neuroscience Research* **33**, 549-558 (1992).

221 Schetters, S. T., Gomez-Nicola, D., Garcia-Vallejo, J. J. & Van Kooyk, Y. Neuroinflammation: microglia and T cells get ready to tango. *Frontiers in Immunology* **8**, 1905 (2018).

222 Lee, C. D. & Landreth, G. E. The role of microglia in amyloid clearance from the AD brain. *Journal of Neural Transmission* **117**, 949-960 (2010).

223 Paresce, D. M., Chung, H. & Maxfield, F. R. Slow degradation of aggregates of the Alzheimer's disease amyloid β-protein by microglial cells. *Journal of Biological Chemistry* **272**, 29390-29397 (1997).

224 Condello, C., Yuan, P., Schain, A. & Grutzendler, J. Microglia constitute a barrier that prevents neurotoxic protofibrillar Aβ42 hotspots around plaques. *Nature Communications* **6**, 6176 (2015).

225 Liu, Z., Condello, C., Schain, A., Harb, R. & Grutzendler, J. CX3CR1 in microglia regulates brain amyloid deposition through selective protofibrillar amyloid-β phagocytosis. *Journal of Neuroscience* **30**, 17091-17101 (2010).

226 Stalder, M., Deller, T., Staufenbiel, M. & Jucker, M. 3D-Reconstruction of microglia and amyloid in APP23 transgenic mice: no evidence of intracellular amyloid. *Neurobiology of Aging* **22**, 427-434 (2001).

227 Sarlus, H. & Heneka, M. T. Microglia in Alzheimer's disease. *The Journal of Clinical Investigation* **127**, 3240-3249 (2017).

228 Fonseca, M. I., Kawas, C. H., Troncoso, J. C. & Tenner, A. J. Neuronal localization of C1q in preclinical Alzheimer's disease. *Neurobiology of Disease* **15**, 40-46 (2004).

229 Afagh, A., Cummings, B. J., Cribbs, D. H., Cotman, C. W. & Tenner, A. J. Localization and cell association of C1q in Alzheimer's disease brain. *Experimental Neurology* **138**, 22-32 (1996).

230 Fonseca, M. I., Zhou, J., Botto, M. & Tenner, A. J. Absence of C1q leads to less neuropathology in transgenic mouse models of Alzheimer's disease. *Journal of Neuroscience* **24**, 6457-6465 (2004).

231 Chalfie, M., Tu, Y., Euskirchen, G., Ward, W. W. & Prasher, D. C. Green fluorescent protein as a marker for gene expression. *Science* **263**, 802-805 (1994).

232 Feng, G. *et al.* Imaging neuronal subsets in transgenic mice expressing multiple spectral variants of GFP. *Neuron* **28**, 41-51 (2000).

233 Banati, R. B. *et al.* Positron emission tomography and functional characterization of a complete PBR/TSPO knockout. *Nature Communications* **5**, 5452 (2014).

234 Fuhrmann, M., Mitteregger, G., Kretzschmar, H. & Herms, J. Dendritic pathology in prion disease starts at the synaptic spine. *Journal of Neuroscience* **27**, 6224-6233 (2007).

235 Mrsic-Flogel, T. D. *et al.* Homeostatic regulation of eye-specific responses in visual cortex during ocular dominance plasticity. *Neuron* **54**, 961-972 (2007).

236 Krashes, M. J. *et al.* Rapid, reversible activation of AgRP neurons drives feeding behavior in mice. *The Journal of Clinical Investigation* **121**, 1424-1428 (2011).

237 Dobin, A. *et al.* STAR: ultrafast universal RNA-seq aligner. *Bioinformatics* **29**, 15-21 (2013).

238 Liao, Y., Smyth, G. K. & Shi, W. featureCounts: an efficient general purpose program for assigning sequence reads to genomic features. *Bioinformatics* **30**, 923-930 (2013).

239 Love, M. I., Huber, W. & Anders, S. Moderated estimation of fold change and dispersion for RNA-seq data with DESeq2. *Genome Biology* **15**, 550 (2014).

240 Brendel, M. *et al.* Glial activation and glucose metabolism in a transgenic amyloid mouse model: a triple-tracer PET study. *Journal of Nuclear Medicine* **57**, 954-960 (2016).

241 Deussing, M. *et al.* Coupling between physiological TSPO expression in brain and myocardium allows stabilization of late-phase cerebral [^{18}F] GE180 PET quantification. *NeuroImage* **165**, 83-91 (2018).

242 Kleinberger, G. *et al.* The FTD-like syndrome causing TREM2 T66M mutation impairs microglia function, brain perfusion, and glucose metabolism. *The EMBO Journal* **36**, 1837-1853 (2017).

243 Leger, M. *et al.* Object recognition test in mice. *Nature Protocols* **8**, 2531 (2013).

244 Richter, L. *et al.* Diazepam-bound $GABA_A$ receptor models identify new benzodiazepine binding-site ligands. *Nature Chemical Biology* **8**, 455 (2012).

245 Sohal, V. S., Zhang, F., Yizhar, O. & Deisseroth, K. Parvalbumin neurons and gamma rhythms enhance cortical circuit performance. *Nature* **459**, 698 (2009).

246 Hu, H., Gan, J. & Jonas, P. Fast-spiking, parvalbumin$^+$ GABAergic interneurons: From cellular design to microcircuit function. *Science* **345**, 1255263 (2014).

247 Pritchett, D. B. & Seeburg, P. H. γ-Aminobutyric $acid_A$ receptor α_5-subunit creates novel type II benzodiazepine receptor pharmacology. *Journal of Neurochemistry* **54**, 1802-1804 (1990).

248 Romeo, E. *et al.* 2-Aryl-3-indoleacetamides (FGIN-1): a new class of potent and specific ligands for the mitochondrial DBI receptor (MDR). *Journal of Pharmacology and Experimental Therapeutics* **262**, 971-978 (1992).

249 Löw, K. *et al.* Molecular and neuronal substrate for the selective attenuation of anxiety. *Science* **290**, 131-134 (2000).

250 Crestani, F. *et al.* Trace fear conditioning involves hippocampal α_5 $GABA_A$ receptors. *Proceedings of the National Academy of Sciences* **99**, 8980-8985 (2002).

251 Wolf, L. *et al.* Enhancing neurosteroid synthesis–relationship to the pharmacology of translocator protein (18 kDa) (TSPO) ligands and benzodiazepines. *Pharmacopsychiatry* **48**, 72-77 (2015).

252 Salter, M. W. & Stevens, B. Microglia emerge as central players in brain disease. *Nature Medicine* **23**, 1018 (2017).

253 Wake, H., Moorhouse, A. J., Miyamoto, A. & Nabekura, J. Microglia: actively surveying and shaping neuronal circuit structure and function. *Trends in Neurosciences* **36**, 209-217 (2013).

254 Chung, W.-S., Welsh, C. A., Barres, B. A. & Stevens, B. Do glia drive synaptic and cognitive impairment in disease? *Nature Neuroscience* **18**, 1539 (2015).

255 Elmore, M. R. *et al.* Colony-stimulating factor 1 receptor signaling is necessary for microglia viability, unmasking a microglia progenitor cell in the adult brain. *Neuron* **82**, 380-397 (2014).

256 Kreisl, W. C. *et al. In vivo* radioligand binding to translocator protein correlates with severity of Alzheimer's disease. *Brain* **136**, 2228-2238 (2013).

257 Pariente, A., de Gage, S. B., Moore, N. & Bégaud, B. The benzodiazepine–dementia disorders link: Current state of knowledge. *CNS Drugs* **30**, 1-7 (2016).

258 Knabl, J. *et al.* Reversal of pathological pain through specific spinal $GABA_A$ receptor subtypes. *Nature* **451**, 330 (2008).

259 R Atack, J. $GABA_A$ receptor subtype-selective modulators. II. α5-selective inverse agonists for cognition enhancement. *Current Topics in Medicinal Chemistry* **11**, 1203-1214 (2011).

260 Dejanovic, B. *et al.* Changes in the synaptic proteome in tauopathy and rescue of tau-induced synapse loss by C1q antibodies. *Neuron* **100**, 1322-1336. e1327 (2018).

261 Towers, S. *et al.* α5 subunit-containing $GABA_A$ receptors affect the dynamic range of mouse hippocampal kainate-induced gamma frequency oscillations *in vitro*. *The Journal of Physiology* **559**, 721-728 (2004).

262 Mably, A. J. & Colgin, L. L. Gamma oscillations in cognitive disorders. *Current Opinion in Neurobiology* **52**, 182-187 (2018).

263 Paolicelli, R. C. *et al.* Synaptic pruning by microglia is necessary for normal brain development. *Science* **333**, 1456-1458 (2011).

264 Neniskyte, U. & Gross, C. T. Errant gardeners: glial-cell-dependent synaptic pruning and neurodevelopmental disorders. *Nature Reviews Neuroscience* **18**, 658 (2017).

265 Choi, J., Ifuku, M., Noda, M. & Guilarte, T. R. Translocator protein (18 kDa)/peripheral benzodiazepine receptor specific ligands induce microglia functions consistent with an activated state. *Glia* **59**, 219-230 (2011).

266 Deplanque, D. *et al.* Etifoxine impairs neither alertness nor cognitive functions of the elderly: A randomized, double-blind, placebo-controlled crossover study. *European Neuropsychopharmacology* **28**, 925-932 (2018).

Abbreviations

°C	Degree Celcius
µm	Micrometer
µL	Microliter
Aβ	Amyloid beta
AAV	Adeno-associated virus
AD	Alzheimer's disease
AICD	Amyloid precursor protein intracellular domain
ALS	Amyotrophic lateral sclerosis
ANOVA	Analysis of variance
APLP1	amyloid precursor-like protein 1
APLP2	amyloid precursor-like protein 2
ApoE4	Apolipoprotein E ε4
APP	Amyloid precursor protein
BSA	Bovine serum albumin
C1q	Complement component 1q
C3	Complement component 3
Ca^{2+}	Calcium ion
CaMKII	Ca^{2+} / calmodulin-dependent protein kinase-II
CCL2	C-C motif chemokine ligand 2
CCL3	C-C motif chemokine ligand 3
CCL4	C-C motif chemokine ligand 4
CCL5	C-C motif chemokine ligand 5
CCL19	C-C motif chemokine ligand 19
CCL22	C-C motif chemokine ligand 22
CDK-5	Cyclin-dependent protein kinase 5
Cl^-	Chloride ion
cm	Centimeter
CNO	Clozapine *N*-oxide
CNS	Central nervous system

CR3	Complement receptor 3; Macrophage-1 antigen
CSF	Cerebrospinal fluid
CSF1R	Colony-stimulating factor 1 receptor
CTF	C-terminal fragment
CXCL2	C-X-C motif chemokine ligand 2
CXCL8	C-X-C motif chemokine ligand 8
CXCL10	C-X-C motif chemokine ligand 10
3D	Three-dimensional
DBI	Diazepam binding inhibitor
DNA	Deoxyribonucleic acid
DREADDs	Designer receptors exclusively activated by designer drugs
e.g.	*Exempli gratia*; for example
eGFP	Enhanced green fluorescent protein
ELISA	Enzyme-linked immunosorbent assay
et al.	*Et alii*; And others
FAD	Familial Alzheimer's disease
FDG-PET	Fluorodeoxyglucose positron emission tomography
Fig.	Figure
fMRI	Functional magnetic resonance imaging
GABA	γ-aminobutyric acid
$GABA_AR$s	γ-aminobutyric acid type A receptors
GFP	Green fluorescent protein
GFP-M	Thymocyte antigen 1 (Thy1)-eGFP line M
GSK-3β	Glycogen synthase kinase 3β
h	Hour
i.g.	Intragastric
Iba1	Ionized calcium-binding adapter molecule 1
IGIF	Interferon-γ inducing factor
IL-1α	Interleukin-1α
IL-1β	Interleukin-1β
IL-6	Interleukin-6
IL-8	Interleukin-8

IL-12	Interleukin-12
IL-15	Interleukin-15
IL-18	Interleukin-18
iNOS	Inducible nitric oxide synthase
i.p.	Intraperitoneal
IP-10	Interferon-γ induced protein-10
ITGAX	Integrin subunit α X
kDa	Kilodalton
kg	Kilogram
LSCM	Laser scanning confocal microscopy
M	Molar
MCI	Mild cognitive impairment
MCP-1	Monocyte chemoattractant protein-1
M-CSF	Macrophage colony-stimulating factor
MDC	Macrophage-derived chemokine
mg	Milligram
MHC II	Major histocompatibility complex class II
min	Minute
MIP-1α	Macrophage inflammatory proteins-1α
MIP-1β	Macrophage inflammatory proteins-1β
MIP-2	Macrophage inflammatory protein-2
MIP-3β	Macrophage inflammatory proteins-3β
mL	Milliliter
mM	Millimolar
NFTs	Neurofibrillary tangles
NGS	Normal goat serum
nL	Nanoliter
nm	Nanometer
NORT	Novel object recognition test
OFT	Open field test
p	Probability value; *p*-value
PBR	Peripheral-type benzodiazepine receptor

PBS	Phosphate-buffered saline
PBTx	Triton X-100 in PBS
PCR	Polymerase chain reaction
PD	Parkinson's disease
PET	Positron emission tomography
pH	Power of hydrogen
PHFs	Paired helical fragments
p.i.	Propidium Iodide
PKA	cAMP-dependent protein kinase A
PSD	Postsynaptic density
PSD-95	Postsynaptic density protein 95
PSEN1	Presenilin 1
PSEN2	Presenilin 2
P-tau	Phosphorylated tau
PV	Parvalbumin
RNA	Ribonucleic acid
s.c.	Subcutaneous
SCYB10	Small-inducible cytokine B10
s.e.m.	Standard error of the mean
sMRI	Structural magnetic resonance imaging
Tab.	Table
TDP-43	Transactive response DNA-binding protein
TGF-β	Transforming growth factor β
Thy 1	Thymocyte antigen 1; CD90
TNF-α	Tumor necrosis factor-α
TNF-β	Tumor necrosis factor-β
TREM2	Triggering receptor expressed on myeloid cells 2
TSPO	18 kDa translocator protein
VDAC	Voltage-dependent anion channel
Vg	Viral genomes
WT	Wild-type

Acknowledgements

I would like to express my sincere thanks and gratitude to the people who have supported me in completing this dissertation.

I thank my advisor, Prof. Dr. Jochen Herms, for his continuous support on this project. I have benefited a lot from his enlightening. This Ph.D. thesis and a lot of my other scientific progress beyond this thesis could not have been done without his constant support and encouragement.

Furthermore, I thank Prof. Dr. Armin Giese and Dr. Mario Dorostkar, two members of my thesis advisory committee, for their contributions and witness of my professional development during my graduate education.

During my doctoral studies, I was privileged to work with a lot of excellent researchers and received enormous help from them. First of all, I would like to thank Prof. Dr. Gerhard Rammes for his essential advice on neuropharmacology. I would also like to thank Prof. Dr. Rainer Rupprecht for actively participating in the experimental design and discussion. I thank Prof. Dr. Richard B. Banati, Dr. Guo-Jun Liu, and Dr. Ryan J. Middleton for their support in generating the knock-out mice and experimental design. I also thank Prof. Dr. Hanns Ulrich Zeilhofer and Prof. Dr. Uwe Rudolph for providing knock-in mice and comments on experiments. I appreciate the support of my research from my collaborators Dr. Matthias Brendel and Florian Eckenweber in performing PET scanning, Katharina Ochs in RNA sequencing, Nils Briel in human tissue histology, Mochen Cui in 3D rendering, and Dr. Chengyu Zou in intravital imaging. I thank Chun Zhang and Ji Wu for their help with illustrations.

I would also like to acknowledge Dr. Gerda Mitteregger, Dr. Meike Miller, Dr. Anne von Thaden, Dr. Manuela Schneider, Dr. Thomas Arzberger, Claudia Ihbe and Nadine Lachner for their technical support and animal care. I appreciate the help of Katrin Pratsch in preparing human brain samples. I am grateful to Dr. Barbara von

Ungern-Sternberg and Karin Bormann-Giglmaier for technical assistance in PET scanning.

I thank Fanfan Sun, Dr. Kaichuan Zhu, Dr. Elena Montagna, Dr. Steffen Burgold, Sonja Einhaus, and all other members in AG Herms. They offered me technical supports, helpful discussions, and a friendly working environment.

Last, but most importantly, I thank my parents. I deeply appreciate their unconditional love and support throughout my studies and whole life. My life during the five-year Ph.D. studies, challenging but exciting, would be completely different without them.

List of Publications

Articles and manuscripts:

1. **Shi Y**, Cui M, Brendel M, Ochs K, Briel N, Eckenweber F, Zou C, Banati RB, Liu G, Middleton RJ, Rupprecht R, Rudolph U, Zeilhofer HU, Rammes G, Dorostkar MM, Herms J. The Benzodiazepine diazepam impairs dendritic spine plasticity via translocator protein (18 kDa): implications for Alzheimer's disease. (Submitted)

2. **Shi Y**, Cui M, Ochs K, Sun F, Banati RB, Liu G, Middleton RJ, Dorostkar MM, Herms J. Targeting translocator protein (18 kDa) alleviates alpha-synuclein-triggered dendritic spine pathology. (In preparation)

3. **Shi Y**, Brendel M, Cui M, Sun F, Ochs K, Dorostkar MM, Herms J. Microglial repopulation restores microglia responsivity in Alzheimer's disease models. (In preparation)

4. Focke C*, Blume T*, Zott B*, **Shi Y***, Deussing M, Peters F, Schmidt C, Kleinberger G, Lindner S, Gildehaus FJ, Beyer L, von Ungern-Sternberg B, Bartenstein P, Ozmen L, Baumann K, Dorostkar MM, Haass C, Adelsberger H, Herms J, Rominger A, Brendel M. Early and longitudinal microglial activation but not amyloid accumulation predict cognitive outcome in PS2APP mice. *The Journal of Nuclear Medicine*, 2019 Apr; 60(4):548-554. (*Contributed equally)

5. Zou C, Crux S, Marinesco S, Montagna E, Sgobio C, **Shi Y**, Shi S, Zhu K, Dorostkar MM, Müller UC, Herms J. Amyloid precursor protein maintains constitutive and adaptive plasticity of dendritic spines in adult brain by regulating D-serine homeostasis. *The EMBO Journal*. 2016 Oct 17; 35(20):2213-2222.

6. Zou C, **Shi Y**, Ohli J, Schüller U, Dorostkar MM, Herms J. Neuroinflammation impairs adaptive structural plasticity of dendritic spines in a preclinical model of Alzheimer's disease. *Acta Neuropathologica.* 2016 Feb; 131(2):235-246.

7. Zou C, Montagna E, **Shi Y**, Peters F, Blazquez-Llorca L, Shi S, Filser S, Dorostkar MM, Herms J. Intraneuronal APP and extracellular Aβ independently cause dendritic spine pathology in transgenic mouse models of Alzheimer's disease. *Acta Neuropathologica.* 2015 Jun; 129(6): 909-20.

Scientific poster presentations:

1. **Shi Y**, Dorostkar MM, Ochs K, Herms J. Targeting Translocator Protein (18 kDa) alleviates alpha-synuclein-triggered dendritic spine pathology. *14th International Conference on Alzheimer's and Parkinson's Diseases*. 2019 Mar; Lisbon, Portugal.

2. **Shi Y**, Dorostkar MM, Herms J. Translocator protein (18 kDa) ligand PK11195 alleviates alpha-synuclein-induced dendritic spine pathology. *11th FENS Forum of Neuroscience*. 2018 Jul; Berlin, Germany.

3. **Shi Y**, Dorostkar MM, Herms J. Pioglitazone alleviates synapse loss via suppressing complement-dependent pathway in a preclinical model of Alzheimer's disease. *1st International Conference on Cognitive Reserve in the Dementias*. 2017 Nov; Munich, Germany.

4. **Shi Y**, Dorostkar MM, Rammes G, Herms J. Diazepam impairs structural plasticity of dendritic spines in somatosensory cortex independent of $GABA_A$

receptor activation. *47th Annual Meeting of the Society for Neuroscience*. 2017 Nov; Washington DC, USA.

Curriculum Vitae

Name: Shi, Yuan Nationality: Chinese

Education

2014 - 2019	Ph.D. student Neuroscience/ Neuropharmacology Ludwig-Maximilians-University of Munich
2011 - 2014	Master of Medicine Neuropharmacology Peking Union Medical College, Tsinghua University, P.R. China
2007 - 2011	Bachelor of Science Pharmacology Shandong University, P.R. China

Honours

2014	LMU Doctoral Scholarship
2010	National Scholarship, Ministry of Education

Language Skills

Chinese	Native Language
English	Fluent
German	Basic

IT Skills

Graphing	GraphPad Prism, Adobe Photoshop, Adobe Illustrator
Imaging	Imaris (advanced), ImageJ, ZEN (advanced)

Eidesstattliche Versicherung/Affidavit

Hiermit versichere ich an Eides statt, dass ich die vorliegende Dissertation The Benzodiazepine Diazepam Impairs Synaptic Plasticity via Translocator Protein (18 kDa): Implications for Alzheimer's Disease selbstständig angefertigt habe, mich außer der angegebenen keiner weiteren Hilfsmittel bedient und alle Erkenntnisse, die aus dem Schrifttum ganz oder annähernd übernommen sind, als solche kenntlich gemacht und nach ihrer Herkunft unter Bezeichnung der Fundstelle einzeln nachgewiesen habe.

I hereby confirm that the dissertation The Benzodiazepine Diazepam Impairs Synaptic Plasticity via Translocator Protein (18 kDa): Implications for Alzheimer's Disease is the result of my own work and that I have only used sources or materials listed and specified in the dissertation.

München, den 13. 09. 2019

Yuan Shi

Confirmation of Congruency

I hereby declare that the electronic version of the submitted dissertation, entitled The Benzodiazepine Diazepam Impairs Synaptic Plasticity via Translocator Protein (18 kDa): Implications for Alzheimer's Disease is congruent with the printed version both in content and format.

München, den 13. 09. 2019

Yuan Shi